THE IMPACT OF ROCK TYPES ON ELECTRICAL PROPERTIES AND RESERVOIR FLUID SATURATION

BY

Mamdouh Nasser Al-Nasser

A Thesis Presented to the
DEANSHIP OF GRADUATE STUDIES

KING FAHD UNIVERSITY OF PETROLEUM & MINERALS
DHAHRAN, SAUDI ARABIA

In Partial Fulfillment of the
Requirements for the Degree of

MASTER OF SCIENCE
In

PETROLEUM ENGINEERING

December 2011

KING FAHD UNIVERSITY OF PETROLEUM & MINERALS
DHAHRAN 31261, SAUDI ARABIA

DEANSHIP OF GRADUATE STUDIES

This thesis, written by **MAMDOUH NASSER AL-NASSER** under the direction of his thesis advisor and approval by his thesis committee, has been presented to and accepted by the Dean of Graduate Studies, in partial fulfillment of the requirements for the degree of **MASTER OF SCIENCE IN PETROLEUM ENGINEERING**.

Thesis Committee

Dr. Hasan Y. Al-Yousef (Thesis Advisor)

Nov 21, 2011

Dr. Maclean O. Amabeoku (Member)

Dr. Mohamed A. Nasr El-Din (Member)

Dr. Abdulaziz A. Al-Majed
(Department Chairman)

Dr. Salam A. Zummo
(Dean of Graduate Studies)

13/12/11

Date

DEDICATION

This thesis is dedicated to my loving parents and my family members.

ACKNOWLEDGEMENT

At first, my thanks are due to our god, the most compassionate, beneficent and graceful who has given me the ability and the patience to pursue master degree in petroleum engineering at KFUPM. Secondly, I appreciate the great deal of support I have received from my family members who truly were the ladder of success.

Moreover, I extend my heartfelt gratitude to my Faculty at KFUPM specially my thesis committee members for unlimited support and alignment that enabled me to complete the degree requirements within the timeframe I had set earlier.

Also, I owe a debt of thanks to Reservoir Description and simulation Department's management in Saudi Aramco at all levels who opened the gate for me to pursue advance degree program and make it possible.

TABLE OF CONTENTS

LIST OF TABLES

LIST OF FIGURES

THESIS ABSTRACT

NAME:	MAMDOUH NASSER AL-NASSER
TITLE:	THE IMPACT OF ROCK TYPES ON ELECTRICAL PROPERTIES AND RESERVOIR FLUID SATURATION
MAJOR FILED:	PETROLEUM ENGINEERING
DATE OF DEGREE:	December 2011

Understanding complex variations in pore geometry within different lithofacies is the key to improved reservoir description and development. Geological description provides information on various depositional and diagenetic controls on pore geometry. Variations in pore geometrical attributes in turn, define the existence of distinct hydraulic units with similar fluid-flow characteristics. Classic discrimination of rock types has been based on subjective geological observations. However, for any porosity within a given rock type, permeability can vary by several orders of magnitude, which indicates the existence of several flow units. The differences in flow units represent variation in the electrical properties which are essential in hydrocarbon saturation evaluation.

In this particular study electrical properties were measured for different hydraulic units identified in two reservoirs. The electrical properties showed variations due to the rock types or hydraulic units. Open-hole logs were then used to compute water saturation in the well using the hydraulic units based cementation and saturation exponents. There is 5.3 percent decrease in the water saturation using hydraulic units derived parameters, compared to using single-value average electrical parameters in Reservoir-D. The decrease in water saturation using hydraulic units technique is very significant, as this translates to an equivalent increase in oil-in-place estimation. There is a minor increase of 1 percent in water saturation across Reservoir-F.

The approach used in this study to classify the reservoir rock into distinct types and assigning applicable petrophysical properties, has improved the oil-in-place estimation.

اسم الطالب : ممدوح ناصر النصر

عنوان الرسالة : تأثير نوعية الصخور على الخصائص الكهربية وتشبع المكامن بالسوائل

التخصص : هندسة البترول

تاريخ الدرجة : ديسمبر ٢٠١١

فهم المتغيرات المركبة في هندسة المسام ضمن الخصائص المختلفة للأحجار ، هو المفتاح لتحسين وصف المكامن وتطويرها. يوفر الوصف الجيولوجي معلومات حول مختلف التأثيرات الرسوبية والتحولية على هندسة المسام ، كما تسهم التغييرات في صفات المسام الهندسية بدورها في تحديد وجود وحدات هيدرولوكية متميزة مع صفات مشابهه لتحرك السوائل. الطريقة التقليدية للتفريق بين الصخور اعتمد على الملاحظة الجيولوجية الموضوعية ، لكن المسامية والنفاذية في نوعية معينة من الصخور يمكن أن تتغير باستخدام مقاييس كمية مختلفة والذي يدل على وجود وحدات سوائل معينة متعددة. الاختلاف بين وحدات السوائل ينتج تغيرات في الصفات الكهربية والذي يعد ضرورياً في تقييم التشبع للهايدروكربون.

في هذه الدراسة الخاصة تم قياس الخصائص الكهربائية لوحدات هيدروليكية مختلفة أمكن تحديدها في مكمنين. وأظهرت نتائج الخواص الكهربائية تباينا بسبب اختلاف أنواع الصخور أو الوحدات الهيدروليكية. ولقد تم استعمال بيانات سجلات آبار غير مغلفة في حساب قيم التشبع بالماء في البئر باستخدام معامل سمنتة وأسس تشبع مستخلصة من الوحدات الهيدروليكية. أظهرت النتائج انخفاضاً قدره ٥,٣% لقيم التشبع المائي مقارنة بالتشبع المتحصل بإستخدام خصائص كهربائية وحيد القيمة في المكن "د". الإنخفاض في التشبع المائي المتحصل بإستخدام طريقة الوحدات الهيدروليكية يعتبر مهم جدا و يعكس زيادة متساوية لتقدير كمية الزيت في المكمن. كما لوحظ وجود زيادة طفيفة في قيم التشبع المائي يساوي ١% عبر المكمن "ف".

إن النهج المتبع في هذه الدراسة في تصنيف الصخور إلى أنواع متميزة وتعيين خواص بتروفيزيائية قابلة للتطبيق أدى إلى تحسين تقدير كمية الزيت في المكمن.

درجة ماجستير العلوم
جامعة الملك فهد للبترول والمعادن
الظهران – المملكة العربية السعودية
التاريخ: ديسمبر ٢٠١١

CHAPTER 1

INTRODUCTION

An accurate determination of electrical properties in early life of reservoirs or an evaluation of a developed reservoir is required to better estimate the hydrocarbon volumes. Archie formula ($S_w = (a.R_w/\Phi^m.R_t)^{1/n}$) is the basic equation to compute water saturation in clean formation and in some cases it is suitable for shaly water saturation model in shaly formation. The accuracy of water saturation value for given reservoir conditions depends on the accuracy of Archie parameters a, m, and n. The terms of Archie relationship have been subjected to many laboratory investigations and even more speculations. There are many factors affecting cementation factor (porosity exponent), m, saturation exponent, n and tortousity factor, a. Therefore, it is very difficult to determine Archie parameters when neglecting reservoir characteristic, rock wettability, formation water salinity, permeability, porosity and fluid distribution.

The routine petrophysical evaluation applies a constant value of Archie's parameters a, m and n in a given reservoir. The constants are applied in the equation for water saturation estimation using resistivity log measurements. However, based on literature review, field experience and Aramco studies, the n value varies from 1.7 for strongly water wet up to 3 for strongly oil wet formations. It is also known that the cementation factor, m and the tortousity factor, a are affected by the physical and chemical properties of the rock.

The purpose of this study is two-fold. First is to measure electrical properties (cementation and saturation exponents) and determine if they vary significantly by rock type or hydraulic units. Secondly, compute water saturation with the hydraulic unit based cementation and saturation exponents. Open-hole logs will be re-processed, using fixed parameters and the results will be compared with those obtained with variable parameters. Recommendations will be made on applicable electrical parameter sets and methodology to calculate water saturation in reservoirs that exhibit several rock types.

CHAPTER 2

LITERATURE REVIEW

2.1 Electrical Properties

Electrical properties of reservoir rocks are important in calculating water saturation, and hence oil-in-place, and residual oil saturation through resistivity well logs. These properties are determined in the laboratory by testing core samples under simulated temperature and overburden pressure conditions.

Commonly, the matrix of a rock is non-conducting. The resistance of a rock is represented by a highly complex network of series and parallel connected resistors. Each resistor can be defined as a fluid-filled single pore or a channel between the pores. Therefore, the resistivity of a rock is a function of porosity, pore geometry, and resistivity of the fluid filling the pores. Archie [1942] defined the following relationship when the rock is 100% saturated with water:

$$R_O = F \,.\, R_W \text{ or } F = R_O / R_W \qquad (2.1)$$

Where:

R_O = Formation resistivity at 100% brine saturation, ohm-m^2/m
R_W = Brine resistivity, ohm-m^2/m
F = Formation resistivity factor

The resistivity of a clean rock, R_t, is a function of water saturation S_w, formation water resistivity R_w, and rock structure, which is represented by the formation resistivity factor (or simply formation factor) *F:*

$$Rt = F \,.\, Rw / Sw^n \qquad (2.2)$$

where, *n* is a constant called the saturation exponent.

The formation factor *F*, is a function of fractional porosity φ, and two other rock parameters called cementation factor *m*, and structural parameter *a*. *F* is expressed as follows:

$$F = a / \varphi^{m} \qquad (2.3)$$

The cementation factor, saturation exponent, and structural parameter (m, n, and a*,* respectively) are called the *electrical parameters,* and are calculated from Equations (2.2) and (2.3) after measuring the other parameters in the equations. These parameters are used in the Archie [1942] and other derived shaly formation equations [Waxman and Smits, 1968; Fertl and Hammack, 1971; Clavier, 1977; Neasham, 1977; and Simandoux, 1982] in order to calculate the water saturation, and hence oil-in-place, and residual oil saturation through resistivity logs.

Core measurements in the laboratory are preferably done under overburden conditions which affect pore geometry. The cementation factor *m*, and structural parameter *a*, are the result of pore geometry, which is controlled by various textural rock properties. [Pirson, 1947; Atkins and Smith, 1961; Mendelson and Cohen, 1982; Perez, 1982; Ramson, 1984; Saner et al., 1997]. Overburden pressure reduces the porosity of the rock and changes its tortuosity and pore constriction factor [Fatt, 1957;Wyble, 1959; Dobrynin, 1962; Helander and Campbell, 1966; and Saner et al., 1996]. Therefore, the formation resistivity factor increases rapidly as pressure increases.

Fluid distribution in the pores is an important factor influencing rock resistivity. In dual-porous water-wet rocks, water fills micro pores and provides a pathway for electrical current [Blum and Martin, 1995]. This results in low resistivity. On the other hand, for the same water saturation value, the resistivity of a rock varies significantly for different wetting conditions [Keller, 1953; Sweeny and Jennings, 1960; Mungan and Moore, 1968; Anderson, 1986; Lewis et al, 1988; Donaldson and Siddiqui, 1989]. As oil saturation increases, electrical resistivity increases far more dramatically in the more oil-wet systems than in the more water-wet systems. Sometimes waterflood behavior may exhibit oil-wet characteristics, whereas electrical resistivity may remain essentially the same as for water-wet systems due to low resistivity caused by the influence of pore-wall roughness on the contact angle in rock/oil/water systems [Swanson, 1980].

2.2 Hydraulic Units

Ebanks (1987) defined a hydraulic units as a volume of the total reservoir rock within which geological and petrophysical properties that affect fluid flow are internally consistent and predictably different from properties of other rock volumes. It is a zone that is continuous over a defined volume of the reservoir, has similar average rock properties that affect flow with similar bedding characteristics. Distribution of flow units is related to facies distribution, but flow unit boundaries do not necessarily coincide with facies boundaries.

Hydraullic Unit Characterization Technique

The hydraulic unit zonation scheme devised by Amaefule et al. (1993) is used to compute and distinguish the different flow units.

The equation is given as :

$$\log(RQI) = \log(PHIZ) + \log(FZI) \tag{2.4}$$

Where:

RQI is reservoir quality index which is a close approximation to the mean flow radius in a reservoir rock and is defined as below:

$$RQI = 0.0314\sqrt{\frac{K}{\varphi}} \tag{2.5}$$

PHIZ is the normalized porosity index and defined as:

$$PHIZ = \frac{\varphi}{1-\varphi} \tag{2.6}$$

FZI is the flow zone indicator and calculated by:

$$FZI = \frac{RQI}{PHIZ} \tag{2.7}$$

The derivation of these simplified equations by Amaefule et al. originated from the generalized form of Kozeny (1927) and Carmen (1937) relationship among porosity, permeability, surface area, and pore shape factor. Amaefule's derivation shows that a bi-logarithmic plot of RQI versus PHIZ will yield a straight line with unit slope. The intercept of this straight line at PHIZ =1 is the flow zone indicator (FZI). Core samples that lie on the same straight line have similar pore thorat characteristics and therefore, constitute a flow unit. Samples with different FZI will lie on the other parallel lines. Figure 2.1 shows a plot of reservoir qulity index versus PHIZ calculated from porosity permeability data to determine the Hus. In this example, Seven hydraulic units were identified.

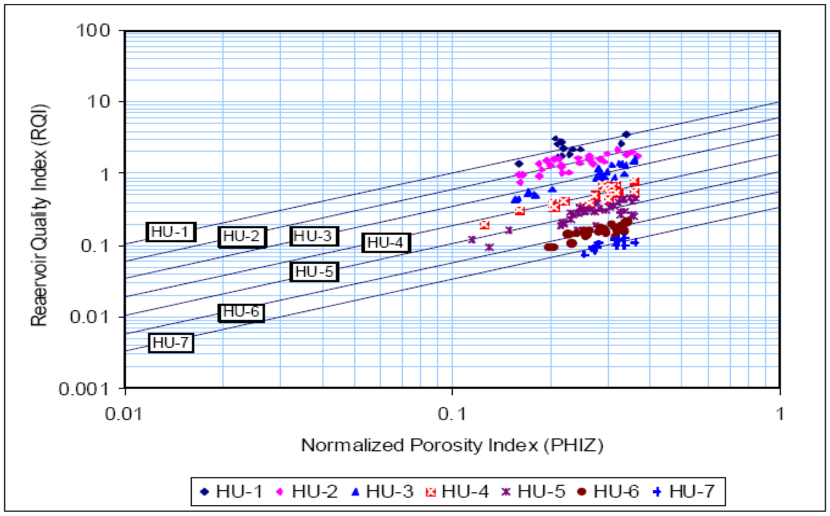

Figure 2.1: Determination of hydraulic (flow) units with porosity and permeability data

2.3 Winland Rock Typing Method

The quality of a reservoir can be characterized by flow units which are controlled by hydrocarbon storage and flow capacity. Flow units define the intervals of similar and predictable flow characteristics. Flow units can be identified from an interrelated series of petrophysical cross plots and from the calculation of pore throat radii (R35, pore size) at the 35% pore volume using the following Winland (1972) equation:

$$\text{Log}\,(R35) = 0.732 + 0.588 \log(K) - 0.864 \log(\Phi) \tag{2.8}$$

Where R35 is the calculated pore throat radius at 35% mercury saturation from mercury injection capillary pressure test (micron), K is permeability (md), and Φ is porosity (percentage). The core sample of a given rock type will have similar R35 values which are utilized to define petrophysical units as given below:

- Mega-port, units with R35 values greater than 10 micron.
- Macro-port, units with R35 values between 2 and 10 micron.
- Meso-port, units with R35 values between 0.5 and 2 micron.
- Micro-port, units with R35 values between 0.1 and 0.5 micron.
- Nano-port, units with R35 values smaller than 0.1 micron.

CHAPTER 3

STATEMENT OF THE PROBLEM

3.1 Statement of The Problem

Routine petrophysical evaluation applies constant values for Archie's parameters a, m and n in a given reservoir. The constants are applied in the equation to calculate water saturation using resistivity log measurements. However, based on literature review, field experience and Saudi Aramco studies, the n value varies from 1.7 which is strongly water wet up to 3 which is strongly oil wet. It is also known that the cementation factor, m and the tortuousity factor, a are affected by the physical and chemical properties of the rock.

3.2 Objectives

The objectives of this project are to:

i. Investigate the variation of electrical parameters with rock type or hydraulic units.
ii. Assess the impact of using constant or variable electrical parameters to compute water saturation using Archie's equation on reserves estimation.
iii. Classify electrical parameters by rock type and/or hydraulic units.

3.3 Proposed Approach

To achieve the proposed objective, the following project plan will be followed:

i. Collect core sample.

ii. Perform CT scan, thin section, SEM, XRD analysis.

iii. Conduct mercury injection capillary pressure.

iv. Measure porosity and permeability of core samples

v. Determine hydraulic units zonation and rock type.

vi. Conduct resistivity experiments to determine cementation and saturation exponent.

vii. Determine electrical properties (cementation and saturation exponents) by rock type or hydraulic units.

viii. Compute water saturation with the hydraulic unit based on cementation and saturation exponents.

ix. Re-process open-hole logs using fixed parameters and compare the results with those obtained with variable parameters.

x. Compare the results and come up with recommendations.

CHAPTER 4

EXPERIMENTAL PROCEDURES

4.1 Sample Preparation and Analytical Procedures

4.1.1 Sample Cleaning, Drying and Pre-analysis Preparation:

The sample was selected in the laboratory from the subject wells. In preparation for the petrographic analysis, the sample required cleaning. The sample was cleaned in a constant immersion-constant replenishment modified soxhlet extraction apparatus, with Toluene to remove any possible hydrocarbons and water, and methanol to displace any residual salts. On completion of the cleaning phase the samples were dried to constant weights in a standard oven at 85°C.

4.1.2 Thin Section (TS)

A slice of the cleaned sample was impregnated with blue epoxy resin to facilitate the identification of porosity. After hardening, a thin slice of the sample was taken and mounted onto a glass slide, after which it ground/polished down to a thickness of 30 microns. The thin section was stained with sodium cobalt nitrate and mixed Alizarin Red-S/potassium ferricyanide, to aid in the identification of feldspar grains and carbonates respectively, before a cover slip was applied.

4.1.3 Dry Scanning Electron Microscopy (SEM)

Freshly broken fragments of the cleaned and dried sample were mounted individually on to standard SEM stubs, using Araldite Rapid Resin as the adhesive. Prior to high resolution/high magnification analysis by SEM the samples were coated with gold by sputter coating to prevent charging under the SEM electron beam. During the analysis, identification of minerals was aided by the use of Energy Dispersive X-ray Analysis (EDS), which provides the qualitative elemental composition of the mineral analyzed.

The gold coated sample stub was placed in a vacuum chamber where an electron beam was fired at the specimen. Low energy secondary electrons are reflected from the surface of the sample and produce the image which was then captured by a camera. The sample was viewed on a screen at high resolution/high magnification. By examining the entire sample at a range of magnifications, a full analysis was obtained. Testing included the identification of minerals from elemental composition by using the EDS.

4.1.4 X-Ray Diffraction (XRD) Analysis

As part of this study XRD analysis has been carried out and the analytical procedure will be briefly described in the following:

Bulk rock XRD analysis

The cleaned sample was gently disaggregated with a pestle and mortar, and then 'micronized' using a McCrone Micronising Mill to obtain an X-ray diffraction 'powder' with a mean particle diameter between 5-10 microns. The slurry was then dried and packed into an aluminum cavity mount, producing a randomly orientated sample for presentation to the X-ray beam. Each whole rock sample was analyzed between 5-60 degrees 2 theta at a step size of 0.05 degrees/sec. Samples were exposed to X-ray radiation from a copper anode at 40kV, 30mA. Peak heights were measured for each mineral present. The counts (peak height) for each mineral were compared to a standard count for a pure sample of that mineral and a percentage calculated. The final results are presented as a normalized percentage for each mineral identified.

Clay fraction XRD analysis

The less than 2 micron fraction was separated from the sample by ultrasound, shaking and centrifugation. The total weight of clay extracted was obtained by removing 20ml of clay suspension and evaporating to dryness. Size fractions greater than 2 micron (e.g. 2-16 micron) were obtained by varying the centrifuge speed and time. The XRD mount was obtained by filtering the clay suspension through a Millipore filter and drying the filtrate on the filter paper. The samples were analyzed as untreated clay, after 'glycolation' overnight and following 'heating' at 380°C for 2 hours and 550°C for one hour. The initial scan for the treatments was between 3-35 degrees 2 theta at a step size of 0.05 degrees/sec. Samples were exposed to X-Ray radiation from a copper anode at 40kV, 30mA. The untreated sample was also analyzed between 24-27 degrees 2 theta at a step size of 0.02 degrees/2 sec to further define kaolinite/chlorite peaks. Traces obtained from the four clay treatments were studied to assess the clay mineral assemblages present. Peak height measurements were taken and incorporated in a formula to indicate the relative amounts of clay minerals present. The data was then used to semi-quantify the clay minerals with respect to the whole rock by reference to the amount of <2 micron clay fraction which had been previously extracted. A qualitative indication of the clay mineral crystallinities can be given by assessment of the peak width for each component. Where applicable the relative intensities of the chlorite 001 and 003 peaks were used to measure the total heavy metal (predominantly Fe) content of the mineral.

4.2 Basic Rock Properties

i. Grain volume was determined for each sample by placing it into a stainless steel matrix cup. It was injected with helium from reference cells of known volume and pressure using the Core Lab AutoPorosimeter. Grain volume was calculated using Boyle's law of gas expansion. Grain density was calculated by dividing sample dry weight by grain volume.

ii. The samples were loaded into the CMS300^{TM} for determination of permeability and porosity. Net confining pressure was applied.

iii. Helium was injected into the sample from reference cells of known volume and pressure. A direct pore volume was determined using Boyle’s law of gas expansion, then pressure was vented at a known rate and unsteady-state Klinkenberg permeability was determined by pressure decay.

iv. Porosity was calculated for each sample as the pore volume fraction of the summation (grain volume + pore volume) bulk volume.

4.3 Mercury Injection

4.3.1 Preparing samples

i. The samples were trimmed as necessary to fit within the penetrometer chambers of the Micromeritics AutoPore devices.

ii. After drying in a vacuum oven, the samples were placed into a desiccator to prevent adsorption of moisture from the atmosphere as they cooled.

iii. Dry weight was measured using an analytical balance (±0.001g).

iv. The Ultra-Porosimeter^{TM} was used to obtain measured grain volume data. The system uses a sample chamber into which helium is allowed to expand as it is injected from reference cells of known volume and pressure. Grain volume was calculated using Boyle's law of gas expansion. The dry weight was divided by the grain volume to calculate the grain density.

v. An ambient, mercury immersion bulk volume was determined. Pore volume was calculated as the difference between bulk volume and grain volume. The pore volume was divided by bulk volume to calculate the porosity fraction.

vi. The samples were placed into a stainless steel cylinder and evacuated overnight, then were pressure saturated with toluene, a strongly wetting fluid. Saturated pore volume data were obtained and compared to the (mercury bulk – grain volume) pore volumes. The saturated pore volumes are generally the preferred values used.

vii. The samples were re-dried in a vacuum oven to fully remove the toluene.

4.3.2 High-Pressure Mercury Injection

i. Testing was performed using the Micromeritics Auto pore 9320, an automated, high pressure mercury injection device which operates at injection pressures of 0 to 55,000 psia.

ii. Each test sample was weighed, and then loaded into a glass penetrometer consisting of a sample chamber attached to a capillary stem with a cylindrical coaxial capacitor. Each penetrometer used was selected on the basis of how well its capacity matched the sample pore volume to maximize accuracy and resolution.

iii. The sample/penetrometer assembly was weighed, and then placed into the low pressure system.

iv. The sample chamber was evacuated and filled with mercury, then the pressure was increased incrementally to slightly above atmospheric pressure. At the end of the low pressure phase the assembly was temporarily removed and re-weighed, then placed into the high pressure side of the apparatus.

v. Pressures were increased incrementally to a maximum of 55,000 psia.

vi. Time was allowed at each incremental pressure for saturation equilibrium. The volume of mercury injected at each pressure was determined by the change in capacitance of the capillary stem.

vii. The pressure was decreased to ambient and the sample unloaded. A final weight was recorded to calculate the residual mercury saturation.

viii. Micromeritics data were imported to a spreadsheet and the mercury volumes calculated. A conformance (correction for surface roughness) value was selected, volume corrections made, and saturations calculated.

ix. Pore throat size, fluid system pressure conversion, and height data were calculated using some published parameters.

4.4 Formation Factor

i. Synthetic formation brine of approximately 200,000-ppm was prepared in the laboratory using reagent-grade chemicals and de-ionized water. The synthetic brine resistivity (R_w) was measured.

ii. The core samples were vacuum/pressure saturated with synthetic formation brine. Sample saturations were verified, using sample weights before and after the saturation procedure and Archimedes bulk volume to calculate saturated porosity, and then comparing saturated porosity with Helium porosity.

iii. The brine saturated core samples were individually mounted into hydrostatic core-holders and a confining stress of 2400-psi was applied. After priming the system to remove any trapped gas, synthetic formation brine was introduced under pressure at the upstream face.

iv. The core samples were then individually mounted into 2-electrode high-pressure resistivity cells with conductive plates and silver screens at each end face. A conductive porous ceramic disk was placed at the production face of the core assembly. They were stressed to the appropriate confining stress using oil as the hydraulic fluid.

v. Synthetic formation brine was introduced again through the core samples with 300 psi backpressure, to displace any trapped gas in the system.

vi. Core sample resistivities (R_o) were measured (1000 Hz) until constant values were achieved (+/-1%) with phase angles less than 2 degrees.

vii. The saturated core resistivities (R_o), saturating brine resistivity (R_w) and porosities were used to calculate the formation factors (F) and cementation exponents (m) of each core plug according to the following equations:

$$F = R_o/R_w \tag{4.1}$$

$$m = \log F/\log \text{Porosity} \tag{4.2}$$

viii. Formation Factor (F) was plotted versus Porosity (fraction) on a log-log plot. An average line fit through the data points and unity (1,1) using a least squares linear regression, identified the cementation exponent (m), the slope of the line. Using the fitted line through unity forces a value of 1 for ‘a’.

4.5 Resistivity Index with Oil-Water Capillary Pressure by Porous-Plate

i. After formation factor testing, each core plug was unloaded and a 15-bar brine-saturated ceramic disk was mounted against the downstream end face. The disk had silver paint around the edges making the plate resistance negligible.

ii. The core plugs were re-loaded in resistivity cells with confining pressure.

iii. Saturating formation brine was flowed through the core–ceramic disk system until the resistivities agreed with the resistivities measured in step vii above.

iv. The core samples were desaturated using a step desaturation process where crude oil was injected at the upstream end faces of each system. Brine production and the corresponding sample resistivities (Rt) were recorded throughout the desaturation process.

v. After the conclusion of the measurements, the core holders were disassembled. The final core plug water saturations were confirmed gravimetrically.

vi. Resistivity index (RI) were calculated from resistance (R_o and R_t) measurements according to the following:

$$RI = R_t / R_o \tag{4.3}$$

vii. A least squares linear regression plot for Resistivity Index (RI) versus water saturation (S_w) fitted through unity (1,1) yielded a line whose slope defines the composite n. Individual saturation exponent n values were calculated using the formula:

$$n = \log RI / \log S_w \tag{4.4}$$

viii. Corresponding core sample saturations were calculated from brine displacement measurements:

$$S_w = [V_p - (W_w/\rho_w)]/V_p \tag{4.5}$$

Where: W_w = Weight of brine displaced

ρ_w = Density of Brine

V_p = Pore Volume

ix. Capillary pressures were plotted against corresponding stable saturations to provide capillary pressure curves for each sample.

CHAPTER 5

SAMPLE SCREENING AND SELECTION

5.1 Samples Selection

The main objective of sample selection is to select core samples that represent the petrophysical properties of the studied rock units. Minimal but sufficient number of samples will reduce analysis time and eventually will save unnecessary cost spend on it. Therefore, the following steps and procedures were taken in order to discriminate the core samples according to its group petrophysical properties.

The cores are analyzed with different techniques for different parameters in this study. The available laboratory measurements for the core samples that are used on rock typing and sample selection:

i. Standard porosity and permeability measurements, Figure 5.1
  - RQI method.
  - Winland method.

ii. Mercury injection
  - Pore throat size distribution
  - Incremental fluid saturation

iii. CT scan for minerals identification and its geometry distribution
iv. Thin section for mineralogy and sedimentation
v. SEM to visualize the geological description.
vi. XRD to analyze and examine the minerals present in the sample.

All the above analysis complimented each other in the process to identify the rock properties starting from mineralogy to geology point of views. The combination of it leads to verification of petrophysical properties. The laboratory analysis combined with computational petrophysical analysis has resulted in a schematic sample selection that will be explained in the following paragraph.

The core analysis results had been incorporated in the following petrophysical analysis. The core porosity and permeability measurements (Table-5.1) were used in constructing the Hydraulic Units (HU) correlation. Eventually, correlation between petrophysical parameters and rock geological properties was established in this study. The following paragraph will explain the process involved in sample selection.

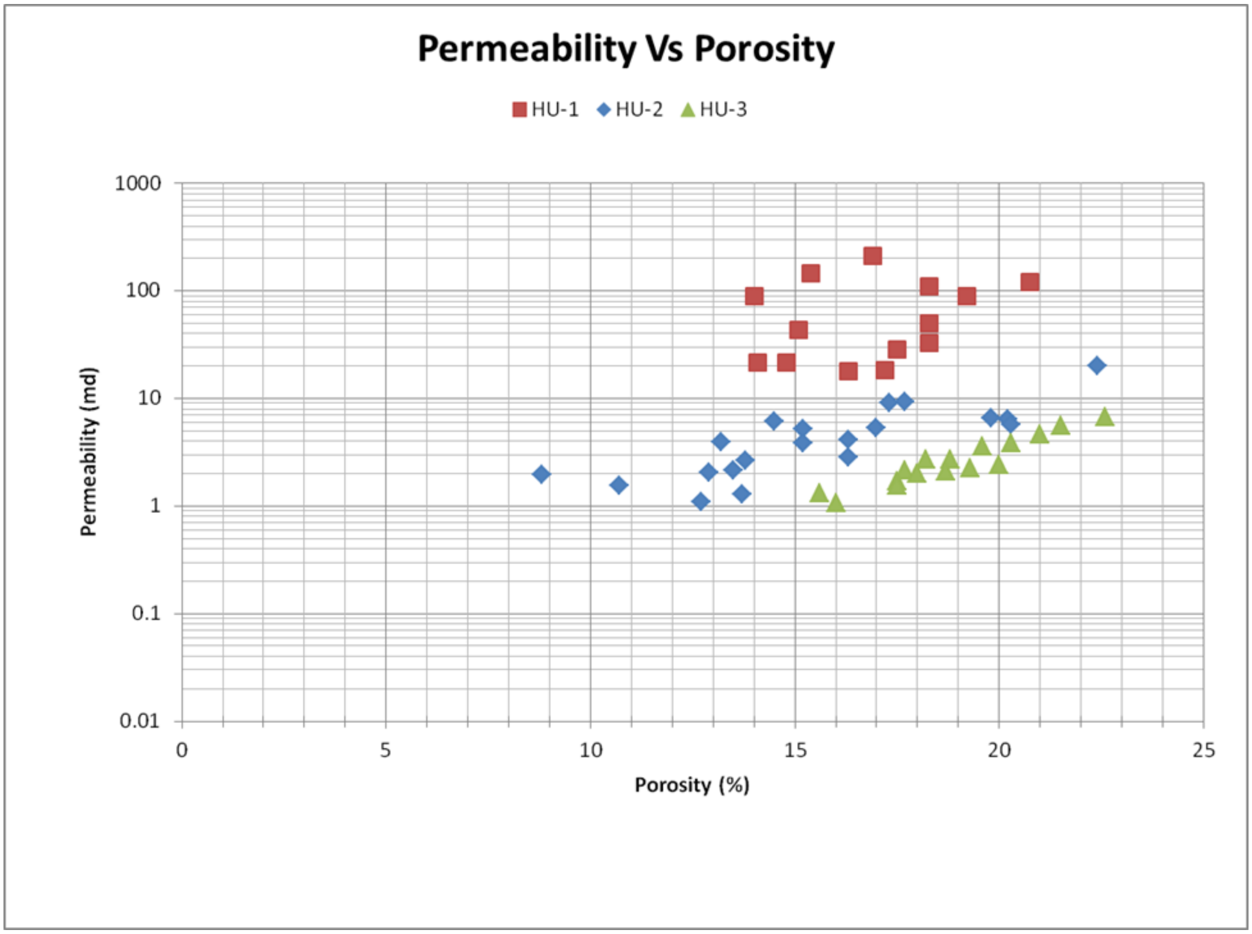

Figure 5.1: Porosity and permeability relationship

5.2 Building the Hydraulic Units

Using Amaefule's derivation, from porosity and permeability measurements, Table 5.1, the bi-logarithmic plot of RQI versus PHIZ will yield a straight line with unit slope. The intercept of this straight line at PHIZ =1 is the flow zone indicator (FZI). Core samples that lie on the same straight line have similar pore throat characteristics and therefore, constitute a flow unit. Samples with different FZI will lie on the other parallel lines. Figure 5.2 shows a plot of reservoir quality index versus PHIZ calculated from porosity permeability data to determine the hydraulic units. Three hydraulic units were identified.

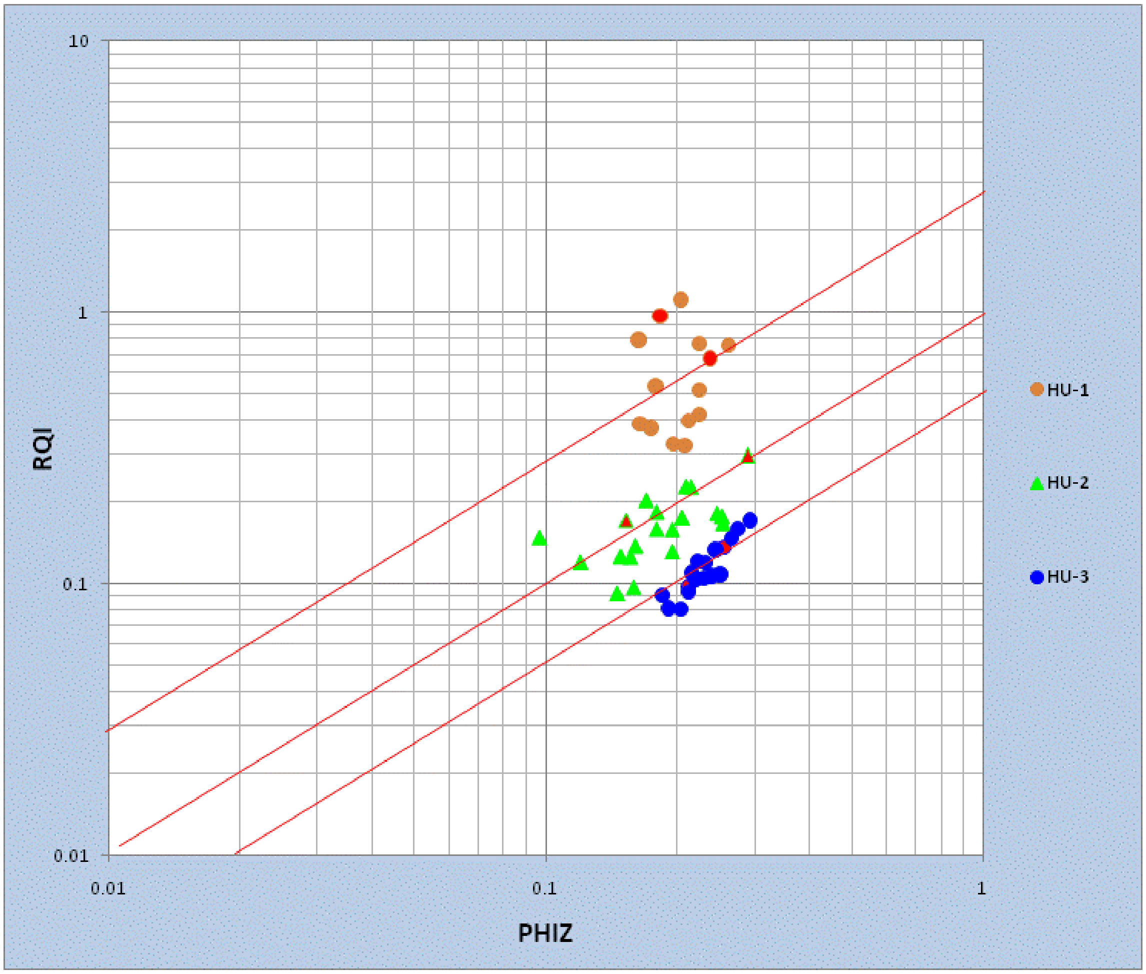

Figure 5.2: Determination of hydraulic flow units from porosity and permeability data

Table 5.1: RQI, PHIZ (NPI) and FZI for hydraulic flow units determination

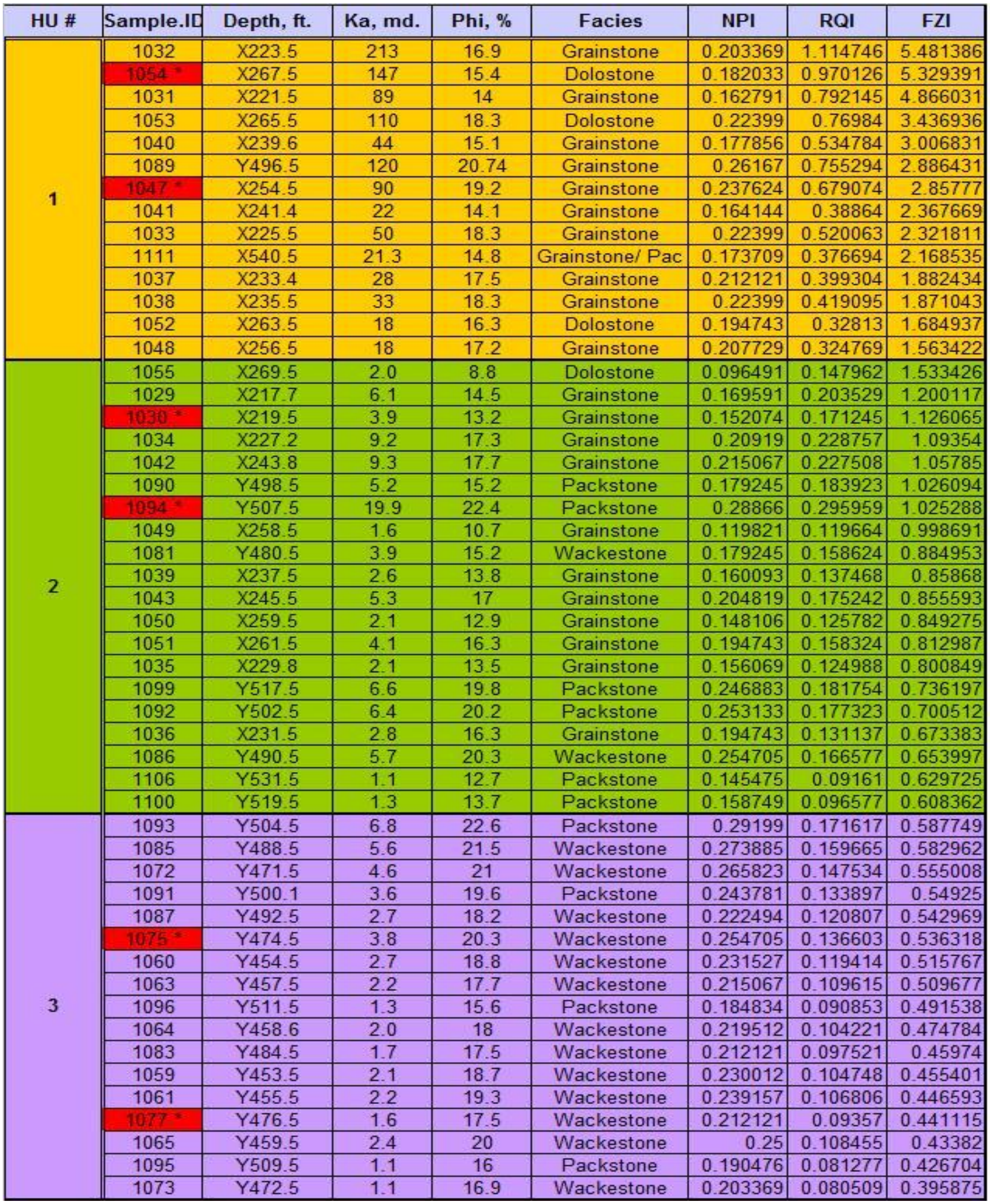

HU #	Sample.ID	Depth, ft.	Ka, md.	Phi, %	Facies	NPI	RQI	FZI
1	1032	X223.5	213	16.9	Grainstone	0.203369	1.114746	5.481386
	1054 *	X267.5	147	15.4	Dolostone	0.182033	0.970126	5.329391
	1031	X221.5	89	14	Grainstone	0.162791	0.792145	4.866031
	1053	X265.5	110	18.3	Dolostone	0.22399	0.76984	3.436936
	1040	X239.6	44	15.1	Grainstone	0.177856	0.534784	3.006831
	1089	Y496.5	120	20.74	Grainstone	0.26167	0.755294	2.886431
	1047 *	X254.5	90	19.2	Grainstone	0.237624	0.679074	2.85777
	1041	X241.4	22	14.1	Grainstone	0.164144	0.38864	2.367669
	1033	X225.5	50	18.3	Grainstone	0.22399	0.520063	2.321811
	1111	X540.5	21.3	14.8	Grainstone/ Pac	0.173709	0.376694	2.168535
	1037	X233.4	28	17.5	Grainstone	0.212121	0.399304	1.882434
	1038	X235.5	33	18.3	Grainstone	0.22399	0.419095	1.871043
	1052	X263.5	18	16.3	Dolostone	0.194743	0.32813	1.684937
	1048	X256.5	18	17.2	Grainstone	0.207729	0.324769	1.563422
2	1055	X269.5	2.0	8.8	Dolostone	0.096491	0.147962	1.533426
	1029	X217.7	6.1	14.5	Grainstone	0.169591	0.203529	1.200117
	1030 *	X219.5	3.9	13.2	Grainstone	0.152074	0.171245	1.126065
	1034	X227.2	9.2	17.3	Grainstone	0.20919	0.228757	1.09354
	1042	X243.8	9.3	17.7	Grainstone	0.215067	0.227508	1.05785
	1090	Y498.5	5.2	15.2	Packstone	0.179245	0.183923	1.026094
	1094 *	Y507.5	19.9	22.4	Packstone	0.28866	0.295959	1.025288
	1049	X258.5	1.6	10.7	Grainstone	0.119821	0.119664	0.998691
	1081	Y480.5	3.9	15.2	Wackestone	0.179245	0.158624	0.884953
	1039	X237.5	2.6	13.8	Grainstone	0.160093	0.137468	0.85868
	1043	X245.5	5.3	17	Grainstone	0.204819	0.175242	0.855593
	1050	X259.5	2.1	12.9	Grainstone	0.148106	0.125782	0.849275
	1051	X261.5	4.1	16.3	Grainstone	0.194743	0.158324	0.812987
	1035	X229.8	2.1	13.5	Grainstone	0.156069	0.124988	0.800849
	1099	Y517.5	6.6	19.8	Packstone	0.246883	0.181754	0.736197
	1092	Y502.5	6.4	20.2	Packstone	0.253133	0.177323	0.700512
	1036	X231.5	2.8	16.3	Grainstone	0.194743	0.131137	0.673383
	1086	Y490.5	5.7	20.3	Wackestone	0.254705	0.166577	0.653997
	1106	Y531.5	1.1	12.7	Packstone	0.145475	0.09161	0.629725
	1100	Y519.5	1.3	13.7	Packstone	0.158749	0.096577	0.608362
3	1093	Y504.5	6.8	22.6	Packstone	0.29199	0.171617	0.587749
	1085	Y488.5	5.6	21.5	Wackestone	0.273885	0.159665	0.582962
	1072	Y471.5	4.6	21	Wackestone	0.265823	0.147534	0.555008
	1091	Y500.1	3.6	19.6	Packstone	0.243781	0.133897	0.54925
	1087	Y492.5	2.7	18.2	Wackestone	0.222494	0.120807	0.542969
	1075 *	Y474.5	3.8	20.3	Wackestone	0.254705	0.136603	0.536318
	1060	Y454.5	2.7	18.8	Wackestone	0.231527	0.119414	0.515767
	1063	Y457.5	2.2	17.7	Wackestone	0.215067	0.109615	0.509677
	1096	Y511.5	1.3	15.6	Packstone	0.184834	0.090853	0.491538
	1064	Y458.6	2.0	18	Wackestone	0.219512	0.104221	0.474784
	1083	Y484.5	1.7	17.5	Wackestone	0.212121	0.097521	0.45974
	1059	Y453.5	2.1	18.7	Wackestone	0.230012	0.104748	0.455401
	1061	Y455.5	2.2	19.3	Wackestone	0.239157	0.106806	0.446593
	1077 *	Y476.5	1.6	17.5	Wackestone	0.212121	0.09357	0.441115
	1065	Y459.5	2.4	20	Wackestone	0.25	0.108455	0.43382
	1095	Y509.5	1.1	16	Packstone	0.190476	0.081277	0.426704
	1073	Y472.5	1.1	16.9	Wackestone	0.203369	0.080509	0.395875

* Samples that are selected for further analysis.

5.3 Winland Rock Typing

Hydraulic units identified by flow zone index (FZI) are revised utilizing Winland R35 rock typing approach by using porosity permeability data. Winland plot shows the rock quality distribution which range from macro to mega ports (Figure 5.3). Winland characterization advances the determined hydraulic units.

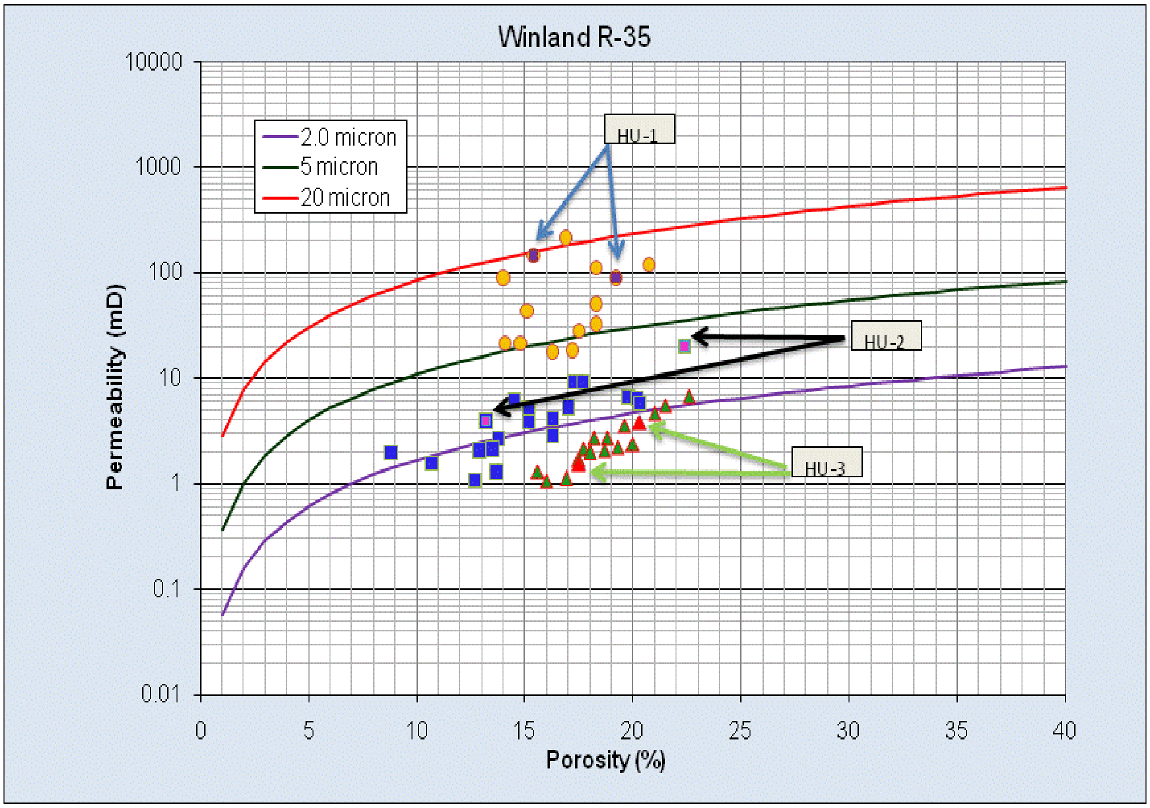

Figure 5.3: Porosity permeability plot of the studied reservoir, Winland R-35 (Arrows point to samples used for further analysis).

5.4 Pore Throat Size Distribution

In addition to RQI and Winland methods, pore throat size distribution from mercury capillary pressure data was also used for sample selection. The computation of pore throat radius from mercury intrusion data is given as follows:

$$Ri = \frac{2\sigma * \cos\theta * C}{Pc} \qquad (5.1)$$

where: Ri = Pore entry radius, microns
σ = Interfacial tension
θ = Contact angle
C = Unit conversion constant (to microns) = 0.145
Pc = Mercury injection pressure, psia.

Figure 5.4 shows pore throat size distributions of all the samples. Pore throat size distribution data will be explained in details for each hydraulic unit in the next section.

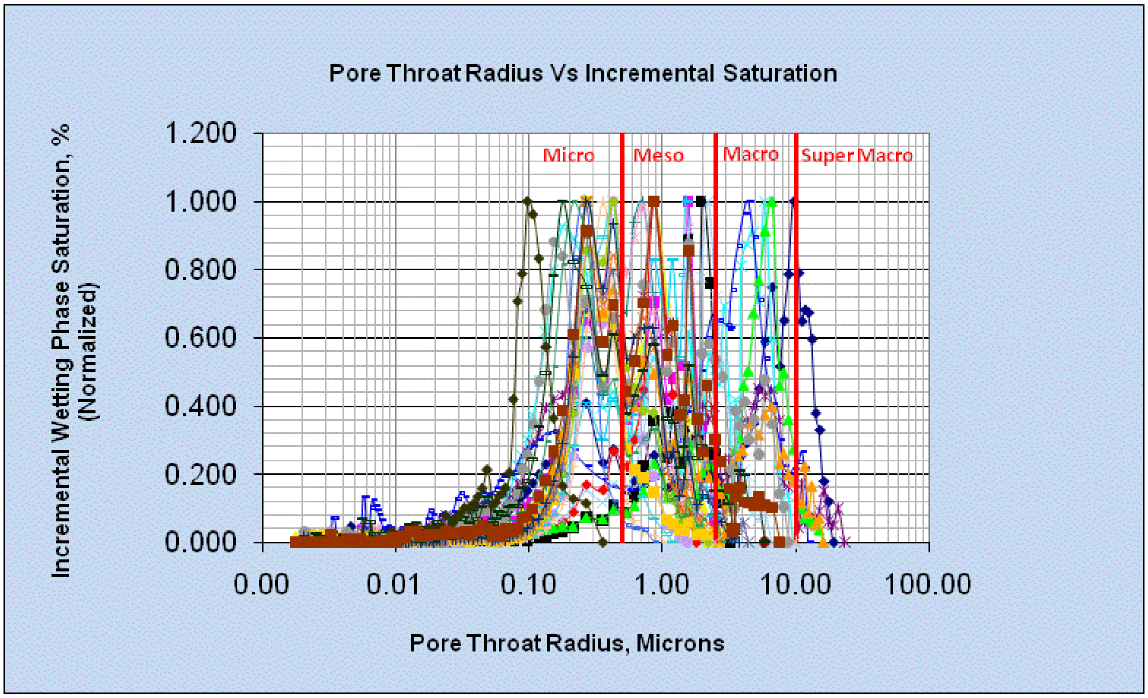

Figure 5.4: Pore throat size distribution from mercury data.

Table 5.2 lists the samples used for thin section, SEM and XRD to support and enhance the sample selection and rock typing.

Table 5.2: Summary of TS, SEM and XRD performed analysis

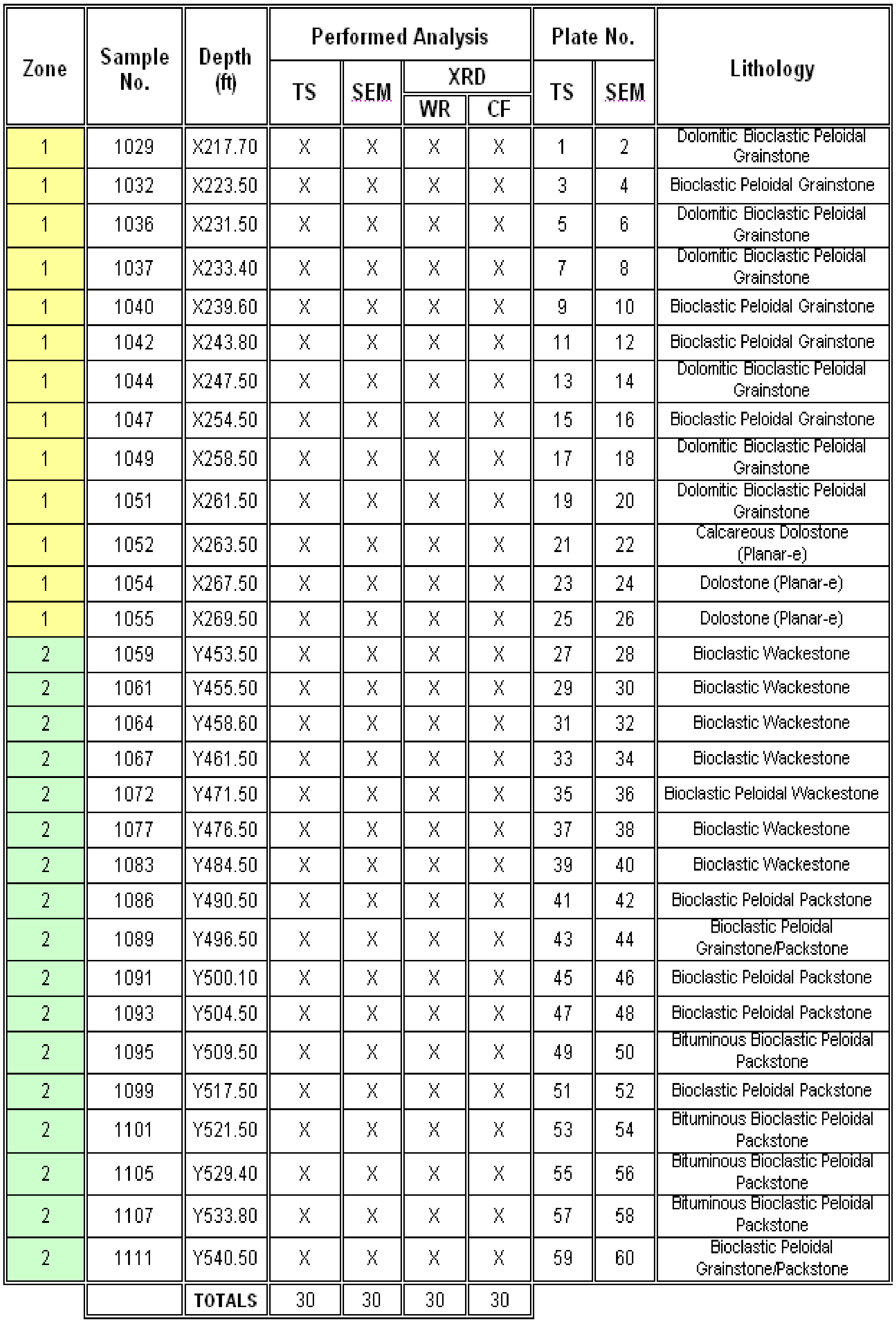

Zone	Sample No.	Depth (ft)	Performed Analysis				Plate No.		Lithology
			TS	SEM	XRD		TS	SEM	
					WR	CF			
1	1029	X217.70	X	X	X	X	1	2	Dolomitic Bioclastic Peloidal Grainstone
1	1032	X223.50	X	X	X	X	3	4	Bioclastic Peloidal Grainstone
1	1036	X231.50	X	X	X	X	5	6	Dolomitic Bioclastic Peloidal Grainstone
1	1037	X233.40	X	X	X	X	7	8	Dolomitic Bioclastic Peloidal Grainstone
1	1040	X239.60	X	X	X	X	9	10	Bioclastic Peloidal Grainstone
1	1042	X243.80	X	X	X	X	11	12	Bioclastic Peloidal Grainstone
1	1044	X247.50	X	X	X	X	13	14	Dolomitic Bioclastic Peloidal Grainstone
1	1047	X254.50	X	X	X	X	15	16	Bioclastic Peloidal Grainstone
1	1049	X258.50	X	X	X	X	17	18	Dolomitic Bioclastic Peloidal Grainstone
1	1051	X261.50	X	X	X	X	19	20	Dolomitic Bioclastic Peloidal Grainstone
1	1052	X263.50	X	X	X	X	21	22	Calcareous Dolostone (Planar-e)
1	1054	X267.50	X	X	X	X	23	24	Dolostone (Planar-e)
1	1055	X269.50	X	X	X	X	25	26	Dolostone (Planar-e)
2	1059	Y453.50	X	X	X	X	27	28	Bioclastic Wackestone
2	1061	Y455.50	X	X	X	X	29	30	Bioclastic Wackestone
2	1064	Y458.60	X	X	X	X	31	32	Bioclastic Wackestone
2	1067	Y461.50	X	X	X	X	33	34	Bioclastic Wackestone
2	1072	Y471.50	X	X	X	X	35	36	Bioclastic Peloidal Wackestone
2	1077	Y476.50	X	X	X	X	37	38	Bioclastic Wackestone
2	1083	Y484.50	X	X	X	X	39	40	Bioclastic Wackestone
2	1086	Y490.50	X	X	X	X	41	42	Bioclastic Peloidal Packstone
2	1089	Y496.50	X	X	X	X	43	44	Bioclastic Peloidal Grainstone/Packstone
2	1091	Y500.10	X	X	X	X	45	46	Bioclastic Peloidal Packstone
2	1093	Y504.50	X	X	X	X	47	48	Bioclastic Peloidal Packstone
2	1095	Y509.50	X	X	X	X	49	50	Bituminous Bioclastic Peloidal Packstone
2	1099	Y517.50	X	X	X	X	51	52	Bioclastic Peloidal Packstone
2	1101	Y521.50	X	X	X	X	53	54	Bituminous Bioclastic Peloidal Packstone
2	1105	Y529.40	X	X	X	X	55	56	Bituminous Bioclastic Peloidal Packstone
2	1107	Y533.80	X	X	X	X	57	58	Bituminous Bioclastic Peloidal Packstone
2	1111	Y540.50	X	X	X	X	59	60	Bioclastic Peloidal Grainstone/Packstone
		TOTALS	30	30	30	30			

Note: The analysis results will be described and discussed in Appendix-A.

5.5 Geological characteristics of samples constituting the Hydraulic Units

All samples are classified as limestone and further subdivided according to the carbonate classification scheme (Dunham, 1962, Figure 5.5). The Dunham classification is used as basis for the geological description given in Appendix A.

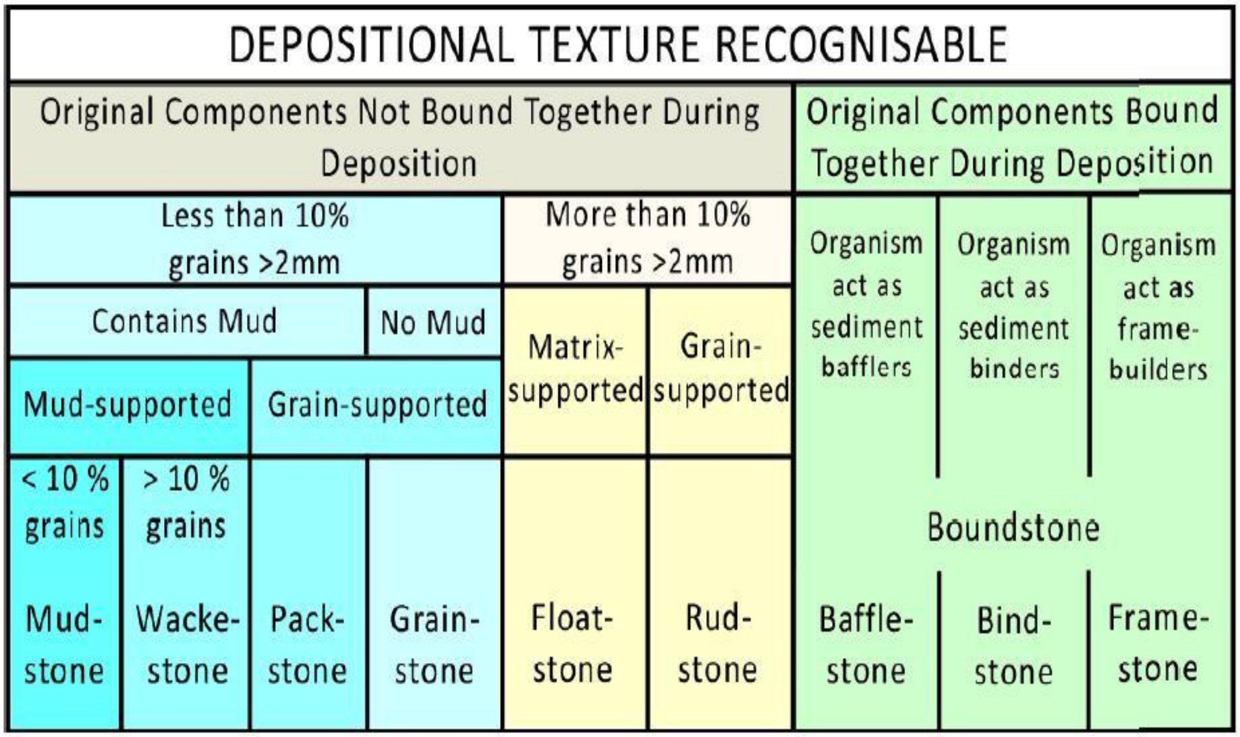

DEPOSITIONAL TEXTURE RECOGNISABLE								
Original Components Not Bound Together During Deposition						Original Components Bound Together During Deposition		
Less than 10% grains >2mm				More than 10% grains >2mm		Organism act as sediment bafflers	Organism act as sediment binders	Organism act as frame-builders
Contains Mud			No Mud	Matrix-supported	Grain-supported			
Mud-supported		Grain-supported						
< 10 % grains	> 10 % grains					Boundstone		
Mud-stone	Wacke-stone	Pack-stone	Grain-stone	Float-stone	Rud-stone	Baffle-stone	Bind-stone	Frame-stone

Figure 5.5: Classification table of carbonate rocks (Dunham, 1962)

5.5.1 Hydraulic Unit 1

HU1 is classified mainly as Bioclastic Peloidal Grainstone which is the dominant facies in this HU and some dolostone. The samples of this facies show moderate to good reservoir quality. The amount of total cement and amount of porosity are the main controlling parameters on the reservoir quality. Measured gas permeability of the samples ranges from 33 to 213 mD with an average of 77mD.

The thin section photomicrograph (TS) and scanning electron micrograph of a representative sample in hydraulic unit 1 is described in details in Appendix-A.

Mercury injection

Figure 5.6 shows typical mercury intrusion capillary pressure curve of hydraulic unit 1 and the pore throat size distribution calculated from the mercury data. Bimodality of the pore geometry can be observed in some samples, the pores are classified mainly as macro as they are dominated by pore throats and some meso pores. Proportions of super macro pores are small.

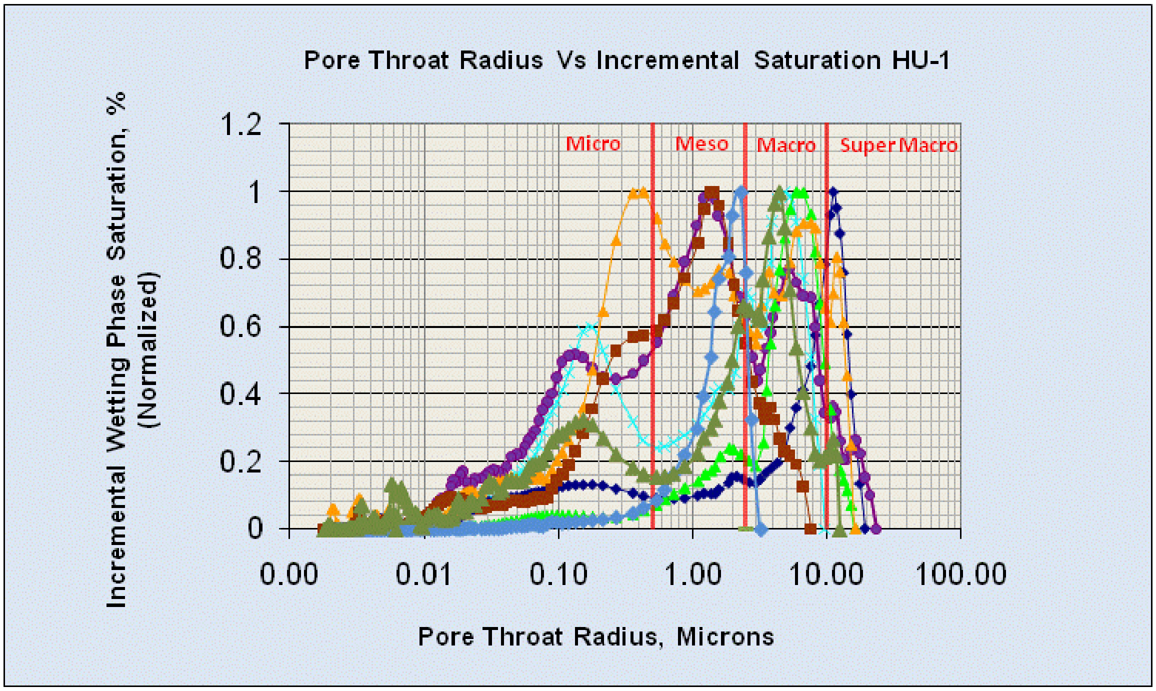

Figure 5.6: Pore throat size distribution of Hydraulic unit 1

5.5.2 Hydraulic Unit 2

Hydraulic unit 2 is classified mainly as Dolomitic Bioclastic Peloidal Grainstone which is the dominant facies in this hydraulic unit and some Bioclastic Peloidal Packstone. The samples of this facies show poor reservoir quality, porosity and cementation are the main controlling parameters on reservoir quality of this facies. The effective pore system is significantly downgraded by cementation (especially dolomite cement). Large crystals of dolomite fill the pore spaces and decrease the pore interconnectivity. Measured gas permeability of the samples ranges from 1.6 to 9.3 mD with an average of 4.3mD.

The thin section photomicrograph (TS) and scanning electron micrograph of a representative sample in hydraulic unit 2 is described in details in Appendix-A.

Mercury injection

Figure 5.7 shows typical mercury intrusion capillary pressure curve of hydraulic unit 2 and the pore throat size distribution calculated from the mercury data. The pores are classified mainly as meso and some micro pores as they are dominated by pore throats.

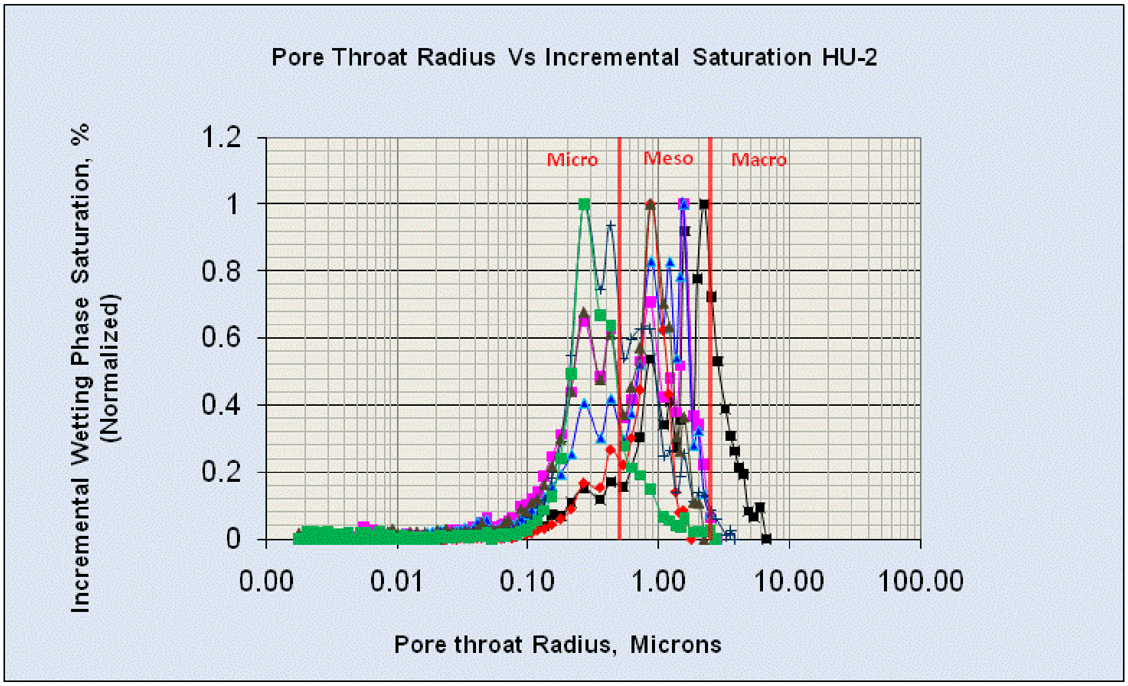

Figure 5.7: Pore throat size distribution from mercury data for hydraulic unit 2

5.5.3 Hydraulic Unit 3

Hydraulic unit 3 is classified mainly as Bioclastic Wackestone which is the dominant facies in this hydraulic unit and some Bioclastic Peloidal Packstone. The samples of this facies show very poor to poor reservoir quality which show high amounts of micritic matrix that should contain significant amounts of microporosity. Types of the macro porosity are mainly moldic porosity or primary intraparticle porosity, both commonly are classified as non- effective porosity. Therefore it is expected that the samples display poor reservoir. The samples show gas permeabilities ranging from 1.1 to 6.8 mD with an average of 2.8 mD.

The thin section photomicrograph (TS) and scanning electron micrograph of a representative sample in hydraulic unit 3 is described in details in Appendix-A.

Mercury injection

Figure 5.8 shows typical mercury intrusion capillary pressure curve of hydraulic unit 3 and the pore throat size distribution calculated from the mercury data. The pores are classified as micro pores as they are dominated by pore throats.

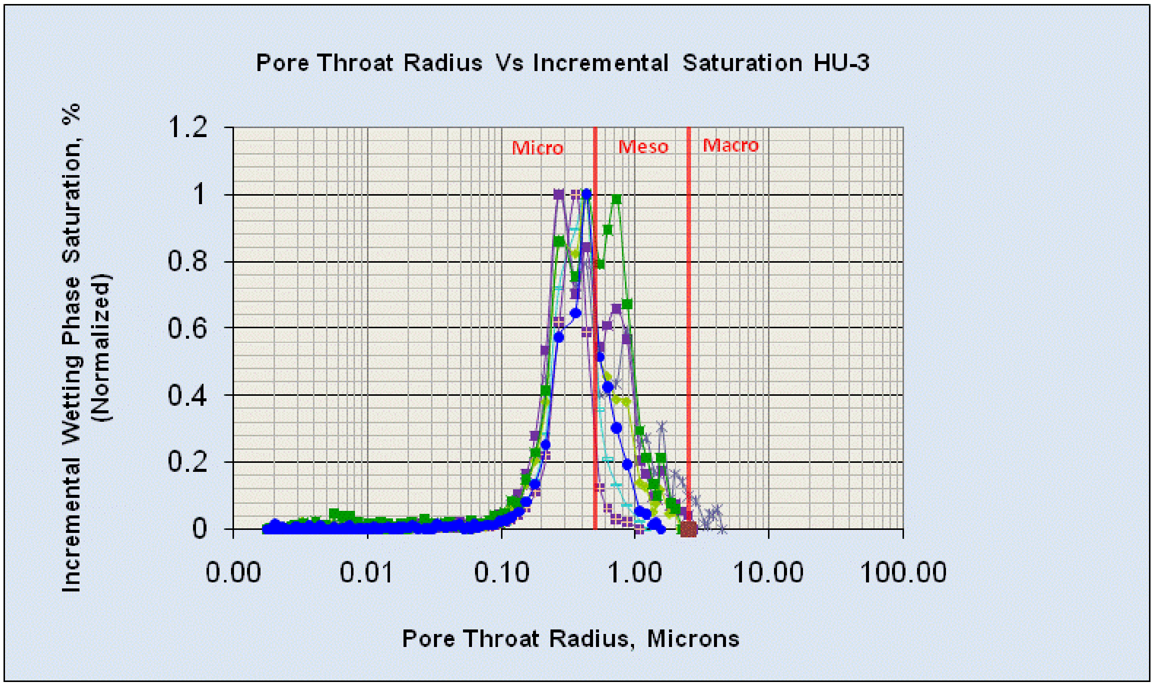

Figure 5.8: Pore throat size distribution from mercury data for hydraulic unit 3

XRD Analysis

X-ray analyses of samples from two reservoir intervals show distinct patterns. As shown in Table 5.3, calcite is the most abundant mineral in the upper interval (Reservoir D), ranging from 1.4 percent to 99 percent (average= 66%). Lower calcite contents are coupled with higher dolomite values (dolomitization and dolomite cement). The average dolomite content is 33%.

The lower interval (Reservoir F) shows predominantly calcite.

Table 5.3: X-RAY Diffraction results (whole Rock)

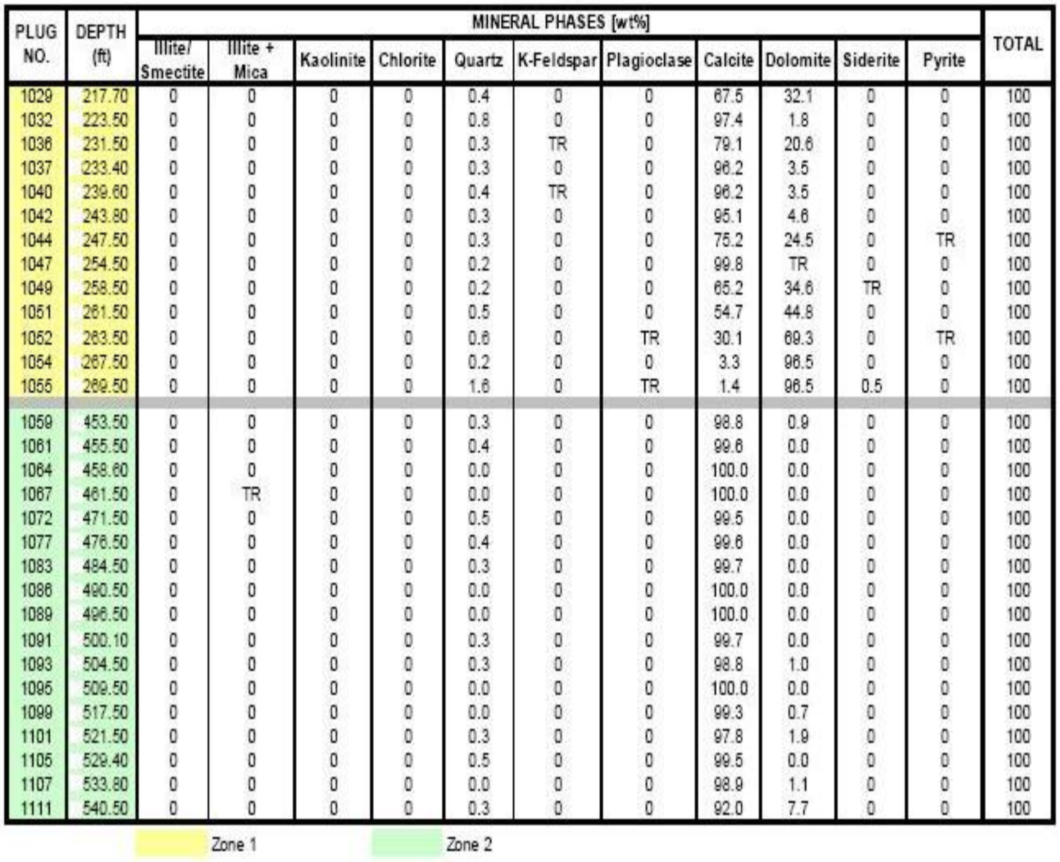

PLUG NO.	DEPTH (ft)	MINERAL PHASES [wt%]											TOTAL
		Illite/ Smectite	Illite + Mica	Kaolinite	Chlorite	Quartz	K-Feldspar	Plagioclase	Calcite	Dolomite	Siderite	Pyrite	
1029	217.70	0	0	0	0	0.4	0	0	67.5	32.1	0	0	100
1032	223.50	0	0	0	0	0.8	0	0	97.4	1.8	0	0	100
1036	231.50	0	0	0	0	0.3	TR	0	79.1	20.6	0	0	100
1037	233.40	0	0	0	0	0.3	0	0	96.2	3.5	0	0	100
1040	239.60	0	0	0	0	0.4	TR	0	96.2	3.5	0	0	100
1042	243.80	0	0	0	0	0.3	0	0	95.1	4.6	0	0	100
1044	247.50	0	0	0	0	0.3	0	0	75.2	24.5	0	TR	100
1047	254.50	0	0	0	0	0.2	0	0	99.8	TR	0	0	100
1049	258.50	0	0	0	0	0.2	0	0	65.2	34.6	TR	0	100
1051	261.50	0	0	0	0	0.5	0	0	54.7	44.8	0	0	100
1052	263.50	0	0	0	0	0.6	0	TR	30.1	69.3	0	TR	100
1054	267.50	0	0	0	0	0.2	0	0	3.3	96.5	0	0	100
1055	269.50	0	0	0	0	1.6	0	TR	1.4	96.5	0.5	0	100
1059	453.50	0	0	0	0	0.3	0	0	98.8	0.9	0	0	100
1061	455.50	0	0	0	0	0.4	0	0	99.6	0.0	0	0	100
1064	458.60	0	0	0	0	0.0	0	0	100.0	0.0	0	0	100
1067	461.50	0	TR	0	0	0.0	0	0	100.0	0.0	0	0	100
1072	471.50	0	0	0	0	0.5	0	0	99.5	0.0	0	0	100
1077	476.50	0	0	0	0	0.4	0	0	99.6	0.0	0	0	100
1083	484.50	0	0	0	0	0.3	0	0	99.7	0.0	0	0	100
1086	490.50	0	0	0	0	0.0	0	0	100.0	0.0	0	0	100
1089	496.50	0	0	0	0	0.0	0	0	100.0	0.0	0	0	100
1091	500.10	0	0	0	0	0.3	0	0	99.7	0.0	0	0	100
1093	504.50	0	0	0	0	0.3	0	0	98.8	1.0	0	0	100
1095	509.50	0	0	0	0	0.0	0	0	100.0	0.0	0	0	100
1099	517.50	0	0	0	0	0.0	0	0	99.3	0.7	0	0	100
1101	521.50	0	0	0	0	0.3	0	0	97.8	1.9	0	0	100
1105	529.40	0	0	0	0	0.5	0	0	99.5	0.0	0	0	100
1107	533.80	0	0	0	0	0.0	0	0	98.9	1.1	0	0	100
1111	540.50	0	0	0	0	0.3	0	0	92.0	7.7	0	0	100

🟨 Zone 1
🟩 Zone 2

CHAPTER 6

RESULTS AND DISCUSSION

FORMATION FACTOR

The saturated core resistivities (R_o), saturating brine resistivity (R_w) and porosities were used to calculate the formation factors (F) and cementation exponents (m) of each core plug at ambient and overburden pressure and temperature (Table 6.1) for two reservoirs.

Ambient condition

Cementation exponents are calculated at temperature of 70 ºF and pressure of 0 psig for each core plug and range from 1.91 to 2.07.

Overburden condition

Cementation exponents are calculated at temperature of 215 ºF and pressure of 4243 psig for reservoir-D and 4765 psig for reservoir-F and range from 2.06 to 2.21.

Table 6.1: Formation factor (F) and cementation exponent (m) at ambient and overburden pressures and temperatures.

Sample	Depth (ft)	Test Temperature (°F)	Overburden psig	Porosity (%)	Rw (Ω.m)	Ro (Ω.m)	Formation Resistivity Factor	Cementation exponent (m)
1030	X219.5	70	0	13.2	0.0520	2.474	47.58	1.91
		215	4243	12.2	0.0165	1.248	75.61	2.06
1047	X254.5	70	0	19.2	0.0520	1.362	26.19	1.98
		215	4243	17.6	0.0165	0.595	36.08	2.06
1054	X267.5	70	0	15.4	0.0520	2.492	47.93	2.07
		215	4243	14.4	0.0165	1.203	72.90	2.21
1075	Y474.5	70	0	20.3	0.0520	1.204	23.16	1.97
		240	4765	19.1	0.0145	0.485	33.42	2.12
1077	Y476.5	70	0	17.5	0.0520	1.639	31.52	1.98
		240	4765	16.4	0.0165	0.638	44.03	2.09
1094	Y507.5	70	0	22.4	0.0520	1.017	19.55	1.99
		240	4765	21.2	0.0165	0.372	25.63	2.09
1110	Y539.6	70	0	14.7	0.0520	2.760	53.07	2.07
		240	4765	13.7	0.0165	1.061	73.14	2.16

Generally the equation ($F = a / \varphi^{m}$), in forced fit, a =1 and $F= 1 / \varphi^{m}$ and in free fit, “a” can take any value in the intercept. But there is nothing unique about the intercept “a”. Therefore, $F= 1 / \varphi^{m}$ is used in the laboratory reporting and log processing. In free fit, the “a“ value was determined to be very close to 1.

Formation Factor (F) was plotted versus Porosity (fraction) on a log-log plot. An average line fit through the data points and unity using a least squares linear regression, identified the cementation exponent (m), the slope of the line. Using the fitted line through unity forces a value of 1 for ‘a’. The composite m value at ambient condition is 1.99 (Figure 6.1) and the composite m value at overburden condition is 2.11 (Figure 6.2).

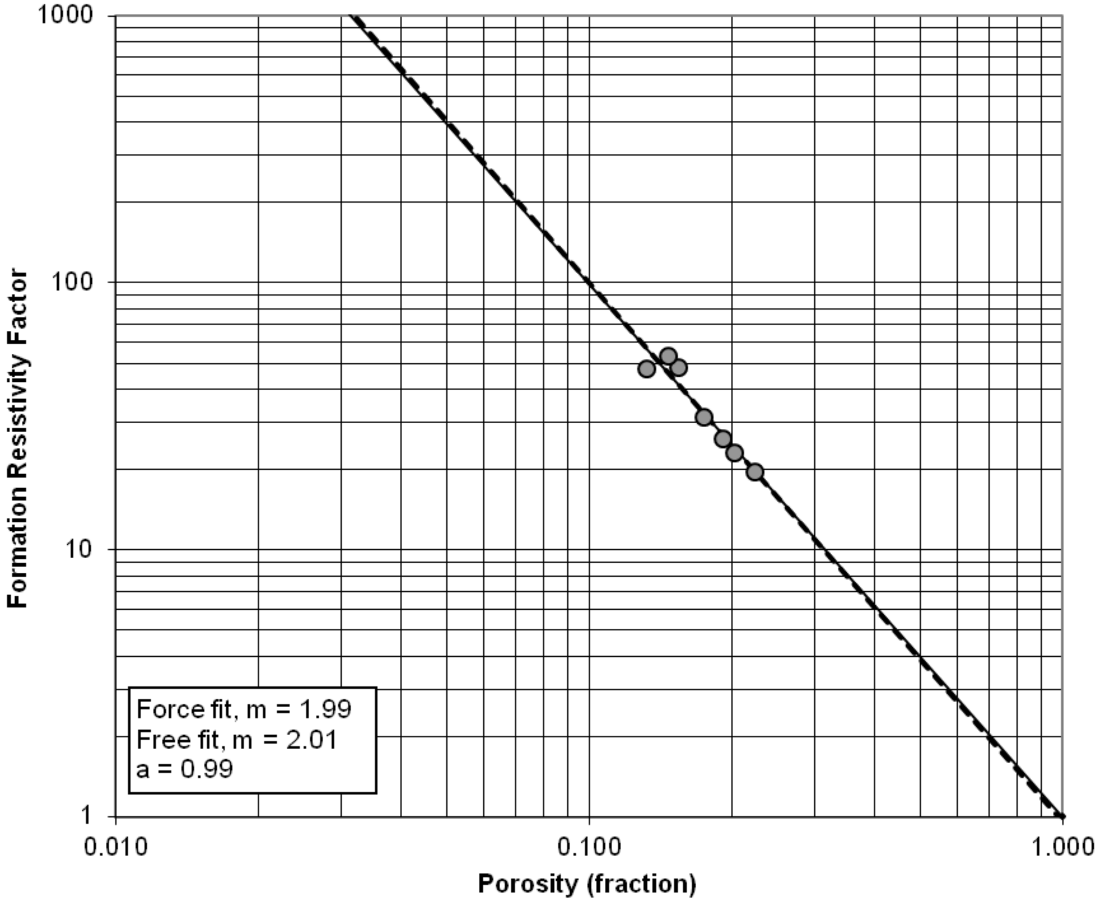

Figure 6.1: Porosity vs formation resistivity factor at Ambient condition

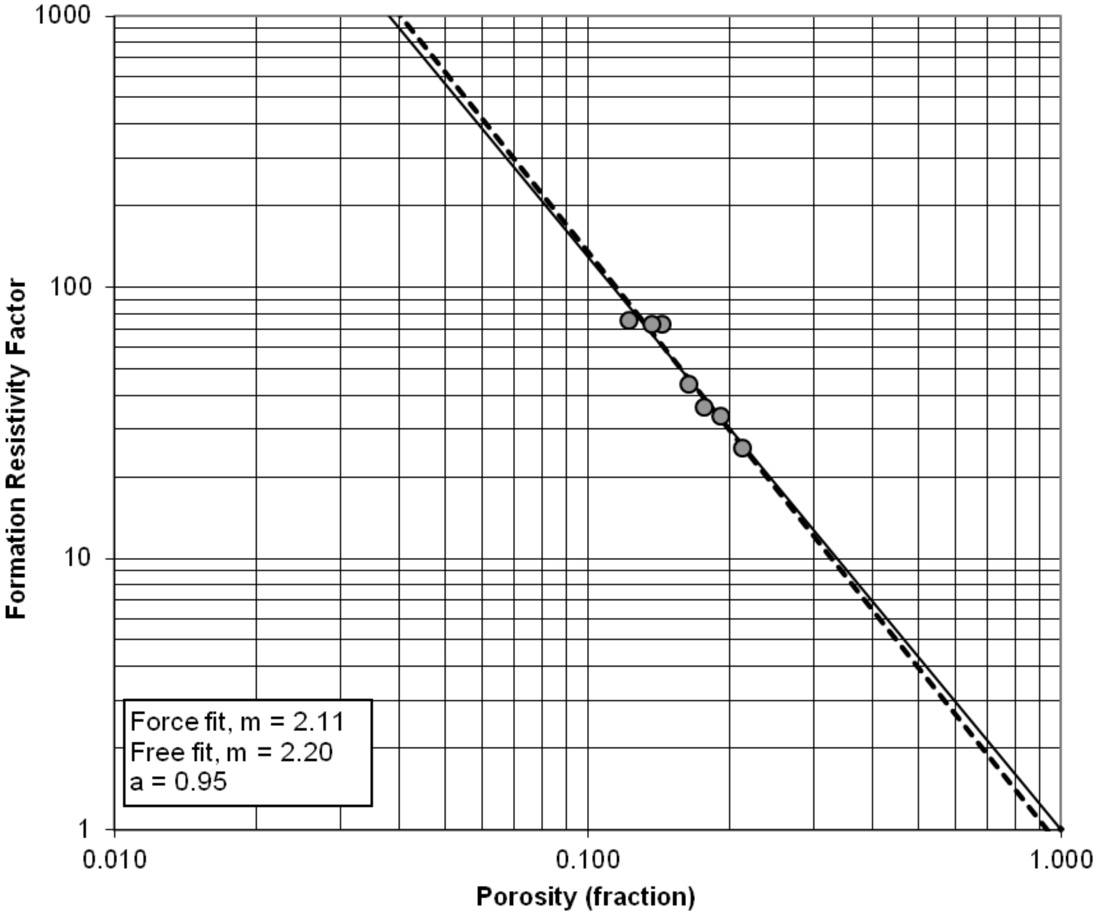

Figure 6.2: Porosity vs formation resistivity factor at elevated temperature and overburden pressure.

4.2.7 Resistivity Index with Gas-Water Capillary Pressure by Porous-Plate

After formation factor testing, The Resistivity index was measured for each core plug at overburden condition for two reservoirs (Table 6.2).

Table 6.2: The overburden condition for each plug sample

Sample	Depth (ft)	Test Temperature (ºF)	Overburden Pressure (psig)	Porosity @ Ovb (%)	PV @ Ovb (cc)
1030	X219.5	215	4243	12.2	6.48
1047	X254.5	215	4243	17.6	9.21
1054	X267.5	215	4243	14.4	7.52
1075	Y474.5	240	4765	19.1	9.87
1077	Y476.5	240	4765	16.4	8.77
1094	Y507.5	240	4765	21.2	11.35
1110	Y539.6	240	4765	13.7	7.02

From porous-plate experiment the brine production and the corresponding sample resistivity (Rt) are recorded (Table 6.4) thought the desaturation process at different capillary pressures. (Table 6.3).

Table 6.3: The Brine production at each capillary pressure

Sample	Depth (ft)	Brine Out (cc) at Capillary Pressure (psig)							
		0.5	1	2	4	8	16	32	75
1030	X219.5	0.20	0.76	1.64	2.75	3.70	4.42	4.83	5.15
1047	X254.5	0.96	1.85	3.13	4.61	5.93	6.65	7.13	7.46
1054	X267.5	1.38	2.17	3.38	4.18	4.93	5.52	5.94	6.31
1075	Y474.5	0.17	1.21	2.18	3.55	5.32	6.53	7.13	7.55
1077	Y476.5	0.08	0.44	0.89	1.92	3.53	5.04	5.65	6.11
1094	Y507.5	0.78	1.94	3.75	5.51	7.14	8.18	8.73	9.27
1110	Y539.6	0.09	0.36	1.07	2.08	3.23	4.34	4.68	5.05

Table 6.4: The sample resistivity at each capillary pressure

Sample	Depth (ft)	Rt at Capillary Pressure (psig)							
		0.5	1	2	4	8	16	32	75
1030	X219.5	-	1.62	2.40	4.19	7.35	14.63	24.43	36.62
1047	X254.5	0.76	0.96	1.51	2.75	5.55	10.16	15.47	23.46
1054	X267.5	1.89	2.67	4.64	7.82	13.09	25.03	42.85	81.85
1075	Y474.5	-	0.65	0.83	1.31	2.77	5.54	9.14	13.84
1077	Y476.5	-	-	0.81	1.11	2.08	4.75	6.09	9.05
1094	Y507.5	-	0.56	0.91	1.61	3.26	6.55	9.28	16.51
1110	Y539.6	-	-	1.54	2.32	4.54	10.62	13.51	20.39

The Resistivity index (RI) were calculated from R_o and R_t measurements and the results are shown in Table 6.5:

Table 6.5: The resistivity Index result at each capillary pressure

Sample	Depth (ft)	Ro @ Ovb (Ω.m)	RI at Capillary Pressure (psig)							
			0.5	1	2	4	8	16	32	75
1030	X219.5	1.25	-	1.30	1.92	3.36	5.89	11.73	19.58	29.35
1047	X254.5	0.60	1.27	1.62	2.54	4.62	9.33	17.06	25.99	39.41
1054	X267.5	1.20	1.57	2.22	3.86	6.50	10.88	20.81	35.62	68.05
1075	Y474.5	0.48	-	1.35	1.72	2.70	5.72	11.43	18.86	28.55
1077	Y476.5	0.64	-	-	1.27	1.74	3.26	7.44	9.54	14.18
1094	Y507.5	0.37	-	1.50	2.45	4.32	8.76	17.62	24.98	44.43
1110	Y539.6	1.06	-	-	1.45	2.19	4.28	10.01	12.74	19.23

The corresponding core sample saturations were calculated from brine displacement measurements (Table 6.6)

Table 6.6: The core sample saturations at each capillary pressure.

Sample	**Depth (ft)**	**Gas Permeability @ 400 psig (mD)**	**BRINE SATURATION (% PORE VOLUME) AT CAPILLARY PRESSURE (PSIG)**							
			0.5	**1**	**2**	**4**	**8**	**16**	**32**	**75**
1030	X219	3.93	96.9	88.3	74.6	57.5	42.8	31.8	25.4	20.5
1047	X254	89.82	89.6	79.9	66.0	49.9	35.6	27.8	22.6	19.0
1054	X267	146.50	81.7	71.1	55.1	44.5	34.5	26.6	21.1	16.2
1075	Y474	3.84	98.3	87.7	77.9	64.0	46.1	33.8	27.8	23.5
1077	Y476	1.55	99.1	95.0	89.8	78.1	59.8	42.5	35.6	30.4
1094	Y507	19.90	93.1	82.9	67.0	51.5	37.1	28.0	23.1	18.3
1110	Y539	0.94	98.7	94.9	84.8	70.3	54.0	38.2	33.3	28.1

The least squares linear regression plot for resistivity index (RI) versus water saturation (S_w) fitted through unity (1,1) yielded a line whose slope defines the composite n (Figure 6.10). The Individual saturation exponent n values (Figures 6.3-6.9) which also can be calculated using the formula were calculated using the formula (Table 6.7)

Table 6.7: Summary of Resistivity Index and Saturation exponents

Sample # 1030			
Ro = 1.2 (Ω.m)		n = 2.14	
C.P. (Psig)	Rt (Ω.m)	Sw	RI
1.00	1.62	0.88	1.30
2.00	2.40	0.75	1.92
4.00	4.19	0.58	3.36
8.00	7.35	0.43	5.89
16.00	14.63	0.32	11.73
32.00	24.43	0.25	19.58
Sample # 1047			
Ro = 0.6 (Ω.m)		n = 2.20	
C.P. (Psig)	Rt (Ω.m)	Sw	RI
0.50	0.76	0.90	1.27
1.00	0.96	0.80	1.62
2.00	1.51	0.66	2.54
4.00	2.75	0.50	4.62
8.00	5.55	0.36	9.33
16.00	10.16	0.28	17.06
32.00	15.47	0.23	25.99
Sample # 1054			
Ro = 1.2 (Ω.m)		n = 2.30	
C.P. (Psig)	Rt (Ω.m)	Sw	RI
0.50	1.89	0.82	1.57
1.00	2.67	0.71	2.22
2.00	4.64	0.55	3.86
4.00	7.82	0.45	6.50
8.00	13.09	0.35	10.88
16.00	25.03	0.27	20.81
32.00	42.85	0.21	35.62
Sample # 1075			
Ro = 0.48 (Ω.m)		n = 2.28	
C.P. (Psig)	Rt (Ω.m)	Sw	RI
1.00	0.65	0.88	1.35
2.00	0.83	0.78	1.72
4.00	1.31	0.64	2.70
8.00	2.77	0.46	5.72
16.00	5.54	0.34	11.43
32.00	9.14	0.28	18.86
Sample # 1077			
Ro = 0.64 (Ω.m)		n = 2.24	
C.P. (Psig)	Rt (Ω.m)	Sw	RI
2.00	0.81	0.90	1.27
4.00	1.11	0.78	1.74
8.00	2.08	0.60	3.26
16.00	4.75	0.43	7.44
32.00	6.09	0.36	9.54
Sample # 1094			
Ro = 0.37 (Ω.m)		n = 2.22	
C.P. (Psig)	Rt (Ω.m)	Sw	RI
1.00	0.56	0.83	1.50
2.00	0.91	0.67	2.45
4.00	1.61	0.52	4.32
8.00	3.26	0.37	8.76
16.00	6.55	0.28	17.62
32.00	9.28	0.23	24.98
Sample # 1110			
Ro = 1.06 (Ω.m)		n = 2.34	
C.P. (Psig)	Rt (Ω.m)	Sw	RI
2.00	1.54	0.85	1.45
4.00	2.32	0.70	2.19
8.00	4.54	0.54	4.28
16.00	10.62	0.38	10.01
32.00	13.51	0.33	12.74

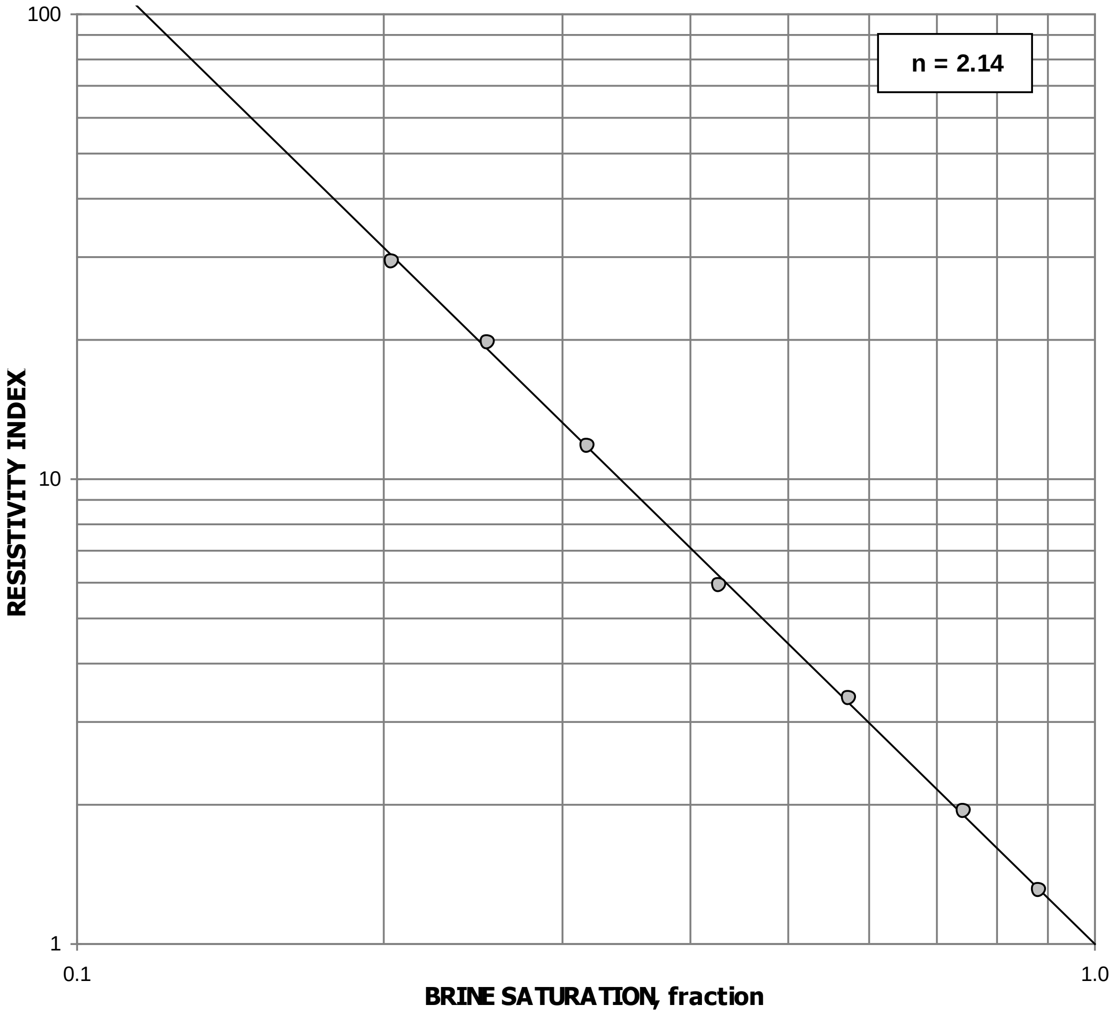

Figure 6.3: Saturation exponent determination of sample # 1030

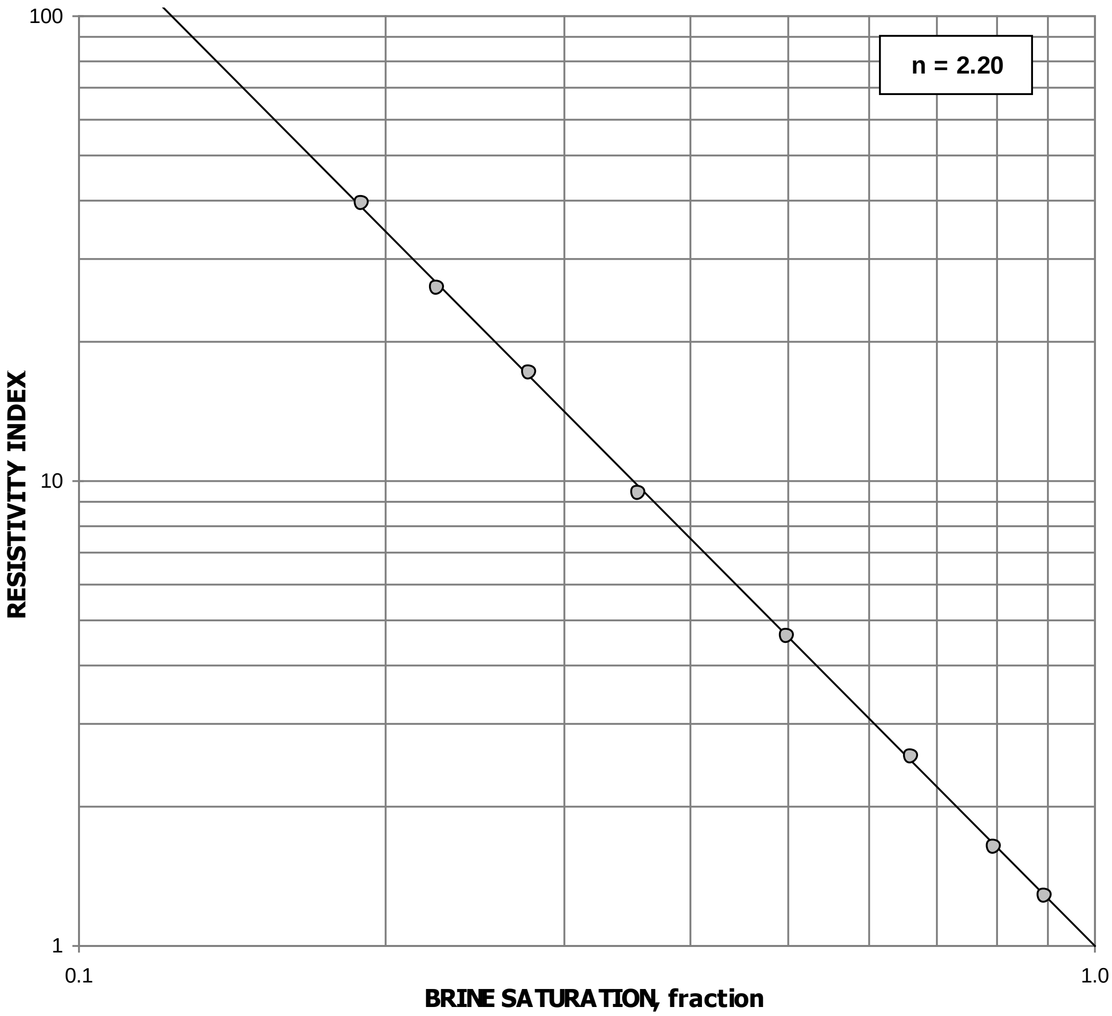

Figure 6.4: Saturation exponent determination of sample # 1047

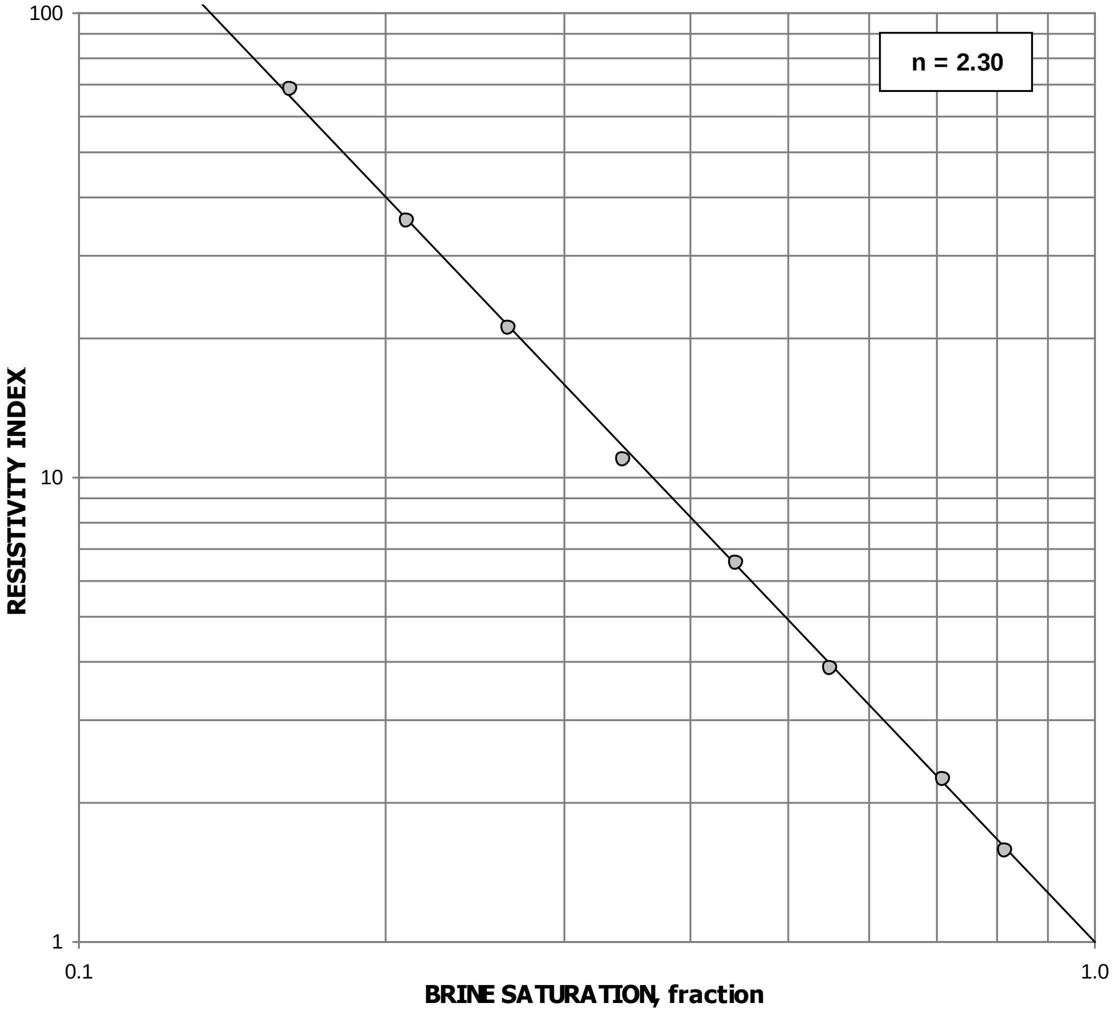

Figure 6.5: Saturation exponent determination of sample # 1054

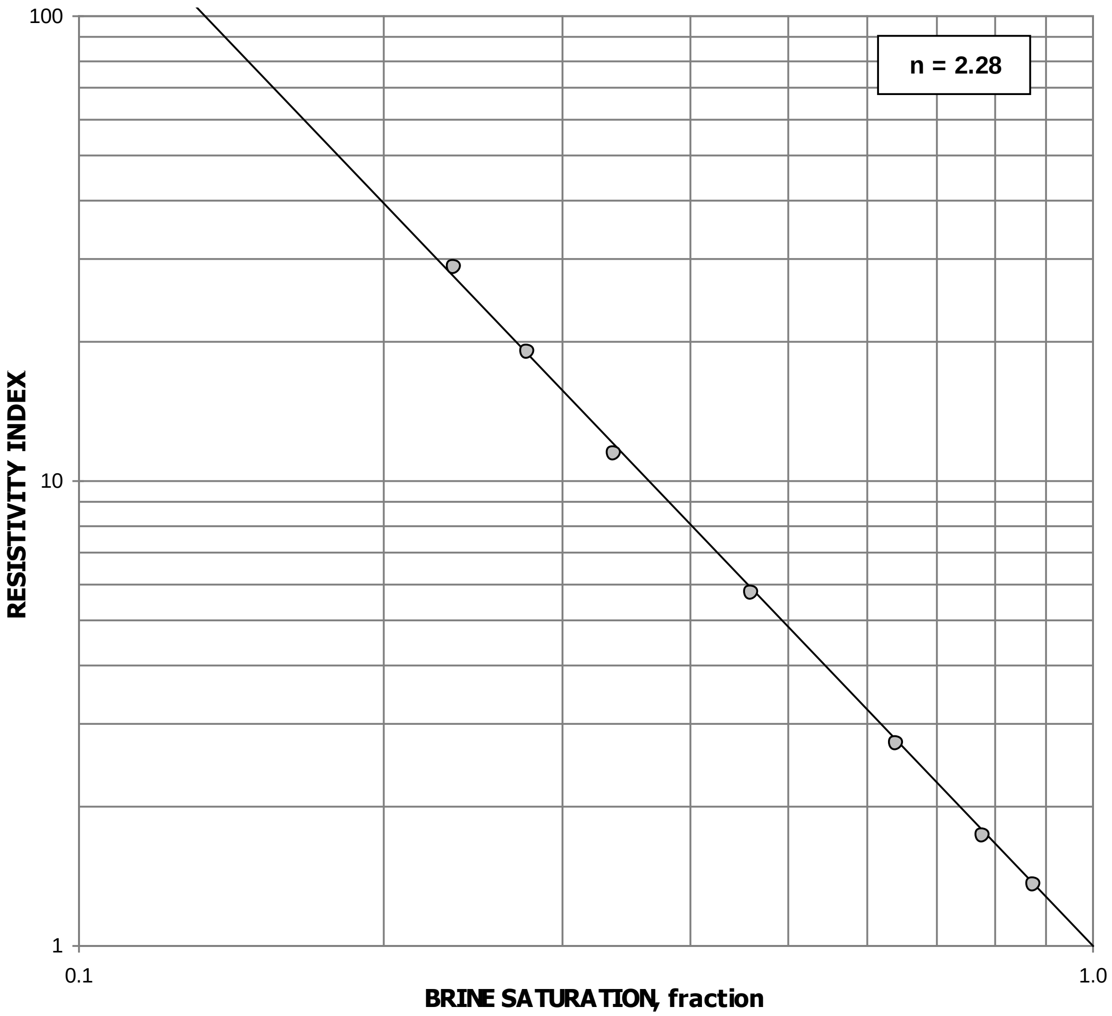

Figure 6.6: Saturation exponent determination of sample # 1075

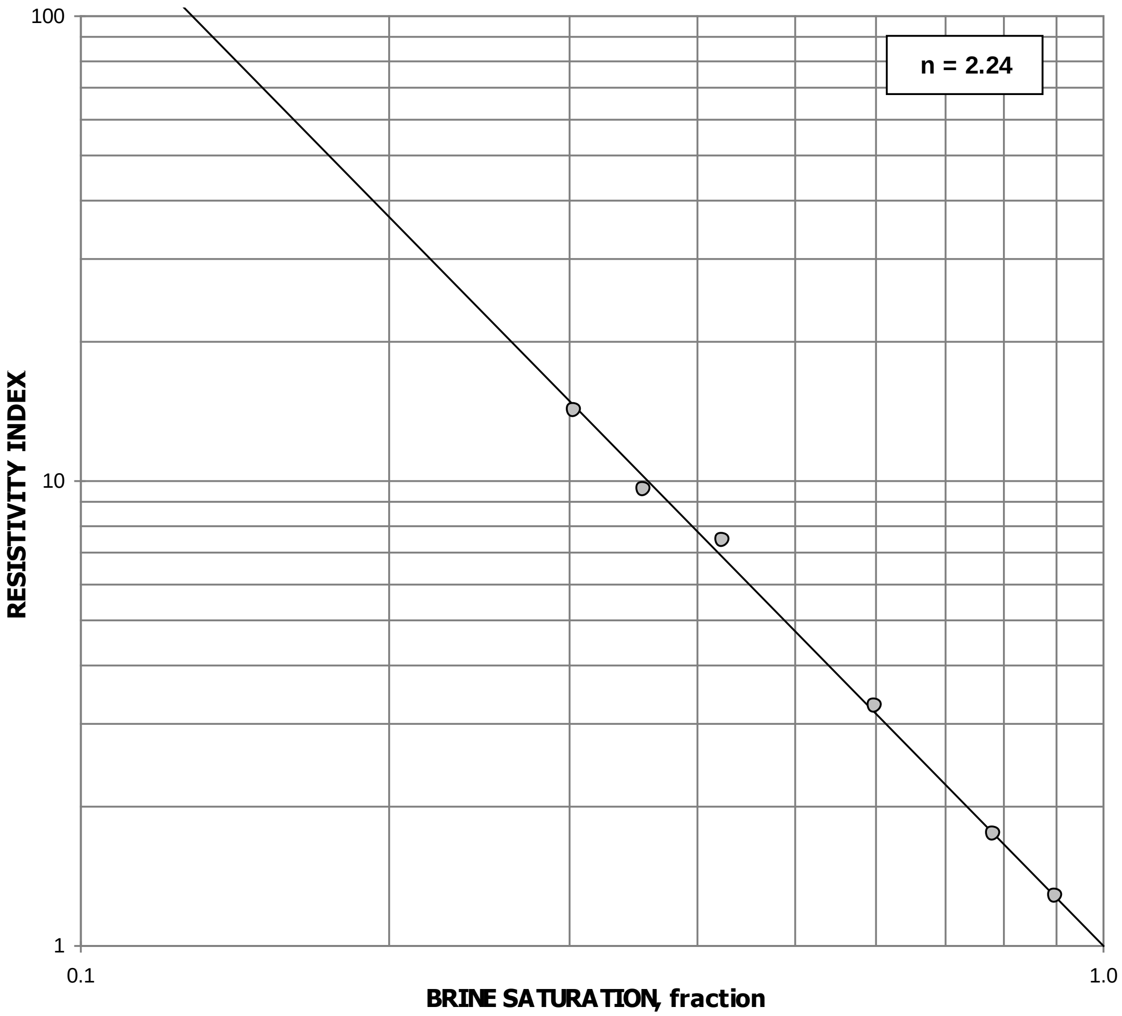

Figure 6.7: Saturation exponent determination of sample # 1077

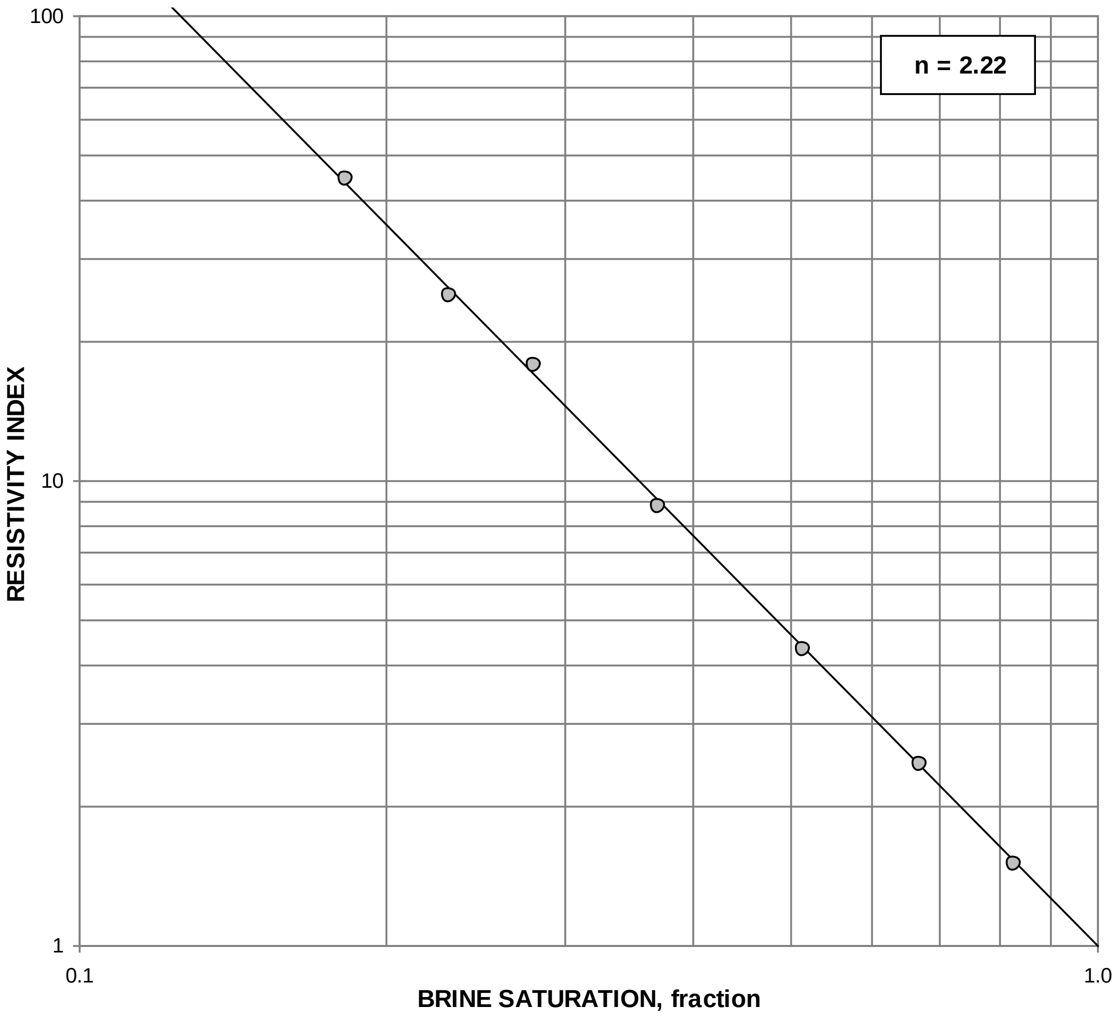

Figure 6.8: Saturation exponent determination of sample # 1094

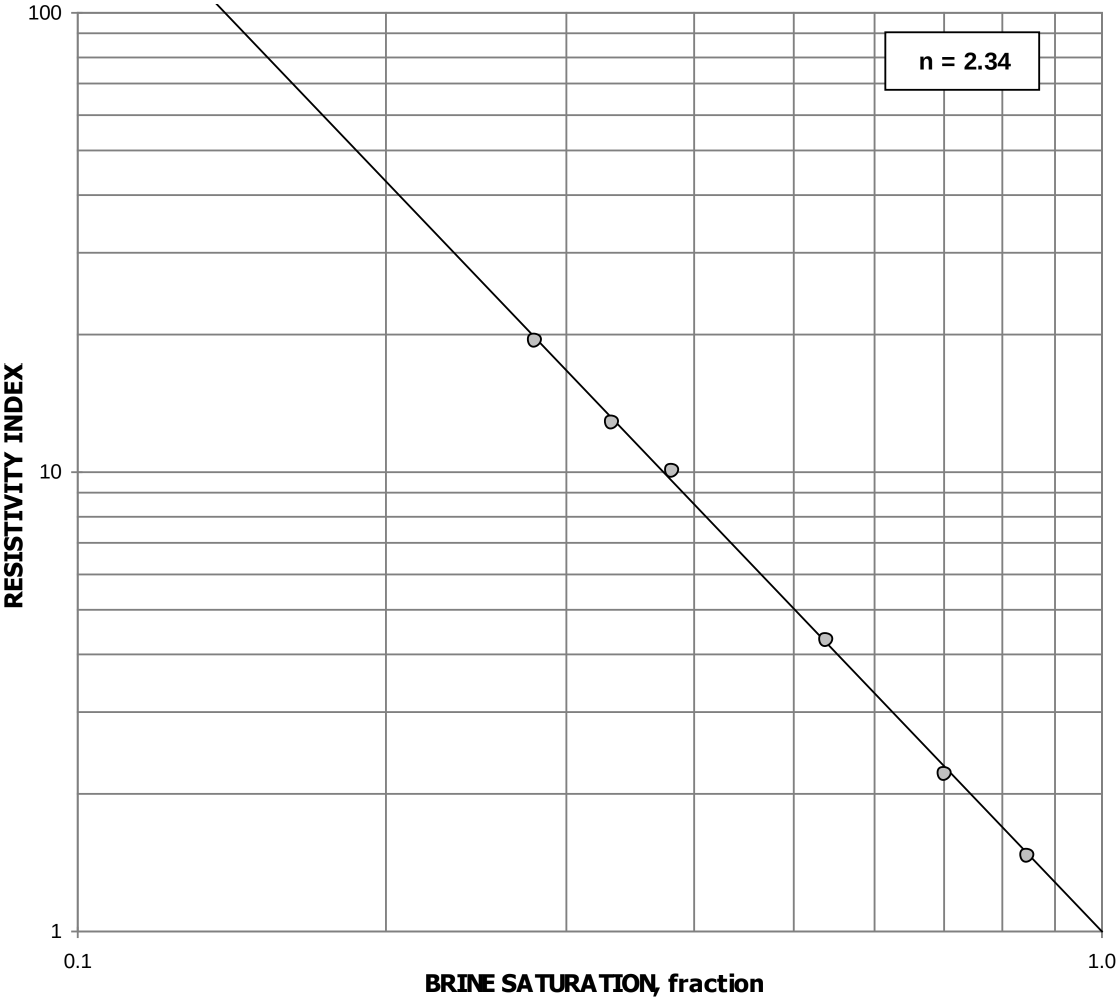

Figure 6.9: Saturation exponent determination of sample # 1110

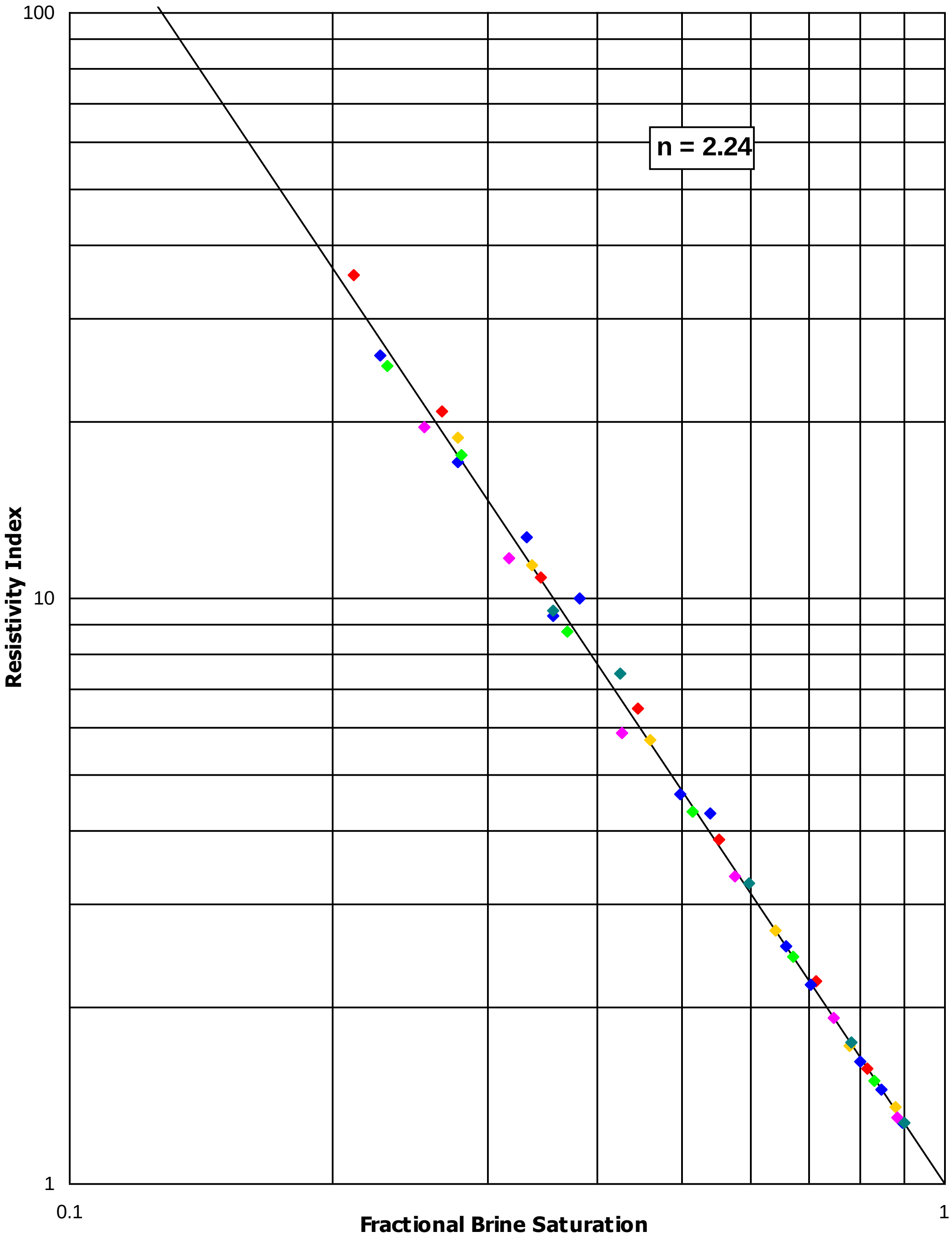

Figure 6.10: Composite Saturation exponent determination

Capillary pressures were plotted against corresponding stable saturations to provide capillary pressure curves for each sample (Figure 6.11 and 6.12).

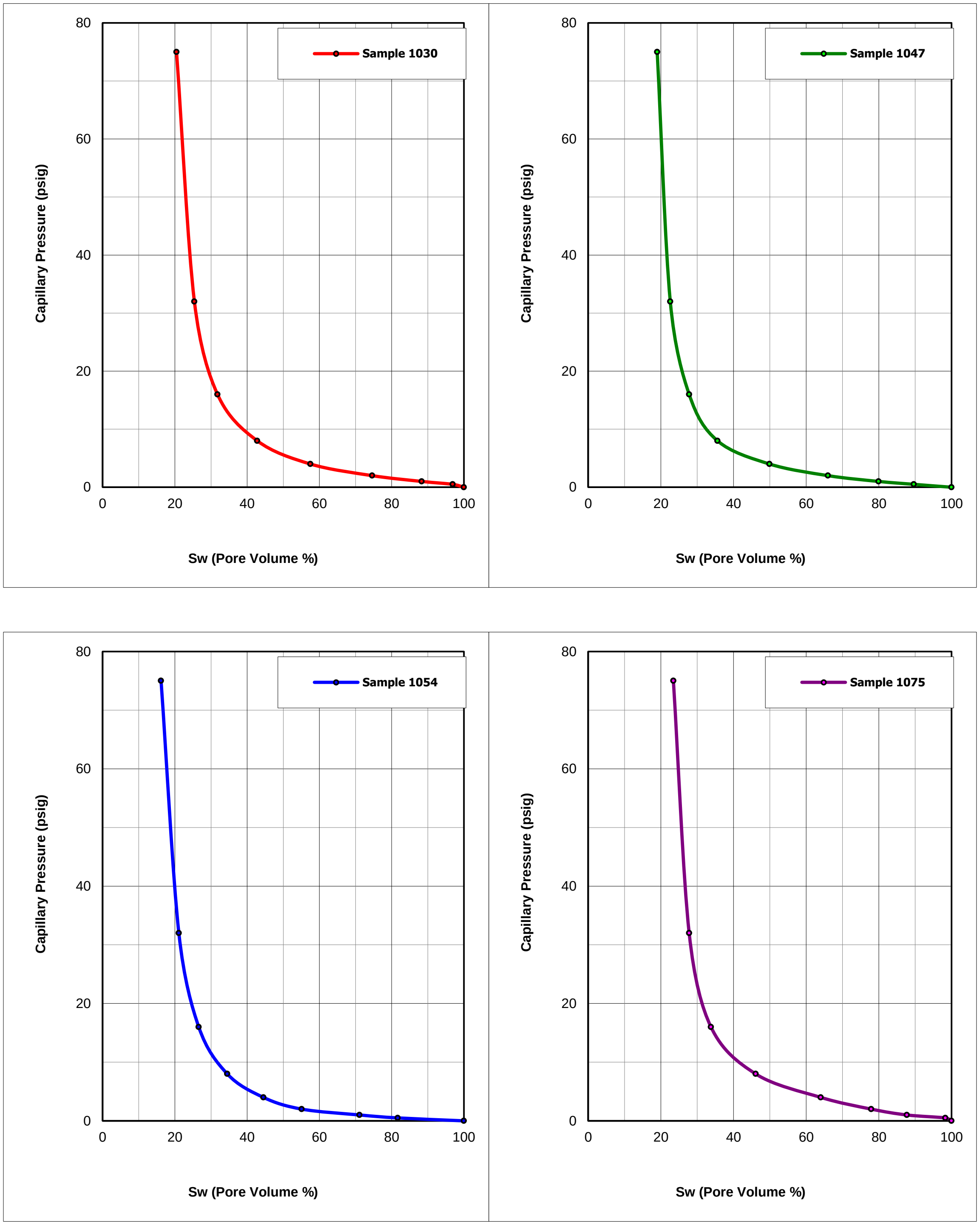

Figure 6.11: Oil/Brine capillary pressure curves of Sample # 1030, 1047, 1054 and 1075

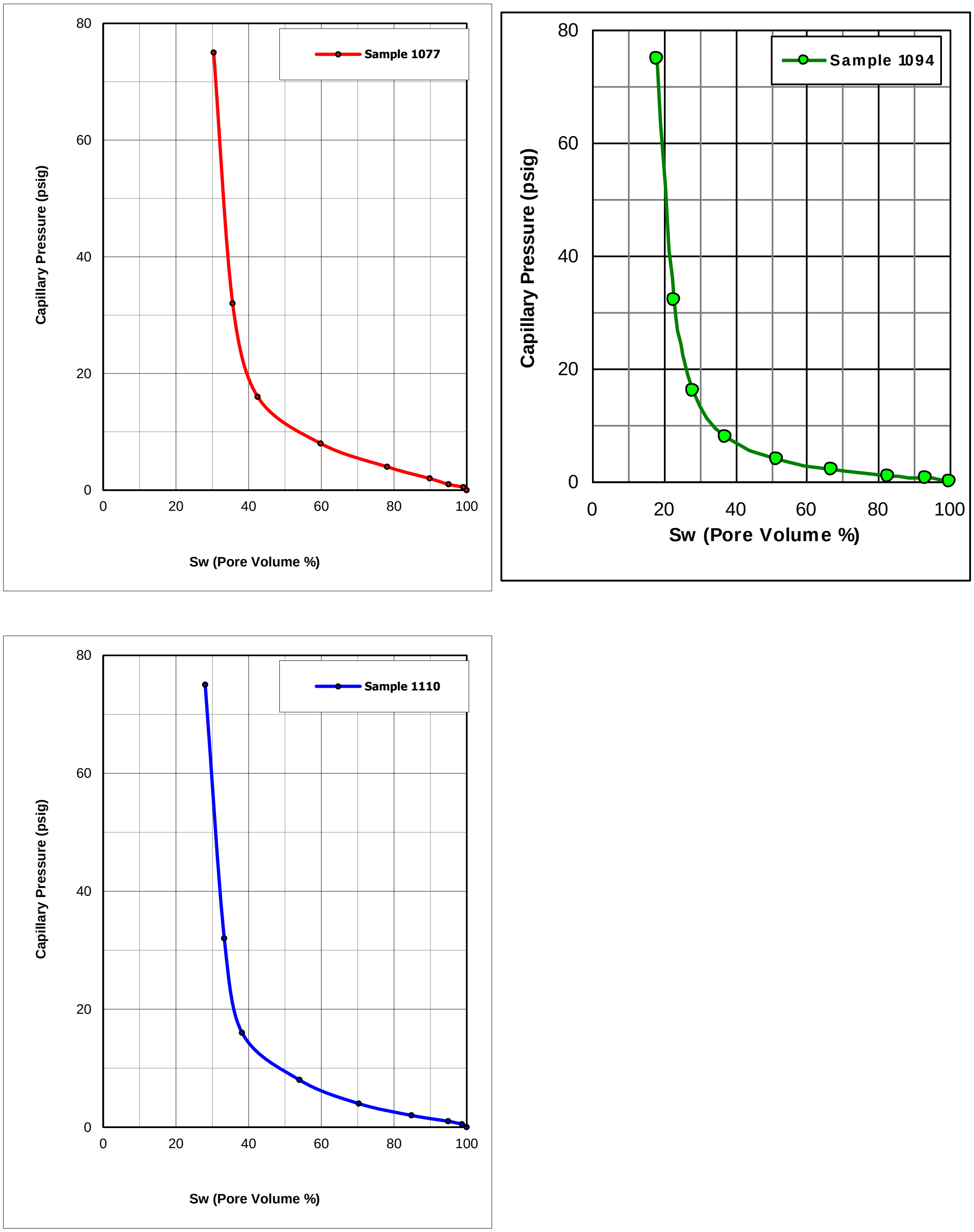

Figure 6.12: Oil/Brine capillary pressure curves of Sample # 1077, 1094 and 1110

The electrical properties of each hydraulic unit was determined based on the selected representative samples (Table 6.8).

Table 6.8: The electrical properties based on hydraulic units

HU #	**Sample #**	**Depth, ft**	**Sample**		**HU**	
			m	**n**	**m**	**n**
1	1054 1047	X267.5 X254.5	2.21 2.06	2.3 2.2	2.14	2.25
2	1030 1094	X219.5 Y507.5	2.06 2.09	2.14 2.22	2.075	2.19
3	1075 1077	Y474.5 Y476.5	2.12 2.09	2.28 2.24	2.1	2.27

The open hole logging data was utilized to calculate water saturation across two reservoirs (D and F) based on hydraulic units electrical properties and compared with the composite electrical properties values Using GEOLOG software and hydraulic unit model.

Reservoir-D results:

Water saturation is calculated across reservoir-D using the determined electrical properties based on hydraulic units and well composite values. The results show small difference in water saturation across different intervals when variable electrical parameters for different rock properties were used (Figure 6.13). The average water saturation shows a difference of 5.2 % (Table 6.9).

Reservoir-F results

Water saturation is calculated across reservoir-F using the determined electrical properties based on hydraulic units and well composite values. The results show minor difference in water saturation across the top of the reservoir where the more dolomite lithology is located due to the small variation in electrical parameters for different rock properties (Figure 6.14). The average water saturation shows a difference of 1.1 % (Table 6.9).

Table 6.9: Summary of average water saturation for Reservoir-D and F

Average Sw	**Reservoir-D**	**Reservoir-F**
Sw- HUs	0.420	0.192
Sw- composite	0.442	0.190
Difference %	5.3 %	1.1 %

Impact of hydraulic unites approach to the study well

There is 5.3% difference in water saturation when comparison is made between the hydraulic units derived electrical parameter versus well composite electrical parameters in reservoir-D. This reduction in water saturation is equivalent to a 5.3 % increase in oil in place as a result of using hydraulic units base electrical properties. On the other hand, Reservoir-F shows minor difference of 1.1% in Sw estimation.

Hydraulic units technique has further enhanced the electrical properties estimation because it categorized the rocks into common geological and petrophysical properties. Eventually, the electrical parameters will be assigned to a specific hydraulic unit instead of averaging it as it was when applying water saturation composite method. Thus, the hydraulic units technique should be a more accurate approach in assigning elecctrical parameters that leads to accurate water saturation estimation. The revised volume of hydrocarbon estimated using this method should further improve the field production history matching.

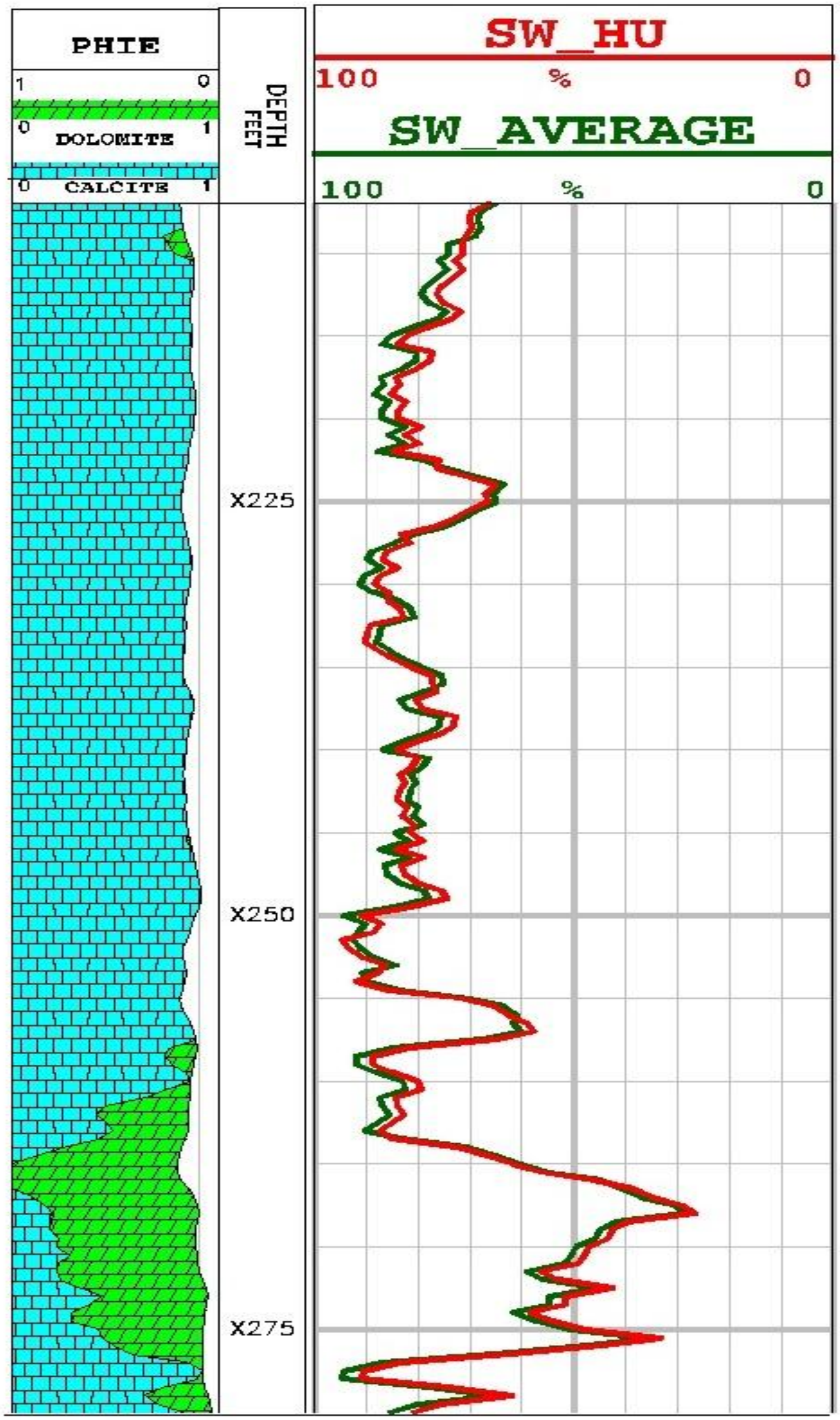

Figure 6.13: Water sturation determination across reservoir-D

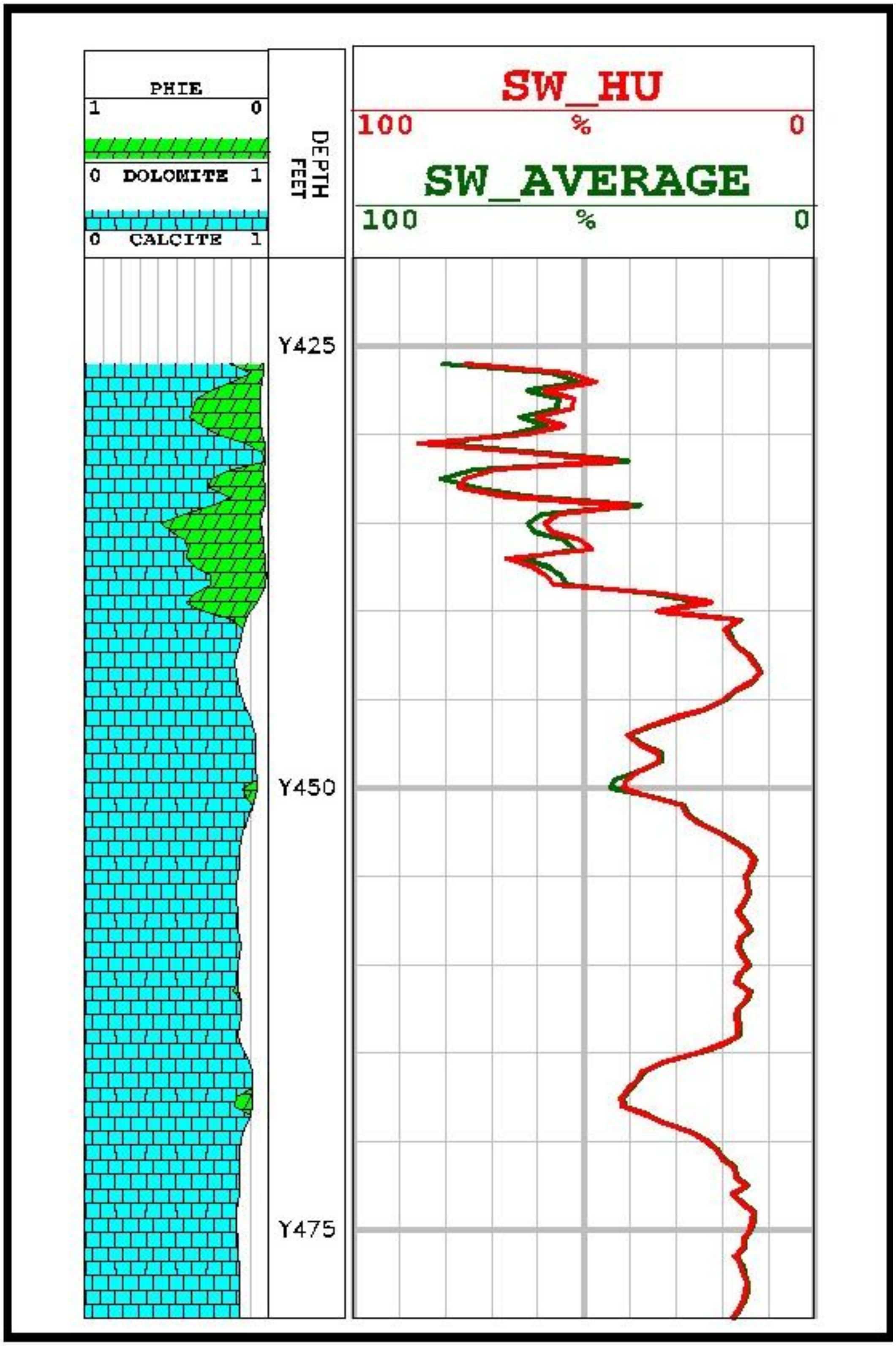

Figure 6.14: Water sturation determination across reservoir-F

CHAPTER 7

CONCLUSIONS AND RECOMMENDATIONS

7.1 Conclusions

1- Variable electrical properties are likely for multimodal pore systems where pores of different sizes can exert differential influences on the conduction of applied current as de-saturation progresses.

2- An unrecognized variation in n and m can induce a difference of more than 5 percent decrease in the petrophysical evaluation of water saturation.

3- The decrease in water saturation using hydraulic units technique is very significant, as this translates to an equivalent increase in oil-in-place estimation.

4- Hydraulic units technique has further enhanced the electrical properties estimation because it categorized the rocks into common geological and petrophysical properties.

5- Hydraulic units technique should be a more accurate approach in assigning electrical parameters that leads to accurate water saturation estimation.

6- The revised volume of hydrocarbon estimated using this method should further improve the field production history matching.

7.2 Recommendations

1. Hydraulic units methodology should be used to calculate water saturation for minimizing uncertainty where a variable m and n is suspected.
2. Hydraulic units should be used to discriminate the rock because it has direct relation to the rock petrophysical properties especially permeability.
3. Systematic rock classification using HU method will help to further improve Sw estimation because the electrical property was assigned to specific unit character.
4. The hydraulic units classification should be used to correlate the reservoir in order to have a first indication of potential fluid flow across an area.
5. Understanding the character of each hydraulic unit will help in completion strategy.
6. Hydraulic unit is the combination of geological and statistical approach in discriminating rock's petrophysical properties hence more samples are required in order to improve its accuracy.

REFERENCES

1. Archie, G.E. (1942). "The electrical resistivity log as an aid in determining some reservoir characteristics" Trans., AIME (1942) 146, 54-62.

2. Anderson W.G. (1986). Wettability literature survey - Part 3: The effects of wettability on the electrical properties of porous media. *JPT*, December, pp. 1371-1378.

3. Blum, H.A., and Martin, J.L., (1955). Log interpretation problem in low resistivity sands, SPE484-G, JPT, p.10.

4. Donaldson, E.L. and T.K. Siddiqui (1989). Relationship between the Archie saturation exponent and wettability. *SPE formation evaluation*, September, pp. 359-363.

5. Ebanks W.J. Jr (1987): "Flow Unit Concept-integrated approach to reservoir description for engineering projects" AAPG (AM. Assoc. Pet. Geol.) Bull., Vol/Issue:71:5, American Association of Petroluem Geologists Annual meeting, 7 Jun 1987, Los angeles, CA.

6. Stiles, J. H. Jr and Hutfilz, JM. (1988):" The use of routine and special core analysis in characterizing brent group reservoirs" UK north see SPE 18388 (1988).

7. Slatts. R.M. and Hopkins G.L. (1990): "Scaling Geologic reservoir description to engineering needs" JPT. V 42 No.2 (February 1990).

8. Chopra A.K. (1988): ”reservoir description Via puls” SPE 17568 int. meeting on petroleum engineering, Tianjin China (1988).

9. Amaefule, J. O., Altunbay, M., Tiab, D., Kersey, D., and Keelan, D. (1993): “Enhanced Reservoir description: Using Core and Log Data to Identify Hydraulic Flow and Predict Permeability in Uncored Intervals/Wells”. Paper SPE 26436 presented at the annual Technical conference and exhibition, Houston, , Oct. DOI: 10.2118/26436-MS.

10. Abbaszadeh, M., Fujii, H. and Fujimoto, F. (1996): “Permeability Prediction by Hydraulic Flow Units – Theory and Applications,” paper SPE 30158, *SPE Formation Evaluation Journal*, December, 1996.263-271.

11. Carman, P.C. (1937): “Fluid Flow through Granular Beds,” *Trans. Inst. Chem. Eng.* (1937) 15, 150.

12. Davies, D.K. and Vessell, R.K. (1996): ”Identification and Distribution of Hydraulic Flow Units in a Heterogeneous Carbonate Reservoir: North Robertson Unit, West Texas,” paper SPE 35183 presented at the Permain Basin Oil and Gas Recovery Conference, Midland, Texas, 27-29 March 1996.

13. Haro, C. F. (2007): “Permeability Modeling in Porous Media: Setting Archie and Carmen-Kozeny Right,” paper SPE 100201, presented at the 2007 international Oil Conference and Exhibition, Veracruz, Mexico, 27-30 June 2007.

14. Maclean O. Amabeoku, David G. Kersey, Rami H. BinNasser, Hisham H. Mohammadi, (2009): “Strategies for Acquiring and Integrating Petrophysical Data for Reservoir Evaluation” SPE 125169.

15. Dunham, R.J. (1962). Classification of carbonate rocks according to depositional texture – Mem. Amer. Ass. Petrol. Geol., 1, p.108-121

16. Fluegel, E. (2004). Microfacies of carbonate rocks - Springer, Berlin, 976 pp.

17. Sibley, D.F. and Gregg, J.M. (1981). Classification of dolomite rock textures – Jour. Sed. Research, 57/6, p. 967-975

18. Mitra Chekani, Petroiran Development Company, Riyaz Kharrat, SPE, (2009). “Reservoir Rock Typing in a Carbonate reservoir” SPE 123703.

19. Libny Leal, Roberto Barbato, Alfonso Quaglia, Juan Porras and Hugo Lazarde, (2001). “Bimodal Behavior of Mercury-injection Capillary Pressure Curve and its relationship to Pore Geometry, rock-Quality and Performance on Laminated and Heterogeneous Reservoir”. SPE 69457.

20. Winland H. D.(1972): Oil accumulation in Response to pore Size changes, Weyburn field, Saskatchewan, Amoco Production Research Report No. F25-G25, 1972.

APPENDIX A

GEOLOGICAL CHARACTERIZATION OF HYDRAULIC UNITS

APPENDIX *A*

Hydraulic unit 1 Geological descriptions

The thin section photomicrograph (TS) and scanning electron micrograph of a representative sample in hydraulic unit 1 is described in details as the following:

Thin section description

This representative sample (1047) is classified as Bioclastic Peloidal Grainstone. This sample has gas permeability of 98.8 mD, 19.2% porosity and grain density of 2.71 g/cc. (From core LAB measurements)

Textural Characteristics

The analysed sample contains carbonate fragments which are partially to completely micritised; primary structures of carbonate grains mainly are obliterated by micritisation and recrystallisation of micrite to microsparite, due to neomorphism most of bioclasts cannot be accurately identified. Carbonate grains show variable amounts of dissolution and replacement by calcite.

Carbonate grains do not show any preferentially orientation and some grains show boring on the surface. The sample had undergone a fair degree of compaction, grain contacts are mainly long contact with some sutured and concavo-convex contacts.

Carbonate Grains

Common **peloids** (16.7% of the point count; Plate 15b, D6), common **foraminifera** (19.7% of the point count; Plate 15b, I3-4) and few **echinoderm fragments** (5.7% of the point count; Plate 15a, I9) are recorded in the sample. All bioclasts are partially to completely micritised and recrystallised to microsparite, some of them can not be accurately identified; these are counted as **undifferentiated skeletal fragments** (23.0% of the point count; Plate 15b, H14).

Other Components

Traces of **hydrocarbon** (organic material) are noted in the sample.

Cementation

Very few dolomite cement is recorded in the sample (3.7% of the point count; Plate 15cb, D3); dolomite crystals mainly appear as pore filling cement and replacement of the carbonate grains. Few calcite cements, equant (Plate 15b, C14), syntaxial (Plate 15a, B4) and isopachous rim (Plate 15b, F4) cements are recorded in the sample within pore voids (12.3% of the point count).

Replacement and Neomorphism

Micrite is commonly replacing carbonate grains (Plate 15b, H14); primary structures of carbonate grains are obliterated by micritisation. Early stage of neomorphic microspar in parts replacing micrite.

Micrite and microsparite in parts are replaced by dolomite large crystals. Very few very fine dolomite crystals (micro dolomite) are noted in the sample (1.0% of the point count; Plate 15b, G10). Micro-dolomite replace primary micritic matrix.

Pore System

The sample shows mainly **primary interparticle porosity** (11.7% of the point count; Plate 15b, B5). **Secondary dissolution porosity** is recorded in the sample (6.3% of the point count; Plate 15b, C2-3). Dissolution porosity makes intraparticle porosity (Plate 15a, C5) as well as moldic porosity (Plate 15a, G11) which normally count as non-effective porosity, where such dissolution is more extensive these porosities are connected to the effective pore system.

The effective pore system in this sample has been significantly downgraded by calcite cement and in lesser amount dolomite cement.

Neomorphism of micrite to microsparite downgraded the microporosity but still some microporosity may exist within the micritised grains.

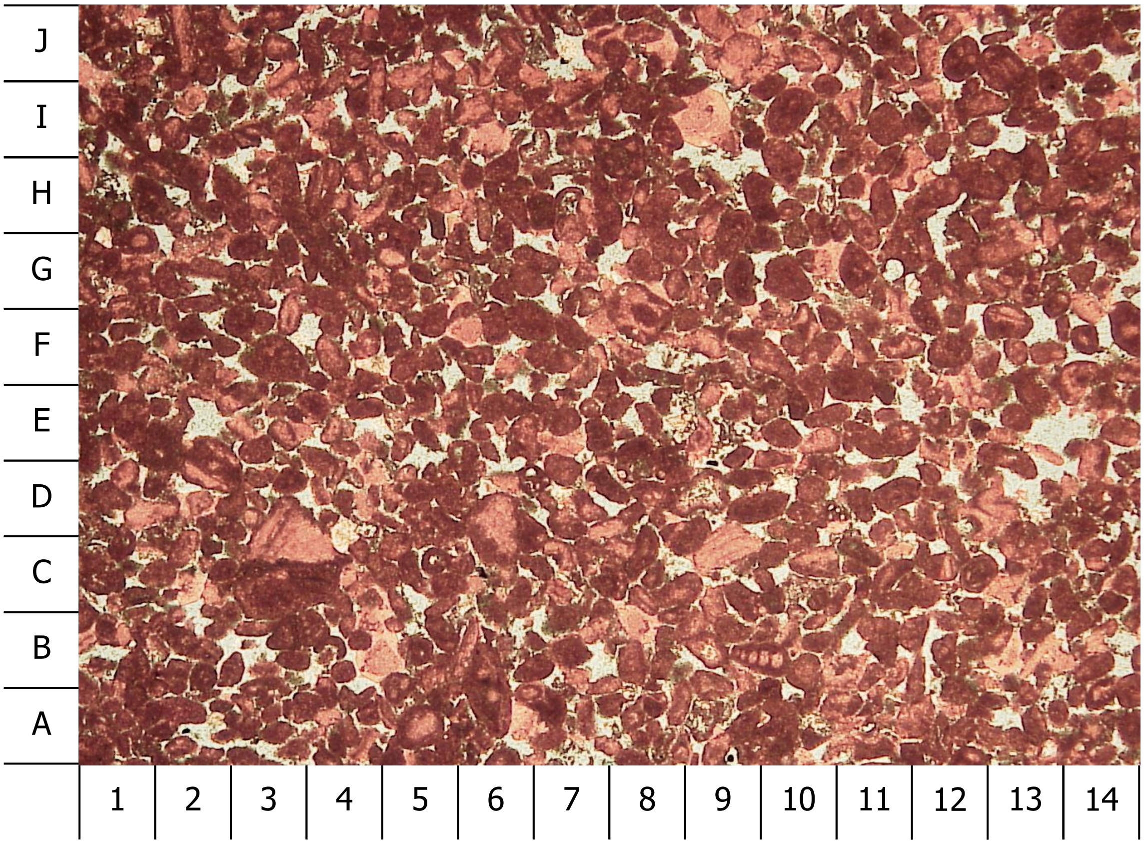

Figure A-1: Thin section photomicrograph – Plane polarized light (Magnification x 2 (plate 15a))

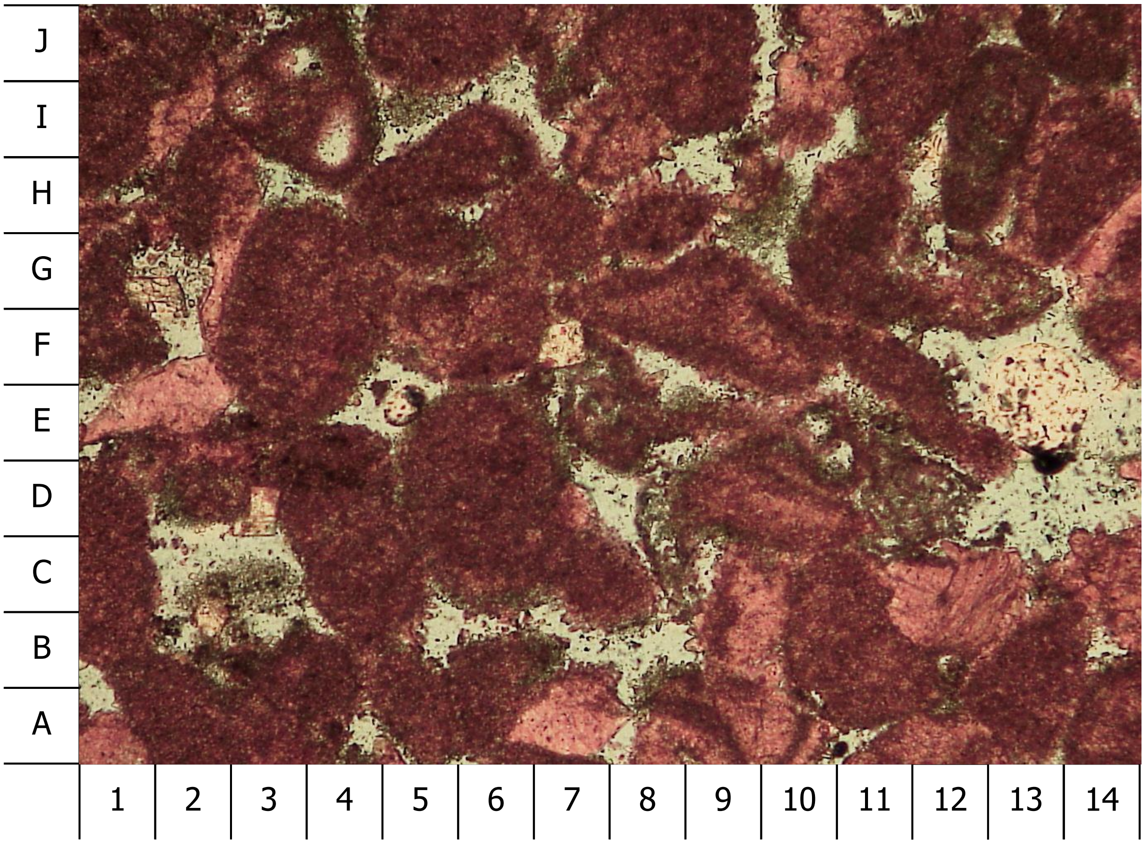

Figure A-2: Thin section photomicrograph – plane polarized light (magnification x 10 (Plate 15b))

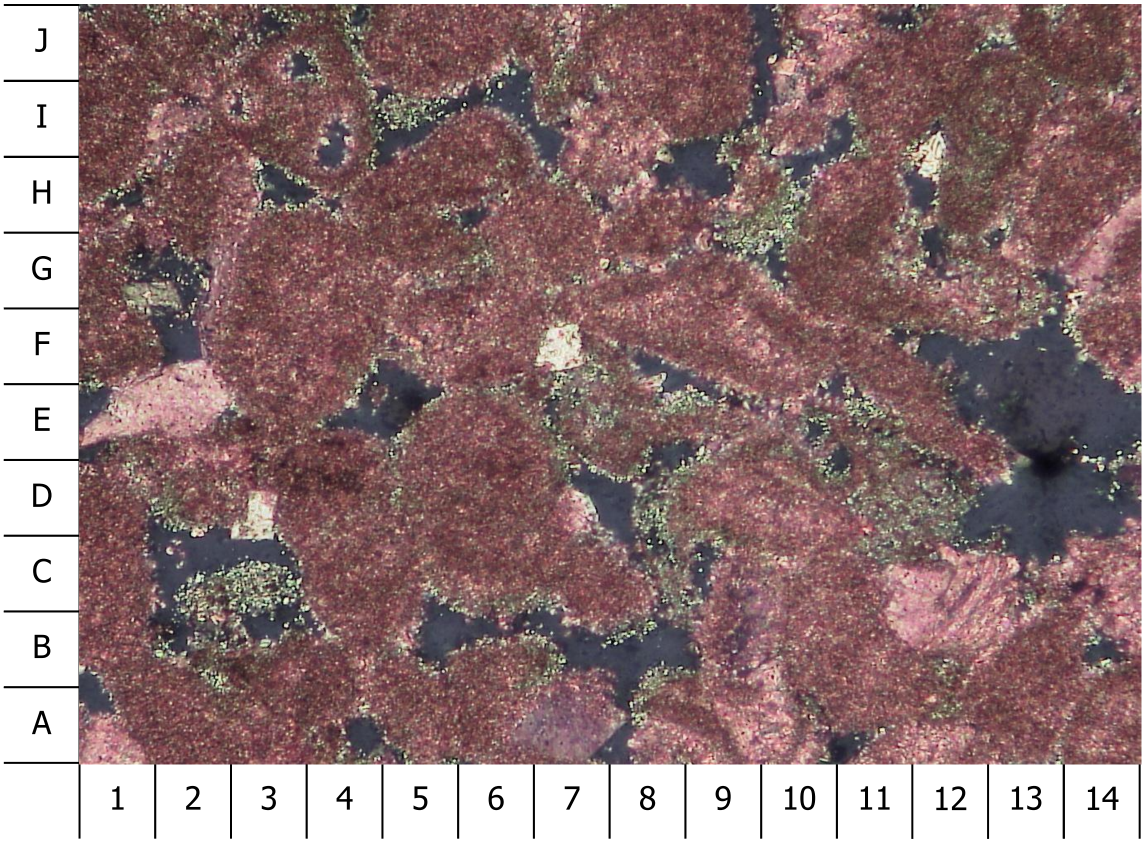

Figure A-3: Thin section photomicrograph – cross polarised light (magnification x 10 (plate 15c))

Scanning Electron Microscope Description

Textural Characteristics

Carbonate grains are partially to completely micritised; their primary structures are largely obliterated. Dissolution of bioclasts and replacement by calcite and dolomite are common. Calcite and very few dolomite are noted as pore-filling cements. Macro- (Plate 16a) and microporosity (Plate 16a, G9) is visible.

Components

The major and very dominant component observed in the sample is **calcite** (99.8% according to XRD data). Only trace amounts of **dolomite** are reported from the XRD-data. Plate 16a suggests that the amount of dolomite crystals is by far higher, but only some crystals are identified as dolomite. Main components are calcite grains and/or blocky, sparry calcite cement.

Peloids (Plate 16a, I6 and Plate 16b, G7/8) and skeletal fragments are largely to completely micritised and sometimes recrystallised to microsparite (Plate 16b, F9; F13/14). Microporous micrite consists of 1-8 micron, well-sorted, subhedral calcite crystals (Plate 16b, F6) randomly packed to yield a continuous network of micropores.

Cementation/Replacement

Pore-filling **calcite cement** is observed mainly as large sparry calcite cement (Plate 16a, E11 and Plate 16b, I/J9) and/or as large, subhedral single grains.

Small euhedral calcite crystals (Plate 16b, D6) generally are noticed to infill voids and/or pore space.

Dolomite cement is noted as euhedral, rhombic crystals of varying, but mainly large grains (Plate 16c, E7). EDAX graph 16.2 shows a good trace displaying the appropriate Ca and Mg peaks.

Dolomite may occur as well in a more blocky character (Plate 16b, G4). As well EDAX graph 16.1 shows a good trace for dolomite displaying again the Ca and Mg peaks.

Neomorphism of micrite to microsparite is observed (Plate 16b, F9, F13/14).

Pore System

The effective pore system in this sample has been downgraded by pore-filling calcite and dolomite cements (Plate 16a). Interparticle (Plate 16b, B/C14; D/E8), dissolution and moldic pores are present and constitute the macroporosity observed. Although largely cemented, the more blocky character of both calcite as well as dolomite leads to remaining open pore space.

Pore interconnectivity however is slightly downgraded by the presence of pore and pore throat restricting cements and thus seems to be high.

Microporosity associated with subhedral crystals (micrite) is commonly observed (Plate 16b and16c), but at least in parts downgraded by neomorphism of micrite to microsparite. However, some microporosity is obviously present which means a certain amount to the total pore volume occurs as microporosity.

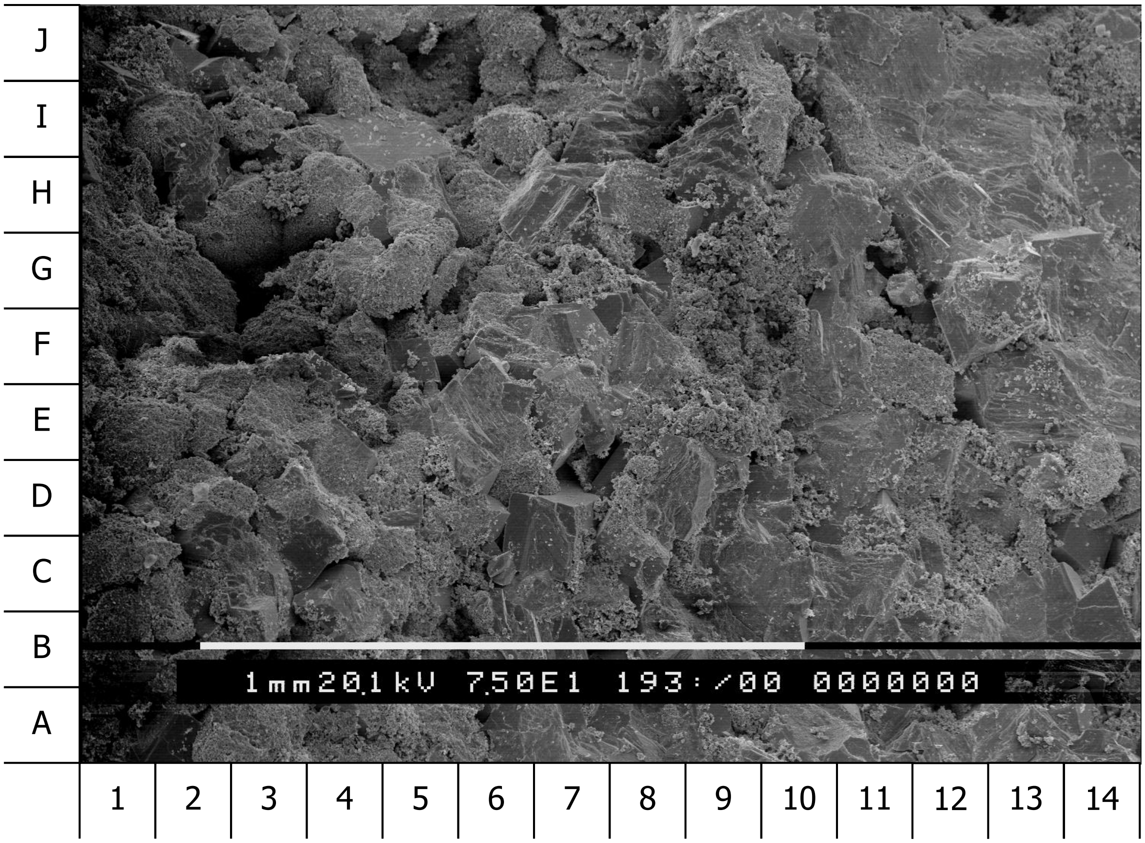

Figure A-4: SEM photomicrograph (plate 16a)

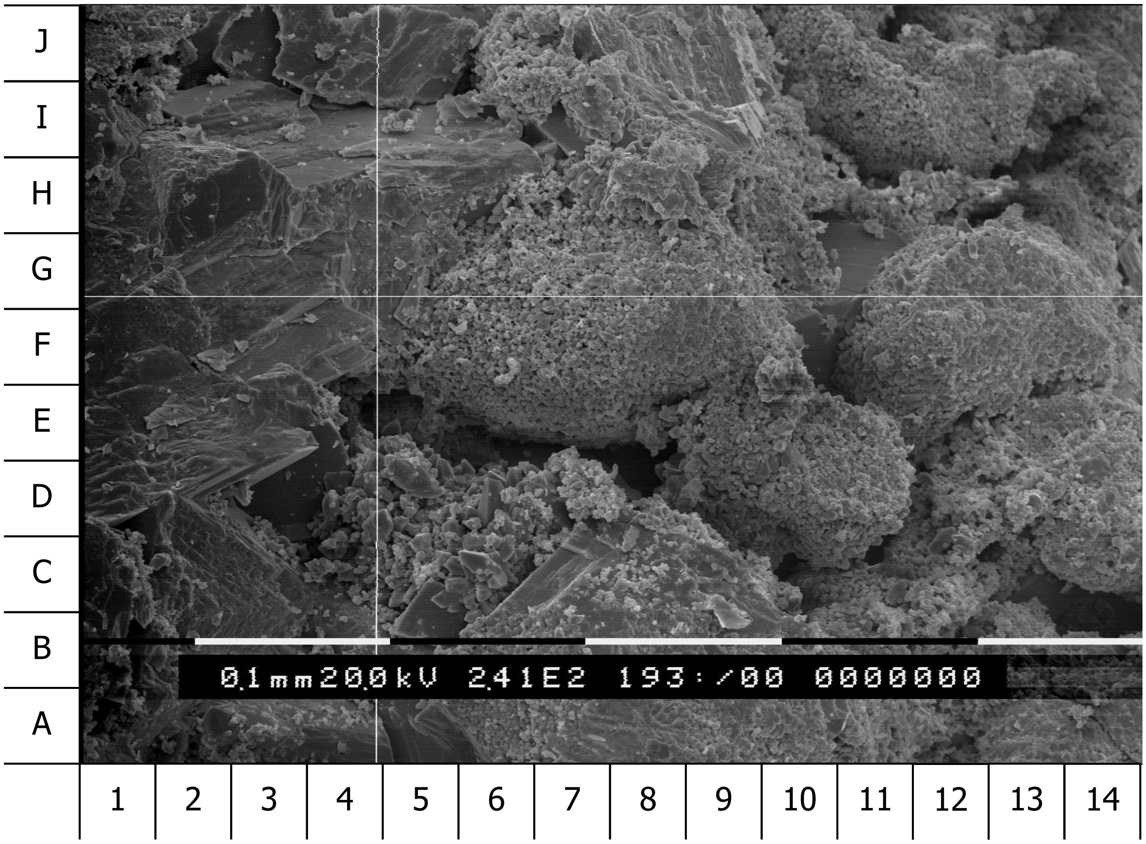

Figure A-5: SEM photomicrograph – EDX 16.1 (plate 16b)

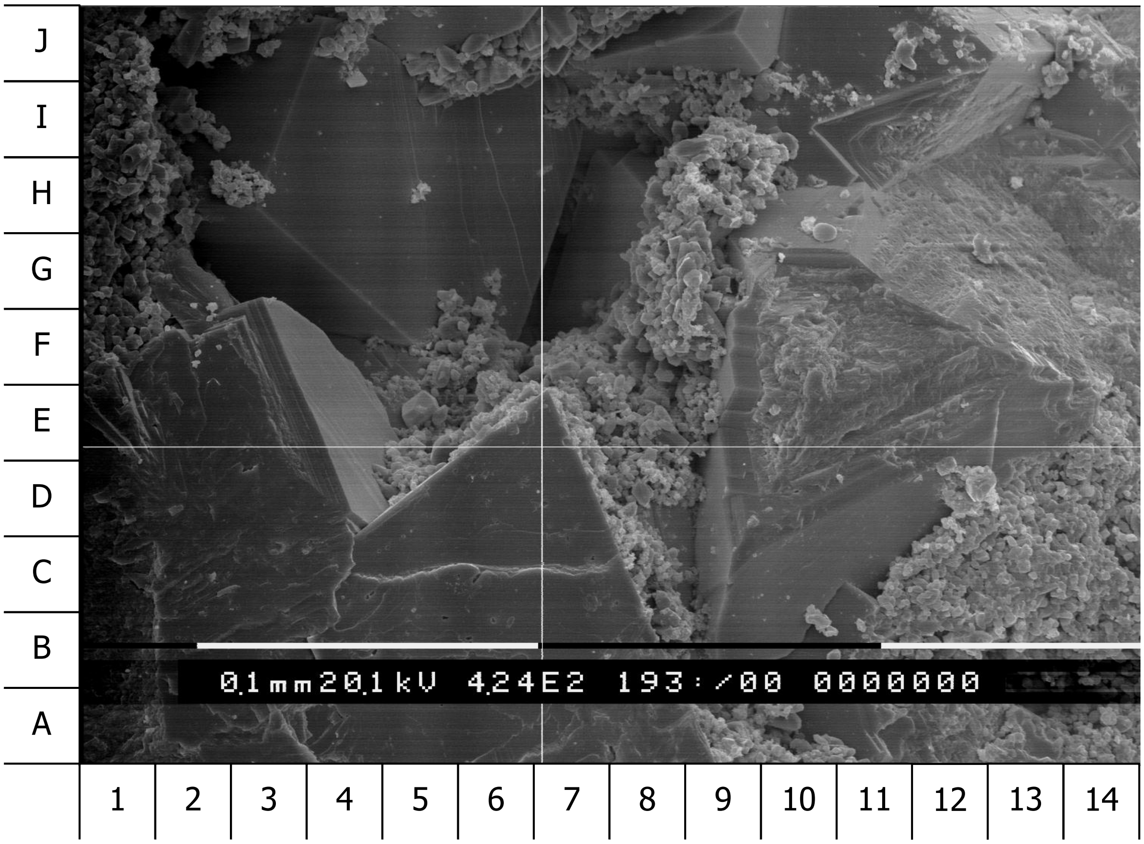

Figure A-6: SEM photomicrograph – EDX 16.2 (plate 16c)

Hydraulic unit 2 Geological descriptions

The thin section photomicrograph (TS) and scanning electron micrograph of a representative sample in hydraulic unit 2 is described in details in Appendix-A as the following:

Thin section description

This representative sample (1029) is classified as Dolomitic Bioclastic Peloidal Grainstone. This sample has gas permeability of 6.1 mD, 14.49% porosity and grain density of 2.73 g/cc. (From core LAB measurements)

Textural Characteristics

The analysed sample contains carbonate grains which are partially to completely micritised. Primary structures of carbonate grains mainly are obliterated by micritisation and recrystallisation of micrite to microsparite, due to neomorphism most of bioclasts cannot be accurately identified. Carbonate grains show variable amounts of dissolution and replacement by calcite and dolomite.

Carbonate grains do not show any preferentially orientation and some grains show boring on the surface. The sample had undergone a fair degree of compaction, grain contacts are mainly long contacts with some sutured and concavo-convex contacts.

Carbonate Grains

Common **peloids** (15.3% of the point count; Plate 1b, G8), few **foraminifera** (12.3% of the point count; Plate 1a, A4), very few **echinoderm fragments** (3.7% of the point count; Plate 1b, F14) are recorded in the sample. All bioclasts are partially to completely micritised and re-crystallised to microsparite, some of them cannot be accurately identified; these are counted as **undifferentiated skeletal fragments** (21.7% of the point count; Plate 1b, D4).

Other Components:

Very rare **pyrite** is recorded in the sample (trace amounts of the point count).

Traces of **hydrocarbon** (organic material) are noted in the sample.

Cementation

Frequent dolomite cement is recorded in the sample (32.3% of the point count; Plate 1b, A6-8), euhedral rhombic crystals of dolomite display high amounts of inclusions (calcite and hydrocarbon in case). Dolomite crystals mainly appear as pore filling cement but replace the carbonate grains in further stages.

Calcite cements, equant (Plate 1b, D2-3), syntaxial and rare isopachous rim (Plate 1b, C4) cements are recorded within pore voids (5.0% of the point count).

Replacement and Neomorphism

Micrite is commonly replacing carbonate grains (Plate 1b, E3), primary structures of carbonate grains are obliterated by micritisation; early stage of neomorphic microspar in parts replacing micrite.

Micrite and microsparite are replaced by dolomite crystals, dolomitisation occur in a very selective manner. Individual dolomite crystals replace various micritised grains (HMC) (Plate 1b, C6) but do not replace the adjacent calcite cement or calcitic fossil fragments (LMC) (Plate 1b, G10). Where such dolomitisation is more extensive, primary fabrics can be completely obliterated.

Pore System

The sample shows mainly **primary interparticle porosity** (5.3% of the point count; Plate 1b, D3); **secondary dissolution porosity** is recorded in the sample (2.3% of the point count; Plate 1b, E6). Dissolution porosity makes intraparticle porosity (Plate 1b, B4) as well as moldic porosity (in case) which normally count as non-effective porosity, where such dissolution is more extensive these porosities are connected to the effective pore system.

The effective pore system in this sample has been significantly downgraded by pore filling dolomite and calcite cements.

Neomorphism of micrite to microsparite downgraded the microporosity but still some significant microporosity may exist within the micritised grains.

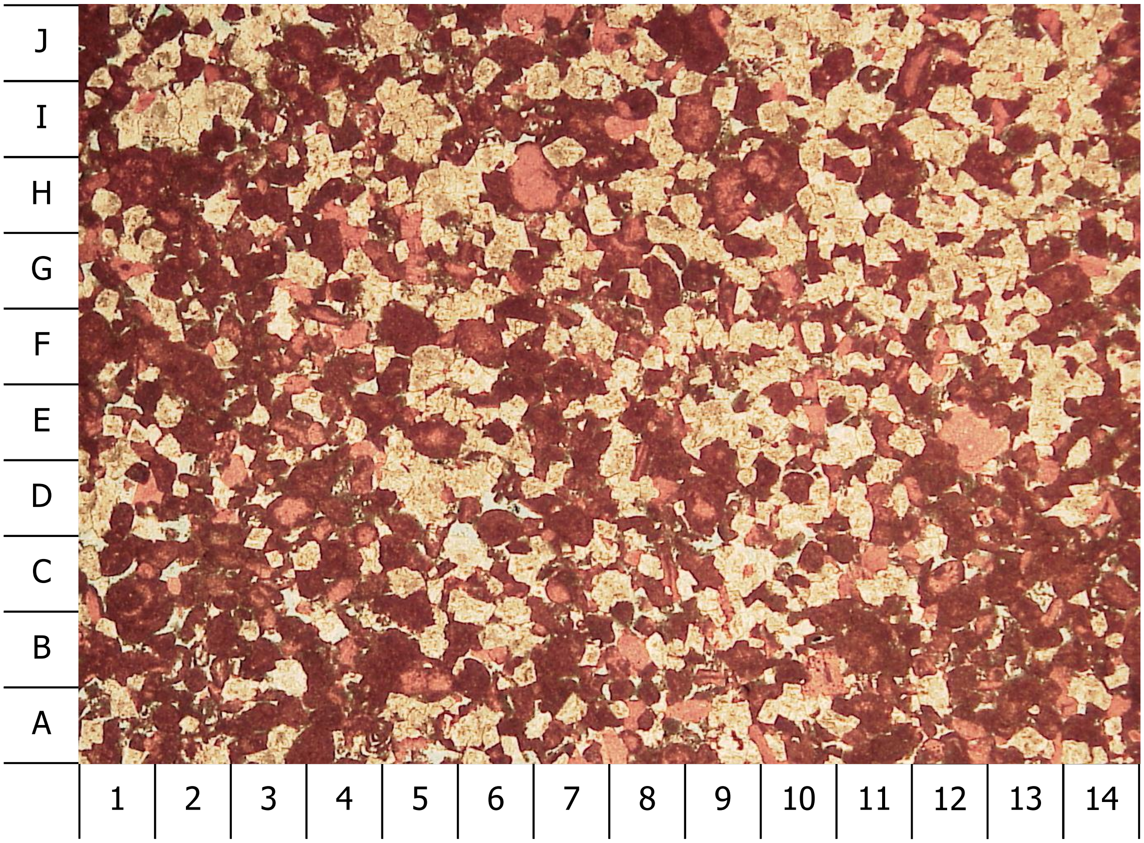

Figure A-7: Thin section photomicrograph – plane polarized light (magnification x2 (plate 1a))

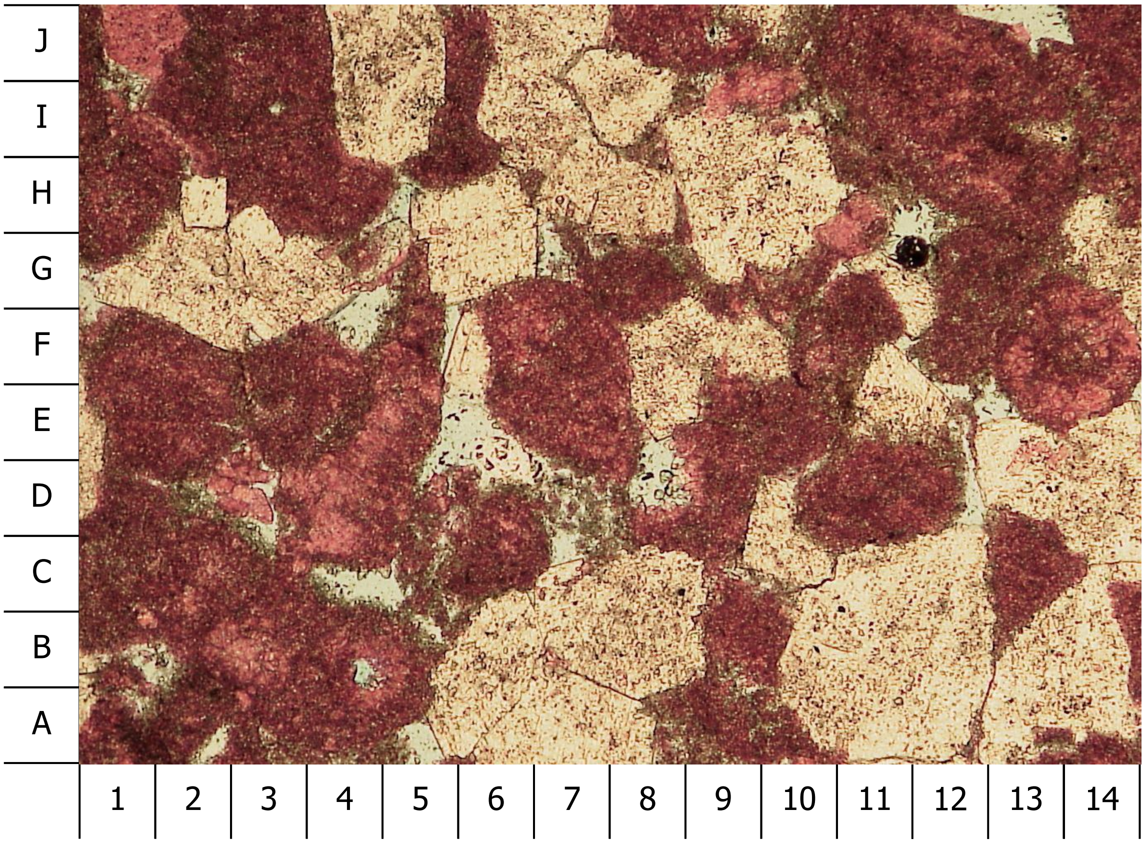

Figure A-8: Thin section photomicrograph – plane polarized light (magnification x 10 (plate 1b))

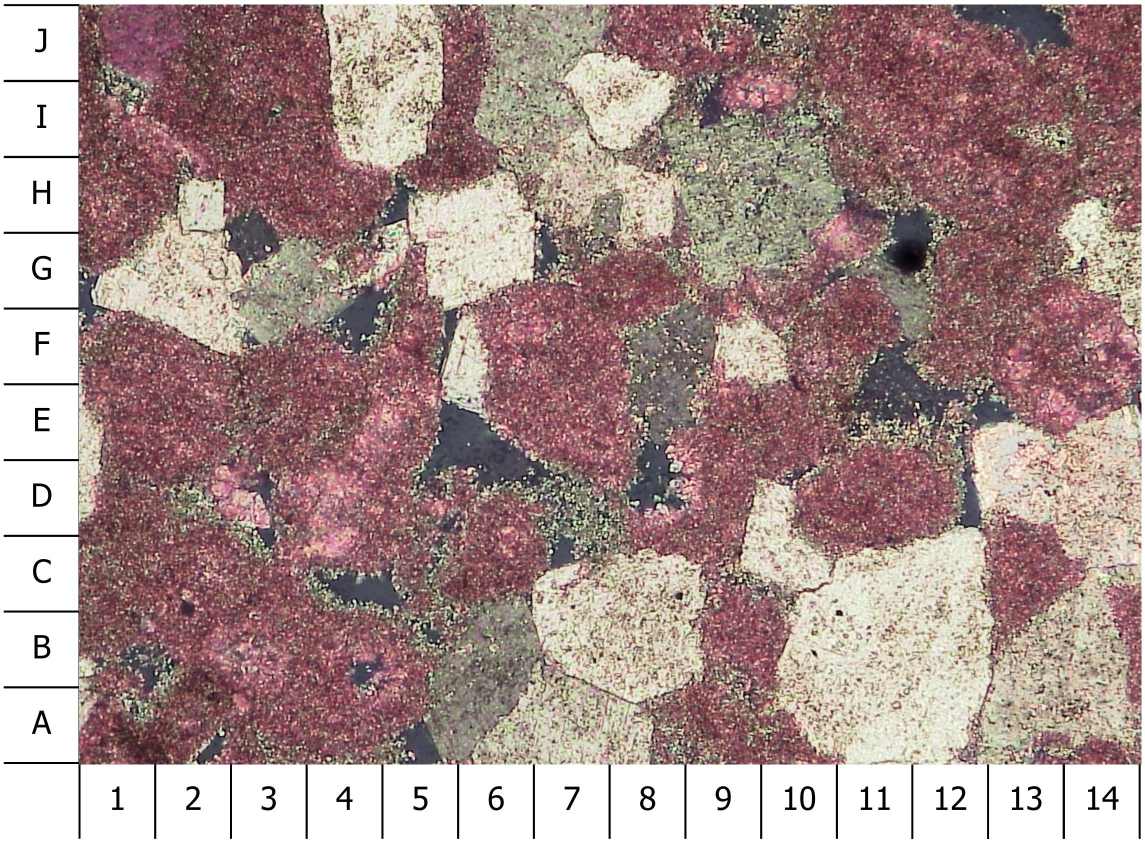

Figure A-9: Thin section photograph – cross polarized light (magnification x 10 (plate 1c))

Scanning Electron Microscope Description

Textural Characteristics

Carbonate grains are partially to completely micritised; their primary structures are largely obliterated. Dissolution of bioclasts and replacement by calcite and dolomite are common. Dolomite and calcite are noted as pore-filling cements. Macro- (Plate 2a) and microporosity (Plate 2c, F8) is visible.

Components

Major components observed in the sample are **calcite** (67.5% according to XRD data) and **dolomite** (32.1% according to XRD data).

Peloids (Plate 2a, H7; H9) and skeletal fragments are largely to completely micritised and sometimes recrystallised to microsparite. Microporous micrite consists of 1-8 micron, well-sorted, subhedral calcite crystals (Plate 2c, F8) that are randomly packed to yield a continuous network of micropores.

Cementation/Replacement

Dolomite cement is noted as euhedral crystals of varying sizes, but mainly large grains (Plate 2a, E7/8; H11 and Plate 2c, D9). EDAX graph 2.1 shows a good trace for dolomite (Plate 2b, G7) displaying Ca and Mg peaks.

Pore-filling **calcite cement** is observed as large sparry calcite cement (Plate 2b, A-D3) and/or as large, subhedral single grains (Plate 2b, E12 and Plate 2c, D3).

Equant, syntaxial calcite grains as well as euhedral to subhedral bladed calcite crystals (Plate 2c, G5) mainly are noticed to infill voids and/or pore space.

EDAX graph 2.2 shows a good trace for calcite (Plate 2c, G5) displaying the Ca peak alone. Calcite and dolomite as single large crystals occluding pore space are easily identified using the EDS.

Neomorphism of micrite to microsparite is frequently observed (Plate 2b, J12/13 and Plate 2c, D13).

Pore System

The effective pore system in this sample has been significantly downgraded by pore-filling calcite and dolomite cements (Plate 2b). Interparticle (Plate 2a, D11; H7), dissolution (Plate 2a, E6/7 and Plate 2b, D6) and moldic (Plate 2b, F2/3) pores are present and constitute the macroporosity found.

Pore interconnectivity however is downgraded by the presence of pore and pore throat restricting cements.

Microporosity associated with subhedral crystals (micrite) is commonly observed (Plate 2c, F8), but at least in parts downgraded by neomorphism of micrite to microsparite (Plate 2b, J12/13). However, some microporosity is obviously present which means a certain amount to the total pore volume occurs as microporosity.

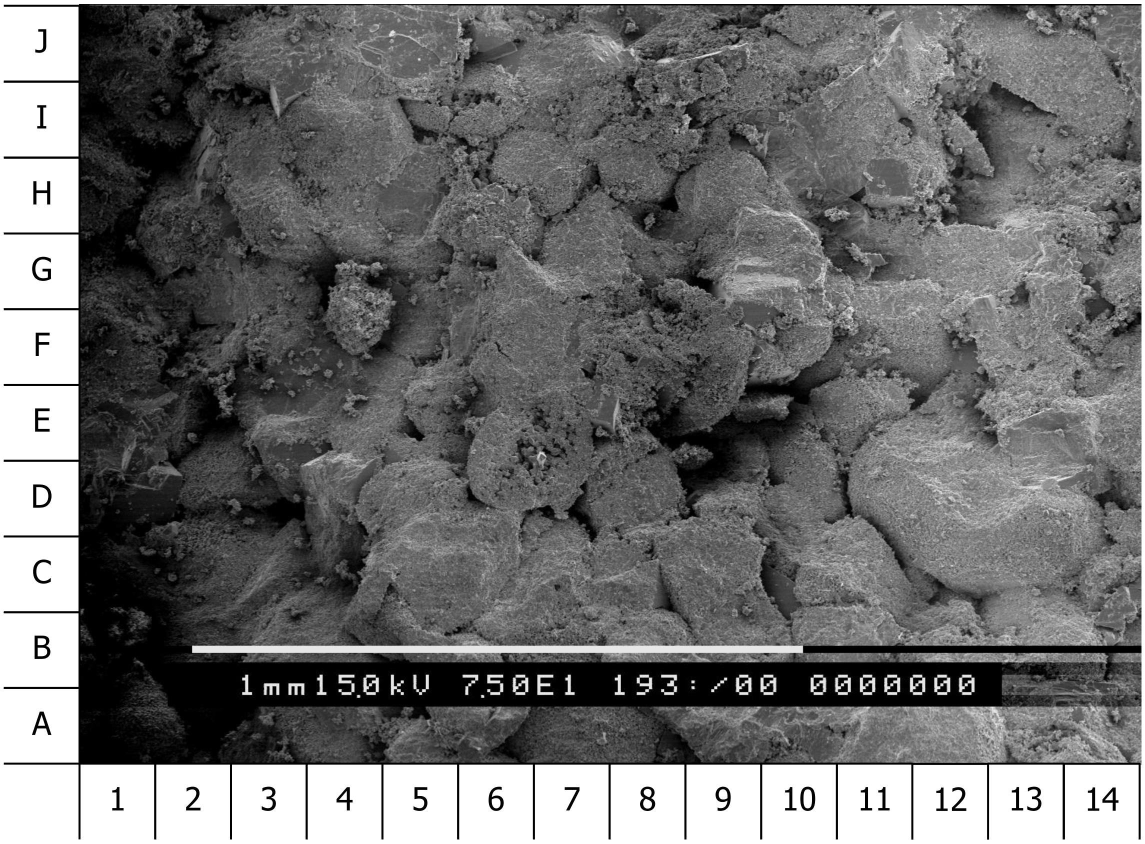

Figure A-10: SEM photomicrograph (plate 2a)

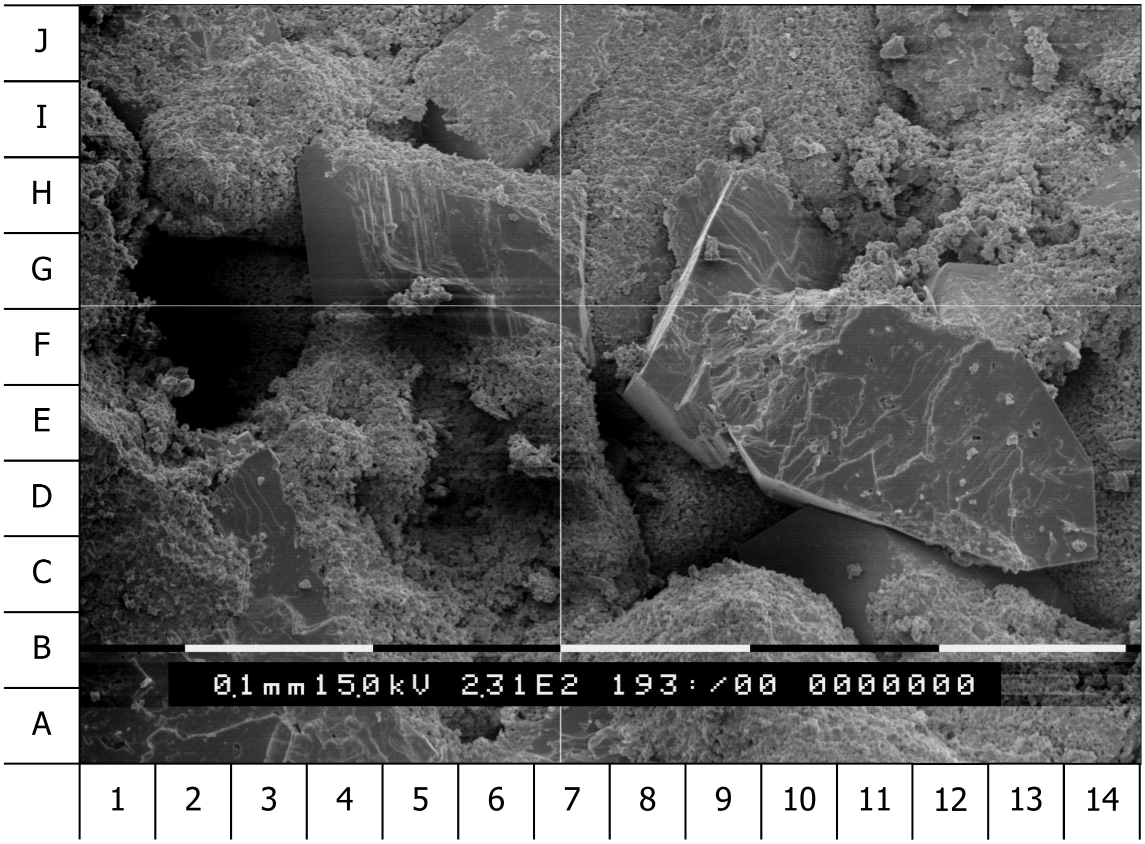

Figure A-11: SEM photomicrograph – EDX 2.1 (plate 2b)

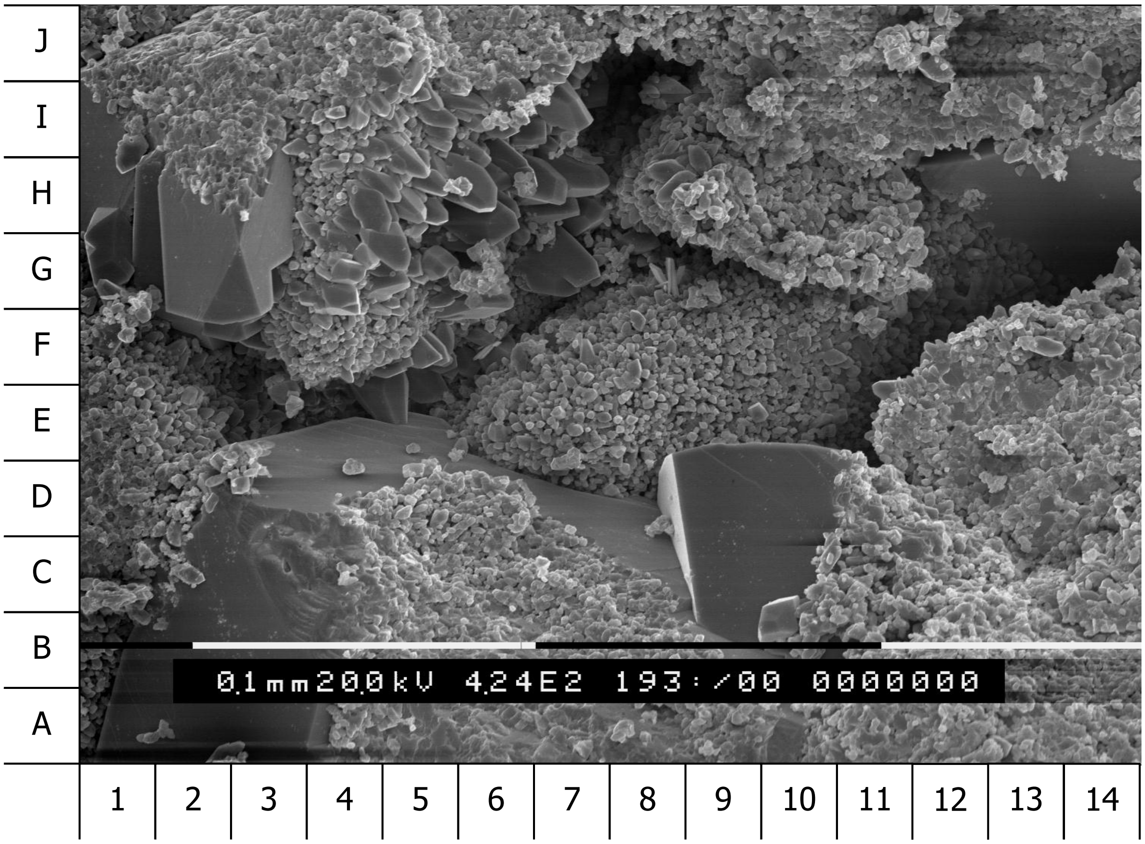

Figure A-12: SEM photograph – EDX 2.2 (plate 2c)

Hydraulic unit 3 Geological descriptions

The thin section photomicrograph (TS) and scanning electron micrograph of a representative sample in hydraulic unit 3 is described in details as the following:

Thin section description

This representative sample (1077) is classified as Bioclastic wackestone. This sample has gas permeability of 1.5 mD, 17.54% porosity and grain density of 2.70 g/cc. (From core LAB measurements)

Textural Characteristics

The analysed sample is matrix supported and contains micritic matrix and bioclasts which are partially to completely micritised, primary structures of bioclasts mainly are obliterated by micritisation; due to neomorphism bioclasts can not be accurately identified. Carbonate grains do not show any preferentially orientation and some fragments show boring on the surface. The sample had undergone a fair degree of compaction, some micro-stylolites (dissolution seams) are noted in the sample, grain contacts are mainly floating with rare point to point contacts. Some open micro-fractures are recorded in the sample; the fractures most likely are artificial and created during thin section preparation.

Matrix

Very dominant micritic matrix is noted in the sample (88.7 % of the point count; Plate 37a, A9); parts of the point counted micritic matrix are micritised bioclasts, the ghost of the micritised bioclasts in some cases are recognisable.

Some dissolution seams (micro-stylolites) are observed within the matrix (Plate 37b and c).

Carbonate Grains

All bioclasts are partially to completely micritised, most of them cannot be accurately identified; these are counted as **undifferentiated skeletal fragments** (4.0% of the point count; Plate 37a, D8).

Residual **organic materials (bitumen?)** have been noted within the sample (trace amounts of the point count).

Cementation

Very few equant calcite cement is recorded in the sample (3.0% of the point count), calcite cement mainly replace the bioclasts or fill the pore spaces.

Very rare dolomite cement is noted in the sample (trace amounts of the point count); dolomite crystals appear as pore filling cement.

Very rare quartz crystals are noted in the sample (trace amounts of the point count); euhedral quartz crystals are recorded within the micritic matrix.

Very rare pyrite is recorded in the sample (trace amounts of the point count).

Replacement and Neomorphism

Micrite is commonly replacing bioclasts, primary structures of bioclasts are partially to completely obliterated by micritisation; early stage of neomorphic microspar in parts replacing micrite. Equant calcite cement in parts replaces bioclasts (Plate 37b, B14).

Pore System

The sample shows mainly **secondary dissolution porosity** (3.0% of the point count; Plate 37a, E4), secondary porosity may result from partly to complete dissolution of bioclasts; rare **secondary interparticle (skeletal) porosity** (1.3% of the point count; Plate 37b, D8) is recorded in the sample.

The total point counted porosity is 4.3%; the pore interconnectivity seems to be poor.

The effective pore system in this sample has been slightly downgraded by pore filling calcite cement.

Some significant microporosity may exist within the micritic matrix.

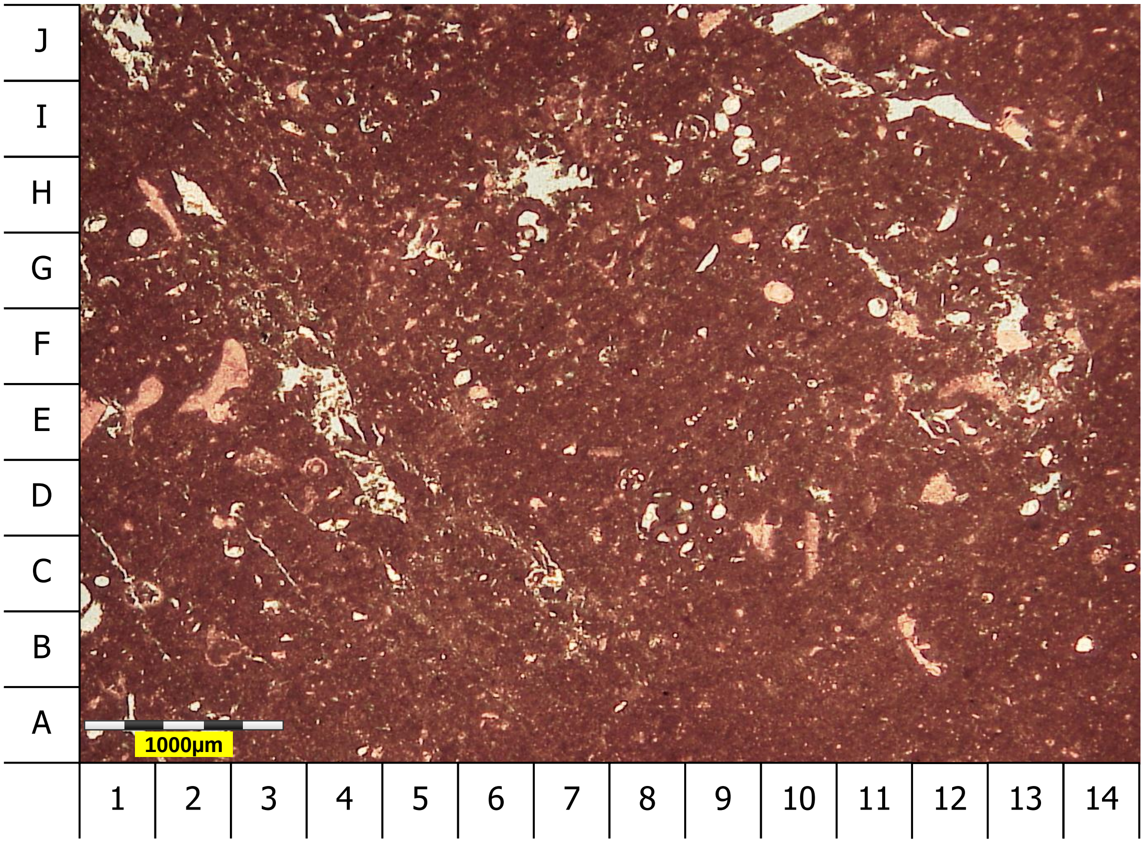

Figure A-13: Thin section photograph – plane polarized light (magnification x 2 (plate 37a))

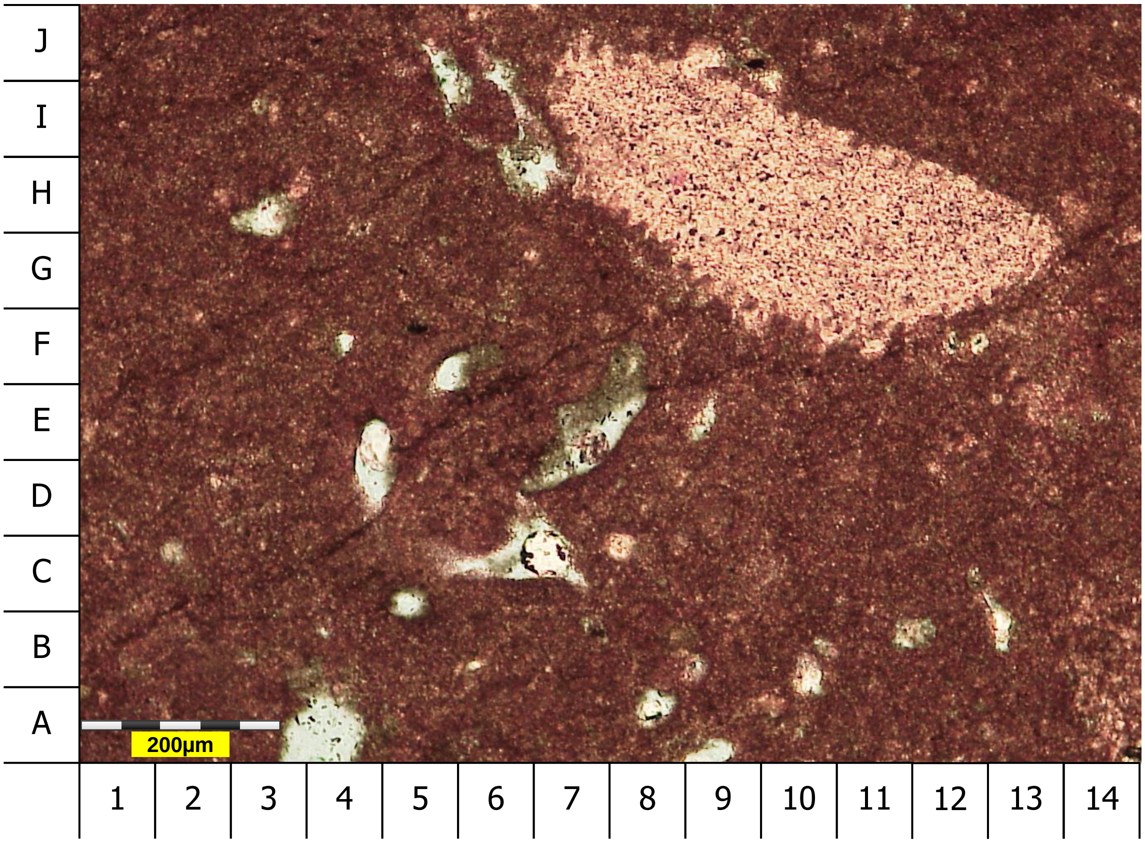

Figure A-14: Thin section photograph – plane polarized light (magnification x 10 (plate 37b))

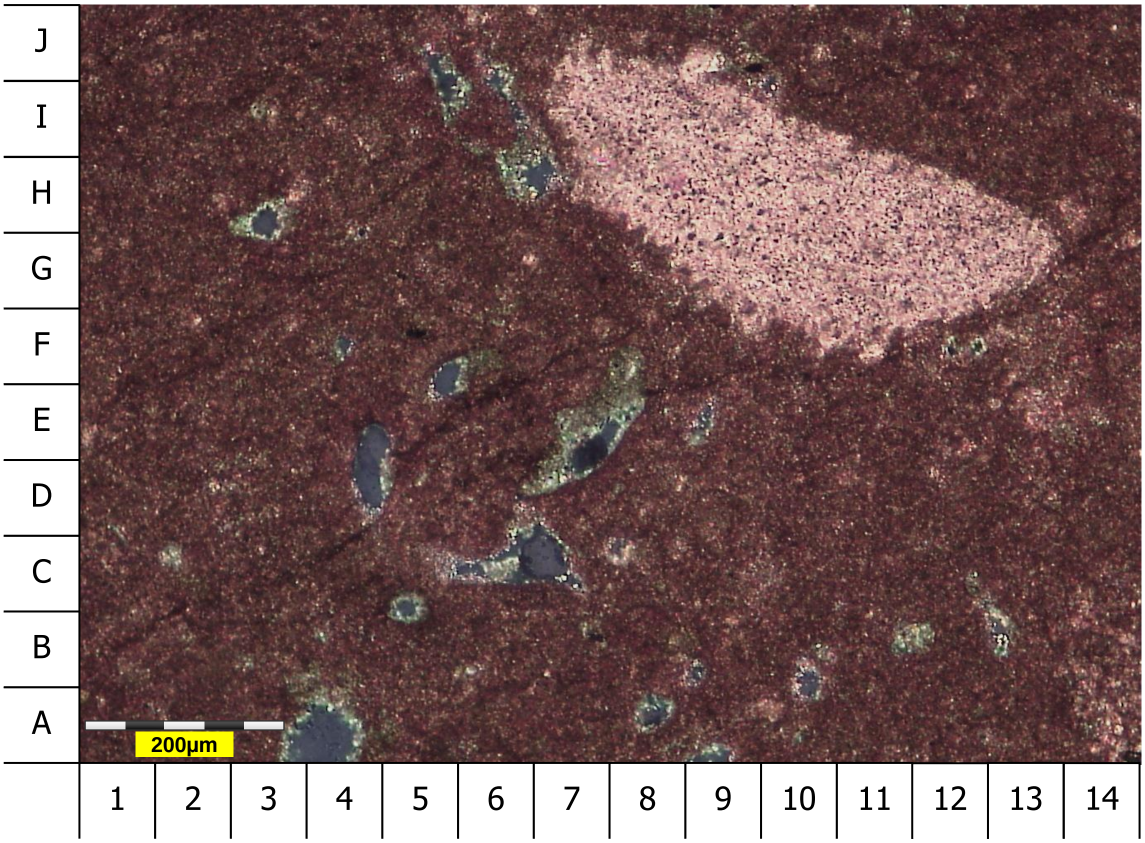

Figure A-15: Thin section photomicrograph – cross polarized light (magnification x 10 (plate 37c))

Scanning Electron Microscope Description

Textural Characteristics

The sample is a matrix supported wackestone. Micritic matrix and micritised bioclasts are the main components. Only minor amounts of pore-filling calcite have been noted.

Macroporosity (mainly dissolution) (Plate 38a, G9) as well as microporosity between the matrix grains (Plate 38c, H3) are visible throughout.

Components

The very dominant component is **calcite** (99.6% according to XRD data).

Bioclasts are largely to completely micritised and thus any primary structures are obliterated. Microporous micrite consists of 1-8 micron, well-sorted, subhedral calcite crystals (Plate 38b and Plate 38c, D6), randomly packed to yield a continuous network of micropores.

Cementation/Replacement

Some **calcite cement** is observed to occur as sparry calcite cement (Plate 38a, B/C1/2; C/D6) occluding pores and pore space. Subhedral single calcite crystals, varying in grain sizes, are noted (Plate 38b, C9; D6; I14). EDAX graphs 38.1 (Plate 38b, C6) and 38.2 (Plate 38c, G10) show good traces for calcite displaying the Ca peak alone.

Some equant calcite grains (Plate 38b, D11/12) are observed mainly situated at the rim of dissolution pores.

Neomorphism of micrite to microsparite is sometimes observed (Plate 38c, D/E12; J9).

Pore System

The effective pore system in this sample has been slightly downgraded by some pore-filling calcite cements. Dissolution porosity (Plate 38a, C8; G/H5) and in cases interparticle porosity (Plate 38a, G9) are present and constitute the observed macroporosity.

Pore interconnectivity may be slightly downgraded by the presence of pore and pore throat restricting cements, but generally seems to be tied up with microporosity and therefore seems to be low.

Microporosity associated with subhedral crystals (micrite) is commonly observed (Plate 38c, H3). Some smaller parts are downgraded by neomorphism of micrite to microsparite (Plate 38c, D/E12). However, this microporosity contributes to a certain and severe amount to the total measured porosity (He-porosity).

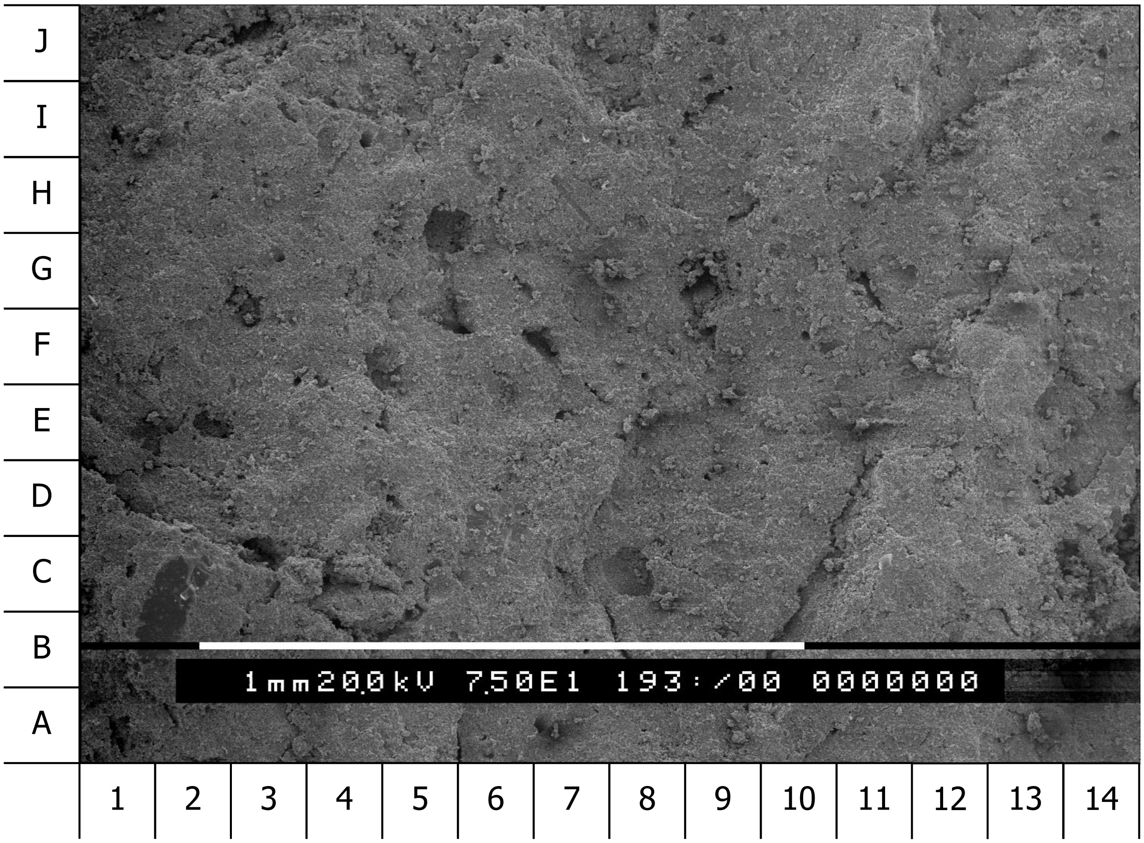

Figure A-16: SEM photomicrograph (plate 38a)

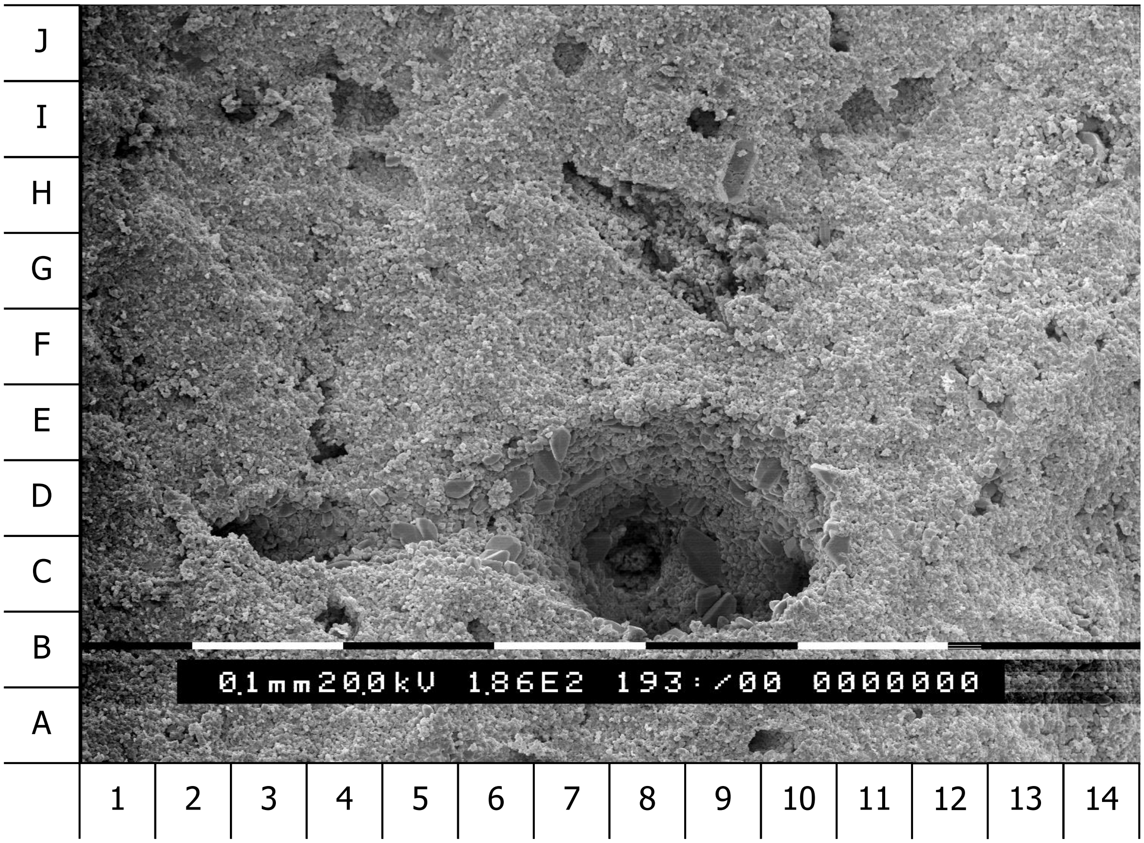

Figure A-17: SEM photomicrograph – EDX 38.1 (plate 38b)

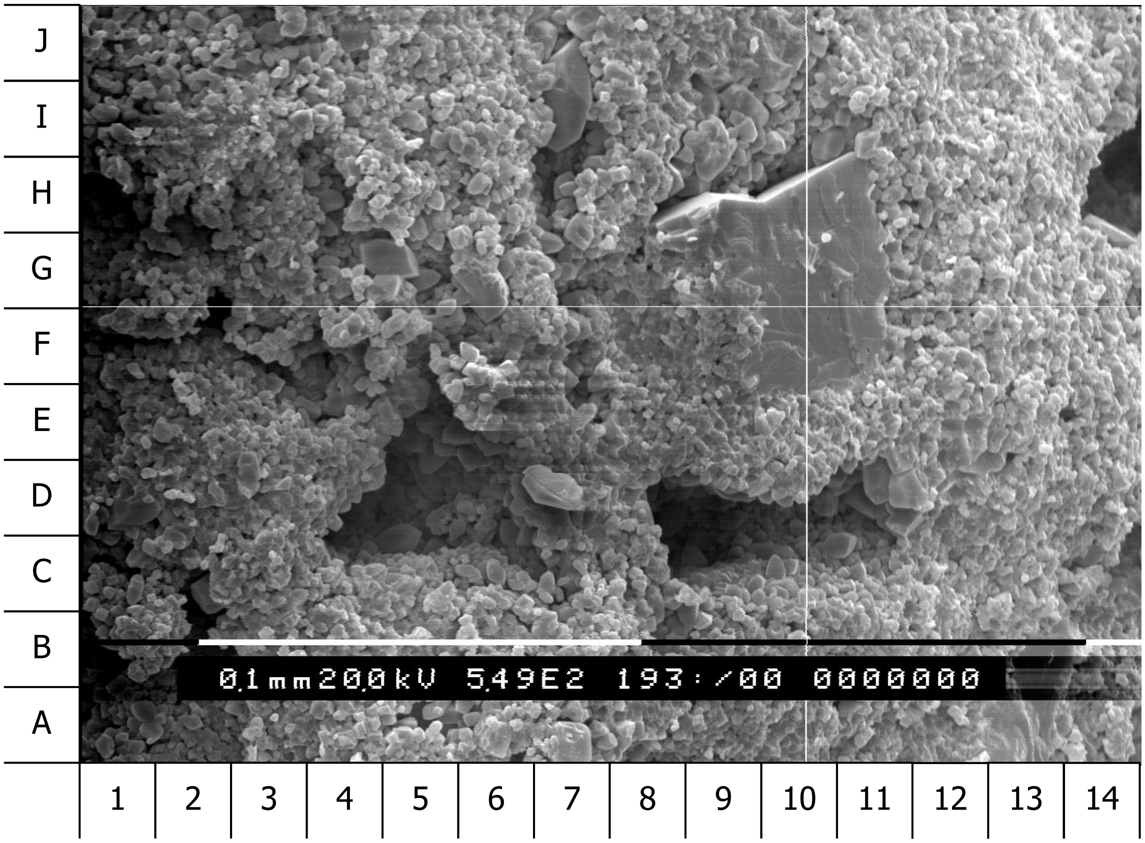

Figure A-18: SEM photomicrograph – EDX 38.2 (plate 38c)

CURRICULUM VITAE

Name:	Mamdouh Nasser Al-Nasser
Nationality:	Saudi
E-mail:	MAMDOUH.NASSER@ARAMCO.COM
Address:	Post Office Box # 9742 Dhahran 31311 Eastern Province, Saudi Arabia
Education:	Bachelor of Science in Applied Chemical Engineering, 2002 King Fahd University of Petroleum & Minerals, Dhahran 31261, Saudi Arabia.
	Master of Science in Petroleum Engineering, 2011 King Fahd University of Petroleum & Minerals Dhahran 31261, Saudi Arabia.
Areas of Interest:	Petrophysical Formation Evaluation
Professional Affiliations:	Society of Petroleum Engineers (SPE)
	European Association of Geoscientists & Engineers (EAGE)
Experience:	Joined Saudi Aramco in January 2002 with Production Engineering Department until 2004. During the production engineering assignment, I worked in Offshore and Onshore fields.
	Since 2004, I have been working with Reservoir Description and simulation Department. During the last five years, I have worked in different Petrophysical areas. I worked on open

hole formation evaluation for geostering operation, Cased hole logging, new logging technology and petrophysical special studies.